Chair of Designing Plastics and Composite Materials

Doctoral Thesis

Mechanical Behavior of Hyperelastic Fiber-Reinforced Composites

Mohammad Reza Mansouri

November 2021

MONTANUNIVERSITÄT LEOBEN
www.unileoben.ac.at

AFFIDAVIT

I declare on oath that I wrote this thesis independently, did not use other than the specified sources and aids, and did not otherwise use any unauthorized aids.

I declare that I have read, understood, and complied with the guidelines of the senate of the Montanuniversität Leoben for "Good Scientific Practice".

Furthermore, I declare that the electronic and printed version of the submitted thesis are identical, both, formally and with regard to content.

Date 04.11.2021

Signature Author
Mohammad Reza Mansouri

ACKNOWLEDGMENTS

This work was carried out in the course of my employment at the Polymer Competence Center Leoben (PCCL) GmbH within the framework of the COMET-program of the Federal Ministry of Science, Research and Economy with contributions by Montanuniversitaet Leoben (Chair of Materials Science and Testing of Polymers, Austria). This research was funded by the Federal Ministry for Climate Action, Environment, Energy, Mobility, Innovation, and Technology and the Federal Ministry for Digital and Economic Affairs, grant number 854178.

I want to express my deepest gratitude to my thesis advisor, Prof. Clara Schuecker, for her professional support during my doctoral study and thorough reviewing of my dissertation and the associated papers. To Prof. Heinz Pettermann from the Technical University of Wien, I am especially thankful for acting as my thesis mentor.

I want to thank Dr. Peter Fuchs, our division manager at PCCL, for giving me the opportunity to join the PCCL Simulation and Modelling team. I am indebted to him for his support and encouragement as well as to let me think out of the box that helped me to develop new ideas.

I would like to thank Prof. Mostafa Baghani from the University of Tehran for having kept supporting me during developing computational codes for the finite element analysis. I greatly thank Prof. Gerald Pinter, Dr. Julia Beter, Dr. Bernd Schrittesser, Gerald Meier, and my friend Dr. Thomas Ules for their contributions to the experimental parts of this work.

To Prof. John C. Criscione from Texas A&M University, I am grateful for sharing new ideas for developing constitutive material models.

ABSTRACT

The aim of the present work is to develop modeling strategies by means of advanced constitutive models and computational frameworks for describing the mechanical behavior of hyperelastic fiber-reinforced materials undergoing finite deformations while being proposed for high efficiency and robustness in finite element application. A unified invariant-base model in terms of the general deformation invariants is proposed to account the contributions of the individual constituent materials, i.e. soft matrix and fibers, and particularly their matrix-fiber mechanical interactions. The present study represents an initial attempt to model matrix-fiber interface debonding in the context of pseudo-elasticity and, moreover, to characterize and computationally evaluate it. For this, inelastic phenomena such as discontinuous Mullins-type softening and permanent set as a result of the matrix damage, the fiber rupture, and the matrix-fiber interface debonding are modeled. The proposed elastic and inelastic constitutive models are successfully implemented into a finite element environment through a general user-defined interface to study a range of initial boundary value problems.

Distinct and particular contributions of the matrix, the fibers, and the matrix-fiber mechanical interaction as well as their respective damage counterparts are characterized independently through performing a comprehensive set of cyclic tensile tests. The experimental observations indicate that fiber-reinforced soft composites exhibit rich complexities, such as nonlinearity, anisotropy, Mullins type softening, and permanent deformations. This work bridges the degradation of the mechanical properties to the microscopically visible matrix-fiber interface debonding for composites undergoing cyclic deformations.

The conformability of the invariant-based constitutive model, implemented in the user-defined subroutine, is validated against the experimental data of composites with different material

anisotropy, indicating good qualitative agreements. Moreover, the pseudo-elastic model is verified by comparison to the cyclic tensile tests, showing a reasonable range of agreement. Finally, this study identifies a unique performance benefit in flexible composite laminates through evaluation of the load-coupling potentials once an external stimulus triggers extensional loadings. To this end, the exceptional, tunable flexibilities of the material are exploited to build up composite laminates with different ply thicknesses, stacking directions, constituent materials, and numbers of plies. A design space is then introduced and used to evaluate the capability of laminates for effective load-coupling behaviors.

KURZFASSUNG

Das Ziel der vorliegenden Arbeit ist die Entwicklung von Modellierungsstrategien mittels fortgeschrittener Konstitutivgesetze und rechentechnischen Gerüsten zur Beschreibung des mechanischen Verhaltens von hyperelastischen faserverstärkten Materialien, unter endlicher Verformung, mit hoher Effizienz und Robustheit in der Finite-Elemente-Anwendung. Es wird ein einheitliches invariantenbasiertes Modell in Form von allgemeinen Invarianten der Verformung vorgeschlagen, um die Beiträge der einzelnen vorkommenden Materialien, d.h. weiche Matrix und Fasern, und insbesondere ihre mechanischen Matrix-Faser Wechselwirkungen zu berücksichtigen. Die vorliegende Arbeit stellt einen ersten Versuch dar, das Matrix-Faser-Interface-Debonding, im Kontext der Pseudoelastizität, zu modellieren und darüber hinaus zu charakterisieren und rechnerisch zu bewerten. Dazu werden inelastische Phänomene wie diskontinuierliche Entfestigung nach Mullins und permanente Verfestigung, welche wahrscheinlich als Folge von Matrixschädigung, Faserbruch und der Matrix-Faser-Grenzflächenversagen auftreten, modelliert. Die vorgeschlagenen elastischen und inelastischen konstitutiven Modelle wurden über eine allgemeine benutzerdefinierte Schnittstelle erfolgreich in einer Finite-Elemente-Umgebung implementiert, um eine Reihe von Randwertproblemen zu untersuchen.

Die jeweiligen Beiträge der Matrix, der Fasern und der mechanischen Wechselwirkung zwischen Matrix und Fasern sowie die jeweiligen Schädigungen werden unabhängig voneinander durch eine umfassende Anzahl an zyklischen Zugversuchen charakterisiert. Die experimentellen Beobachtungen zeigen, dass faserverstärkte weiche Verbundwerkstoffe eine große Komplexität aufweisen, wie z.B. Nichtlinearität, Anisotropie, Entfestigung nach Mullins und permanente Verformungen. Diese Arbeit stellt eine Verbindung zwischen der Degradation der mechanischen Eigenschaften und dem mikroskopisch sichtbaren Debonding der Matrix-Faser-Grenzfläche bei Verbundwerkstoffen unter zyklischer Verformung her.

Die Anpassungsfähigkeit des invariantenbasierten Konstitutivgesetzes, welches in der benutzerdefinierten Subroutine implementiert ist, wurde anhand der experimentellen Daten von Verbundwerkstoffen mit unterschiedlicher Materialanisotropie validiert und zeigt gute qualitative Übereinstimmungen. Darüber hinaus wird das pseudoelastische Modell durch den Vergleich mit den zyklischen Zugversuchen verifiziert, was eine akzeptable Bandbreite der Übereinstimmung zeigt. Schließlich identifiziert diese Studie einen besonderen Leistungsvorteil in flexiblen Verbundlaminaten durch die Auswertung der Lastkopplungspotentiale, sobald ein externer Stimulus Dehnungsbelastungen auslöst. Zu diesem Zweck werden die außergewöhnlichen, einstellbaren Steifigkeiten des Materials ausgenutzt, um Verbundlaminate mit unterschiedlichen Lagenstärken, Stapelrichtungen, konstituierenden Materialien und Lagenzahlen aufzubauen. Anschließend wird ein Designraum eingeführt und verwendet, um die Fähigkeit der Laminate für ein effektives Lastkopplungsverhalten zu bewerten.

TABLE OF CONTENT

PART I: OUTLINE AND SUMMARY

1. STATE OF THE ART AND MOTIVATION

Past efforts in the study of classic composites were mostly devoted to harnessing fiber-reinforced composites' extreme properties, such as their high tensile strength and low elongation. As reinforcements, glass, polyester, and carbon fibers have high tensile strength, and, within their operating limits, they show very little deformation. When they are embedded in a soft elastomer, it harnesses their key characteristics in an exceptionally flexible form, enabling the development of fiber-reinforced materials in soft applications. These applications include pressure-controlled robotic actuators [1–4] , soft wearable systems [5,6], morphing aircraft wings [7–10], artificial muscles [5,11,12], elastofluidics [13–15], aerospace applications [16–18], and energy-absorbing composite systems [7,19]. Some of these applications are shown in Fig. 1.

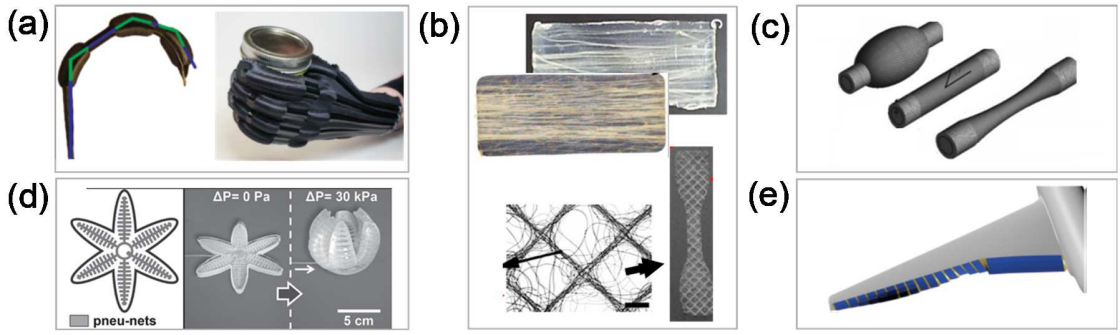

Fig. 1. Some applications of soft reinforced materials: a) wearable robots [5]; b) biocompatible materials [20,21]; c) artificial muscles [22]; d) soft actuators [23]; and e) morphing wings [24].

Versatile material morphology and the resulting unique mechanical properties make soft fiber-reinforced composites an interesting alternative for classical resin-based materials in load coupling applications. To investigate the potential of different material combinations aiming at maximized load coupling effects, several composite laminates considering different load cases and boundary

conditions can be studied using computational tools. However, development of computational tools for such composites is challenging becaues the high stiffness discrepancy between matrix and reinforcement will cause significant flexibility changes in some directions and extreme linear stiffness in others. Moreover, flexible composites are defined as materials consisting of at least two phases such as elastomeric matrix and fibers and a recognizable interphase or an interface with zero thickness. Thus, developing a large-strain anisotropic constitutive model in a commercial FE software considering the contributions of all material constituents and interphase/interface to the deformation is necessary. In this regard, available finite strain anisotropic models in the literature are comprehensively reviewed in the following, emphasizing their ability to account for contributions of all material constituents.

Flexible fiber-reinforced materials, including biological organs and inorganic composites, are considered as hyperelastic continuums in the sense that it is assumed there exists a potential function Ψ which represents the total stored energy of the continuum during the deformation. The majority of the works in the field of flexible fiber-reinforced materials take into account the potentials of the individual constituent materials, i.e. soft matrix and fibers, to model their constitutive behaviors. The papers by, for example [25–32] accounted the contributions of the matrix and fibers as constituent materials for modeling inorganic fiber-reinforced composites. In addition, the works by [33–37] are examples in which the contributions of the constituent materials are only considered for mechanical behavior modeling of soft biological tissues. The work presented by Holzapfel-Gasser-Ogden (HGO) [33] is the most used constitutive model for modeling fiber-reinforced hyperelastic materials. A few works considered the matrix-fiber mechanical interaction potential for constitutive modeling of flexible fiber-reinforced materials. The matrix-fiber interaction potential is introduced by [38] and [39] for modeling the mechanical behavior of human annulus fibrosus. Since then, the interaction potential is taken into account for modeling of the continuous cord-rubber composite [40], biological tissues [41], soft inorganic composites with continuous fibers [42], and dry fabrics [43]. Recently, [44] and [45] considered an interaction potential associated with coupling between dispersed

collagens and cross-links for modeling of soft tissues. In the existing models, a contribution of the stretch in fiber directions to the matrix-fiber interaction potential has been considered. In addition, only a few papers such as [40] and [41] studied the effects of including the matrix-fiber interaction potential in the overall behavior modeling of soft composites, which are limited to the model fitting using symmetric deformations.

In this work, the matrix-fiber interaction mechanism is hypothesized to be a result of the fibers' rotation and not of the fibers' elongation. Accordingly, we aim to propose a model in a constitutive framework on the basis of an angular-base deformation invariant to exclude the contribution of fibers in the matrix-fiber interaction potential. A specific deformation invariant to capturing the effect of the rotation of fibers has not yet been employed for modeling the matrix-fiber interaction potential. In addition, very little is known about the relevance of this potential and the material constituents' potentials in the mechanical behaviors of flexible composites. That is why a quantitative evaluation of the models considering the interaction potential has not yet been carried out and their respective experimental characterization has not been evaluated satisfactorily in the literature.

Flexible composites are defined as materials consisting of at least two phases such as elastomeric matrix and fibers and a recognizable interphase [46,47] or an interface with zero thickness. The matrix-fiber interface/interphase, which is referred to as adhesion bond, guarantees the stress transfer from the soft matrix to stiff fiber and is the key factor of composite performance [46,48]. The chemically formed adhesion bonds influence directly the mechanical interactions between the matrix and the fibers so that weak adhesion bonds result in early matrix-fiber debonding [49] and therefore less contribution of the matrix-fiber mechanical interactions to the composite performance as a whole [50]. There are largely ignored aspects of hyperelastic, fiber-reinforced composites, one of the most important of which is inelastic behavior induced by microscopic damage in the individual material phases of a composite. This phenomenon is referred to in literature as Mullins-type softening and irreversible permanent strain. In fibrous materials, the matrix-fiber debonding is an

additional factor that intensifies inelastic behaviors. However, there is no clear understanding of how much of the damage in fiber-reinforced materials stems individually from the matrix, the fibers, and the matrix-fiber debonding. In addition, distinct contribution of the matrix-fiber debonding to the degradation of the mechanical properties of fiber-reinforced materials has not yet been addressed in the literature. Although the models of hyperelastic fiber-reinforced materials are developed within a decoupled representation assuming separated contributions of their individual constituents, however, determining their actual mechanical contributions is challenging, being reflected in the immense variety of the proposed models which are reviewed in this section. For instance, recently, [51] and [52] selectively removed the ground matrix by chemically treating tissues, tested the remaining noncollagenous matrix material, and found that including the damage for the noncollagenous matrix material in the decoupled-representation-based constitutive modeling—as considered in [53], [54], [55], [56], [57], and [58]— did not change the results comparing to the case when damage is not considered for the noncollagenous matrix.

The damage models developed to account for damage-induced inelastic phenomena can be roughly categorized into two groups: continuum damage mechanics (CDM) and models based on pseudo-elasticity (for an overview of the pseudo-elasticity method, the reader is referred to [59] and [60]). In this section, the works supported these two approaches are comprehensively reviewed with an emphasis on their ability to account for the distinct and particular contributions of the matrix damage, the fiber rupture, and probably the matrix-fiber debonding, reproducing the inelastic behaviors such as Mullins type softening and permanent strain. The models attributed to a complete damage modeling of material failure due to the application of stress or strain exceeding the elastic limit of the material are not discussed here [61–65]. Continuum damage mechanics (CDM) models are on the basis of a hyperelastic strain-energy function wherein the damage is incorporated by a damage function with internal variables to account for the energy dissipated during loading-unloading cycles [66,67]). In the works of [54], [56], [68,69], and [70] models were introduced within the framework of CDM for soft tissues considering separated contributions on Mullins-type softening

damage from matrix and fibers. The works presented in [71], [69], and [72] introduced a model for the description of stress-softening and permanent strain observed in the uniaxial cyclic extension of collagenous soft tissues suggesting that the damage occurs only in fibers. A similar approach is used by [73] and [74] with the difference that in addition to the collagen fibers they considered the damage from the elastin matrix as well. An alternative approach for modeling inelastic damage attributes in fiber-reinforced materials is based on pseudo-elasticity introduced by [75], in which the material is treated as elastic in loading while showing inelastic behavior in unloading. This approach is extended by [60] for modeling Mullins effect in filled rubbers and further developed by [59] for modeling the Mullins effect and permanent strain in particle-reinforced rubbers. The same approach is used in [76] to model the inelastic behavior of the brain as an isotropic material. In Ref. [77] a pseudo-elastic model is presented for soft tissues that incorporates stress softening in both the isotropic matrix and the fibers without considering the permanent strain. The work presented in Ref. [78] proposed a new model to describe Mullins-type softening in aortic layers when loaded beyond the physiological range. However, the permanent strain observed in the experimental results is not accounted therein. The work is extended in [79] accounting for the Mullins softening and the permanent strain in arterial tissues. The damage model assumes that the Mullins softening occurs only in collagen fibers while both matrix and fibers contribute simultaneously to the permanent strain. Recently, [80] studied the Mullins-type softening in short fiber, soft composites in the pseudo-elasticity framework considering damage for both matrix and fibers. However, the permanent strain is not accounted in the modeling, unlike the observations in the experiment. They assumed that the matrix-fiber debonding contributes to the matrix damage term due to void nucleation at the bonding sites and further evaluated their model against the cyclic uniaxial extension of specimens with fibers parallel to the loading direction.

Based on the careful literature survey carried out in this work, the advantages and limitations of both continuum damage mechanics in connection with hyperelasticity and pseudo-elasticity models are listed. Both methods are able to model the separated contributions on damage from the matrix and

fibers, nevertheless, this alone is not enough. In hyperelasticity, a significant advantage of pseudo-elasticity models relative to approaches based on continuum damage mechanics is that the material parameters can be obtained independently of damage parameters [78,81] thereby a change of damage variable does not alter the overall value of the strain energy [82]. A limitation of models developed based on continuum damage mechanics in regard to hyperelasticity, which has not been pointed out in the literature, is that one cannot distinguish the contribution of the stress softening from the permanent strain on damage, in that, both share the same damage parameters, while, pseudo-elastic models can do. Furthermore, the material calibration is found to be more complicated in CDM models than for the pseudo-elastic models [74]. Continuum damage mechanics is not satisfactory for reproducing the Mullins effect for materials showing a high reduction of stiffness due to inelastic dissipation (see, [57], [77,83–85]) a phenomenon that is common in elastomers. The inherent simplicity of the pseudo-elasticity approach makes it specifically suitable for computational implementation and practical applications [67,79]. Based on the literature reviewed, two valuable conclusions are made. (i) To the best of our knowledge, the inelastic damage attributes such as the Mullins-type softening and permanent strain as a result of the matrix-fiber debonding has not yet been modeled. It is reflected in the proposed models wherein the contributions of the matrix and the fibers have been only accounted, while the matrix-fiber debonding would be associated with a third material phase called 'matrix-fiber interface/interphase' neither matrix nor fibers. (ii) Pseudo-elasticity is regarded as a method based on which the material and damage parameters can be obtained independently, nevertheless, employing a relevant constitutive model that enables to account distinct contributions of the material phases of the composite is pivotal with this approach.

2. OBJECTIVES AND METHODS OVERVIEW

Based on the literature reviewed, the hypothesis for this work is that the prediction of the elastic mechanical behaviors can be improved by adding the "matrix-fiber mechanical interaction" term to the constitutive models of hyperelastic fiber-reinforced materials. In addition, it is supposed that this term plays an important role in the damage behavior modeling of soft composites. This work is a first attempt to study these hypotheses and the research objectives to test them are listed as follows.

- Proposing a constitutive framework for modeling hyperelastic materials in terms of not only the matrix and fibers but also the contributions of their interactions, i.e. the matrix-fiber mechanical interactions. The relevance of this term in constitutive modeling of hyperelastic composites is discussed.
- Quantitative evaluating the proposed model via comparisons of the theory with experiments. In addition, the contributions of the material phases and the matrix-fiber mechanical interaction to the deformations are quantified.
- Understanding of what is the underlying mechanism producing damage, i.e. Mullins type softening and permanent deformations, in hyperelastic fiber-reinforced materials through experimental observations. Furthermore, an initial attempt is made to model the matrix-fiber interface debonding in the context of pseudo-elasticity.
- Are flexible composite laminates potential for load coupling applications such as extension-twist coupling.

A brief overview of methods used in this dissertation is given first and then they are described in detail in the following paragraphs. A matrix-fiber-interaction constitutive model is presented and it is further developed to take into account the damage corresponding to the separated contributions of the matrix, fiber, and matrix-fiber interface debonding. Then, the model is implemented in a user-

defined subroutine interface for the finite element applications. To verify the proposed model, it is calibrated against the experimental data. For this, a comprehensive set of experiments is performed on composites with different material anisotropy. Eventually, the potential of the flexible composite laminates for load-coupling applications is discussed using finite element simulations.

In this dissertation, a homogenized anisotropic finite strain material model for fiber-reinforced elastomers with two fiber families is developed within a constitutive framework. The total strain-energy density function is decomposed into three distinct contributions: matrix (Ψ_M), fiber (Ψ_F), and (mechanical) interactions (Ψ_τ) that is named the MFI model, after the first initials of the contributions' names (see **paper 1**). The matrix-fiber interaction mechanism is a result of the fibers' rotation and not of the fibers' elongation. Accordingly, an angular-base deformation invariant, represented by I_8^*, is introduced to be employed by an exponential-polynomial function to form the matrix-fiber interaction potential (see **paper 1**). The proposed model is further developed in the context of pseudo-elasticity to take into account the inelastic phenomena such as discontinuous Mullins-type softening and residual strain due to matrix damage, fiber rupture, and matrix-fiber interface debonding. The pseudo-elastic model is based on hyperelastic strain energy functions with two damage variables for each of the matrix, the fibers, and the matrix-fiber mechanical interactions. The development of the inelastic model is presented in **paper 3**.

The developed model is implemented in the user-defined subroutine UMAT for the purpose of finite element method (FEM) applications. For this, the total Cauchy stress tensor and the Pseudo-elasticity tensors (which are not elastic anymore) are developed and then they are decoupled into volumetric and isochoric parts. The consistent Jacobian matrix, i.e. DDSDDE variable in the UMAT user subroutine, corresponding to the Jaumann rate of the Kirchhoff stress tensor needed for the Abaqus is presented. The algorithmic stress and (pseudo-)elasticity tensors required for the finite element implementation of the pseudo-elastic model are also explained. A uniaxial tension test is carried out on a unit cube composed of one element to illustrate the performance of the model through finite

element implementation. The computational (FEM) and analytical solutions are then compared in order to illustrate the performance of the deveoped code. the FE-implementation of the elastic part of the model is elaborated in **paper 2** while its inelastic part is the focus of **paper 3**.

Comprehensive sets of experiments are carried out on matrix, fiber, and composites with different material anisotropy and aspect ratios. The first measurements include the uniaxial extension of the pure matrix, uniaxial tension of composites with the fiber orientationin [+0/-90] in the fiber direction, stress-stretch responses of composites with the preferred fiber orientations [+45/-45] and [+30/-60] under uniaxial extensions, digital image correlation (DIC) measurements of the strain fields for the composites [+45/-45] and [+30/-60] under tensile tests, the angle between deformed fibers of the composite [+45/-45] recorded via in situ tensile tests, and the wrinkling patterns (out-of-plane deformations) of the uniaxially stretched samples [+45/-45] and [+30/-60] using 3D DIC method. The test methods are described in **paper 2** in greater detail. The second measurements include cyclic tensile tests on pure matrix and the composites [+0/-90] (in fiber direction), [+45/-45], and [+30/-60], the respective strain fields at loadings and unloadings (residual strain) recorded by the DIC method, and in situ tensile tests on composites with the preferred fiber orientation [+45/-45] under microscopy to scan through the whole thickness of the samples enabling a full-field analysis of the matrix-fiber debonding. The second measurements are explained comprehensively in **paper 3**.

Using the first measurements, the (hyper)elastic part of the model is calibrated within the developed constitutive framework as follows. The matrix potential Ψ_M is simply calibrated against the uniaxial extension of the pure matrix. Keeping the material parameters of the matrix, the composites [+0/-90] are subjected to uniaxial tests along the fiber direction to calibrate the material constants of the fibers potential Ψ_F. The material parameters of the interaction potential Ψ_τ are then obtained within the developed constitutive framework via fitting the model into the symmetric uniaxial tensile tests on the samples [+45/-45]. The whole procedure for the calibration of the elastic material model is

presented in **paper 1**. The second measurements are used to obtain the properties of the inelastic model. Before that, the (elastic) potentials of the matrix, the fibers, and the mechanical interaction are calibrated as explained above via the respective cyclic tensile tests but considering only the primary loading path. Keeping now the elastic material parameters, the inelastic model is fitted to the entire loading history for the cyclic loading-reloading stress-stretch responses of the samples [+45/-45]. For this purpose, the damage parameters are calibrated through inverse finite element modeling based on an FEM-model of the test samples using the optimization code LS-OPT employing the least-squares algorithm to minimize the discrepancy between the model results and entered experimental data. The calibration procedure of the inelastic model through the cyclic tentile tests is taken into account in **paper 3**. The elastic part of the model developed within the constitutive framework is now quantitatively evaluated through a comparison of the theory with the first measurements explained above considering the test results of the samples with the fiber orientation [+45/-45]. The comparisons include the stress-stretch responses, strain fields, and rotation of fibers. The conformability of the constitutive equation with experimental results is visualized in the first comparisons. For the strain fields, the principal stretches in loading direction and transverse to the loading are measured and compared to the theory. The rotation of fibers (in other words, the current angle between deformed fibers) is theoretically calculated via the angular-base invariant I_8^* and is compared with the test results. The comparisons are analyzed in detail in **paper 3**. The (elastic) model so calibrated through the first measurements is then verified via the comparison of the finite element simulations with the tensile test results of the composites with the fiber orientation [+30/-60]. The relevance of the matrix-fiber interaction potential in constitutive modeling of hyperelastic composites is illustrated by three representative examples when its effect is neglected (when the interaction potential is neglected the MFI constitutive model is reduced to the Holzapfel-Gasser-Ogden (HGO) model). They include uniaxial extension of single-layer plates with different material anisotropy, inflation-extension of a thin cylindrical tube, and load-coupling behaviors in composite laminates (see **paper 1**). Furthermore, the contributions of the matrix, fibers, and matrix-fiber

mechanical interaction to the total deformations are indicated using a set of finite element simulations on composites with the material anisotropy [+45/-45] and [+30/-60] under uniaxial extensions. It is carried out by showing the spatial distributions and quantitative measurements of the respective potentials. Note, that the material properties obtianed from the first measurements are used for these illustrations. The illustrations can be found in **paper 2**. To validate the predictions of the proposed inelastic damage model, the cyclic stress-stretch experimental responses of non-symmetric deformations on the samples [+30/-60] are compared against the simulation results (FEM). The loading-reloading results are presented. The material parameters obtained from the second measurements are used for these simulations. Moreover, the local stretch maps (the maximum local stretches at loading and permanent stretches after unloading), captured via the DIC method, are compared with the FEM simulation results for the composites with the symmetric deformations (i.e. the samples with the preferred fiber orientation as [+45/-45]) during the cyclic tensile test. The validations of the inelastic model are elaborated in **paper 3**.

Fig. 2 schematically shows the coupling of deformation modes such as end moment (M) and longitudinal (engineering) stress (σ_e) as well as end twist (Ω) in a composite laminate with the off-axis plies subjected to a uniaxial deformation. The values of these parameters, which may be addressed herein as conflicting requirements for designing laminates exhibiting effective extension-twist coupling behaviors, are individually evaluated. Effective load-coupling behaviors necessitate the laminate to possess unique properties, the most important of which are: high output values of the end moment, high end-twist capability, and low longitudinal stress, so as to minimize the actuation force required for stretching the laminates. During the extension-twist coupling behavior, the values of the parameters {M, Ω} are increasing; therefore, based on the definition above, they are not assumed to be conflicting requirements. On the other hand, an effective coupling behavior requires high torsional capability for low longitudinal stresses, which implies that the parameter set {σ_e, Ω} is a conflicting requirement. The set {M, σ_e} is also not suitable for load-coupling applications because the effective load-coupling behavior, as explained above, requires a high-end moment for

low longitudinal stress, while these two parameters are highly coupled to each other. Accordingly, a new term M/σ_e is introduced here, which is called the decoupling ratio (see **paper 4**). The only parameter that remains is the end twist Ω, which is a desirable quantity for load coupling. Consequently, a design space represented by a diagram is considered in which its vertical axis denotes the decoupling ratio M/σ_e, while its horizontal axis shows the degree of torsional flexibility through Ω. To see the introduced design space, the reader is referred to **paper 4**. In this work, effective load-coupling behaviors are studied within this design space.

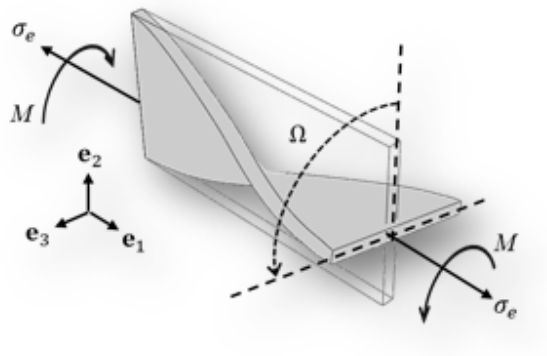

Fig. 2. Extension-twist coupling of a composite laminate.

3. STRUCTURE OF THE THESIS

In this section, the publications during the Ph.D. study are listed and a brief description of them is presented. The contribution of the Ph.D. candidate to the publications is clarified (see Table 3.1) and a description of the works done by each co-author is presented.

Table 3.1. The contributions of the Ph.D. candidate to the publications.

	Paper 1	Paper 2	Paper 3	Paper 4
Conceptualization	100%	100%	100%	80%
Modeling & Simulation	100%	100%	80%	100%
Experimental testing	60%	70%	100%	100%
Data evaluation	100%	100%	100%	100%
Writing - original draft	100%	90%	100%	100%
Writing - review & editing	-	-	-	-

PAPER 1: The contribution of mechanical interactions to the constitutive modeling of fiber-reinforced elastomers

M.R. Mansouri, P.F. Fuchs, J.C. Criscione, B. Schrittesser, J. Beter

European Journal of Mechanics-A/Solids, 85 (2020) 104081 (IF: 4.220)

doi: 10.1016/j.euromechsol.2020.104081.

Description:

In this paper, we developed a Matrix-Fiber-Interaction (MFI) constitutive model and an angular-base deformation invariant is introduced. In addition, the importance of the matrix-fiber mechanical interaction in the constitutive modeling of fiber-reinforced hyperelastic materials is shown.

Authorship contributions:

P.F. Fuchs: Funding acquisition, Supervision, Writing - review & editing. **J.C. Criscione:** Writing-review & editing. **B. Schrittesser:** Supervision, Writing - review & editing. **J. Beter:** Experimental testing.

PAPER 2: Quantifying matrix-fiber mechanical interactions in hyperelastic materials

Mansouri M.R., Beter J., Fuchs P.F., Schrittesser B., Pinter G.

International Journal of Mechanical Sciences, 95 (2021), p. 106268 (IF: 5.329)

doi: 10.1016/j.ijmecsci.2021.106268

Description:

In this work, the MFI model developed within the introduced constitutive framework is quantitatively evaluated through a comparison of the theory with the experimental observations. Furthermore, the contributions of the material phases and matrix-fiber mechanical interaction to the deformations are quantified for composites with different material anisotropy using finite element simulations.

Authorship contributions:

J. Beter: Experimental testing, Writing - original draft. **P.F. Fuchs:** Funding acquisition, Supervision, Writing - review & editing. **B. Schrittesser:** Supervision, Writing - review & editing. **G. Pinter:** Writing - review & editing.

PAPER 3: Matrix-fiber interface debonding in soft composites: Modeling and microstructural evolutions

Mansouri M.R., Fuchs P.F., Baghani M., Schuecker C.

Composites Part B: Engineering (IF: 9.078)

Under review: 19.10.2021

Description:

In this work, the contribution of the matrix-fiber interface debonding to the degradation of the mechanical properties is discussed. Based on the experimental outputs, we present a model covering almost the full phenomenology of hyperelastic fiber-reinforced materials, while being proposed for high efficiency and robustness in finite element application. In this work, the damage mechanisms are modeled in the context of pseudo-elasticity, with a focous on the matrix-fiber interface debonding, and the developed model is compared against cyclic tensie tests. This work indicates that fiber-reinforced soft composites exhibit rich complexities, such as nonlinearity, anisotropy, Mullins type softening, and permanent deformations.

Authorship contributions:

P.F. Fuchs: Funding acquisition, Supervision, Writing - review & editing. **M. Baghani:** Modeling & Simulation, Supervision, Writing - review & editing. **C. Schuecker:** Supervision, Writing - review & editing.

PAPER 4: Elastic load coupling with tailored elastomer composites

Mansouri M.R., Fuchs P.F.

Composites: Part C, 4 (2021), p. 100088.

doi: 10.1016/j.jcomc.2020.100088.

Description:

This work addresses the potential of flexible composites for load-coupling applications such as extension-twist coupling. To this end, the conflicting design requirements such as decoupling ratio between deformation modes, i.e. extension and twist, and torsional flexibility are studied for laminates with different ply thicknesses, stacking directions, constituent materials, and numbers of plies. A design space is then introduced and used to evaluate the capability of laminates for effective load-coupling behaviors.

Authorship contributions:

P.F. Fuchs: Conceptualization, Funding acquisition, Supervision, Writing - review & editing.

4. OVERAL CONCLUSION

By introducing an angular-base deformation invariant, a Matrix-Fiber-Interaction (MFI) model is proposed in a constitutive framework for modeling hyperelastic materials in terms of not only the matrix and fibers but also the contributions of their interactions, i.e. the matrix-fiber mechanical interactions. The proposed model enables us to capture the mechanical behavior of fiber-reinforced elastomers with two fiber families and with different material anisotropy. It is shown by the comparison of experiments with finite element simulations for symmetric and non-symmetric deformation states. In order to show the relevance of the interaction potential in the constitutive modeling of fiber-reinforced elastomers, three representative examples are provided and all are modeled using the MFI and the HGO constitutive models. The results imply that the mechanical interaction potential affects substantially the constitutive behaviors.

The proposed model developed within the constitutive framework is quantitatively evaluated using comparison of the theory with the experimental measurements. The measurements include the stress-stretch responses of composites with different material anisotropy under tensile tests, DIC measurements of strain fields in the loading and transverse to the loading directions, and the angle between deformed fibers (rotation of fibers). The results show good qualitative agreements in all comparisons. In addition, the contributions of the material phases and the matrix-fiber mechanical interaction to the uniaxial extensions of composites with different material anisotropy are quantified using finite element simulations. The spatial distributions and quantitative measurements of the respective potentials signify that the matrix-fiber mechanical interaction is the main mechanism contributing to the mechanical behavior of hyperelastic fiber-reinforced composites.

In this work, the contribution of the microstructural evolution, as a result of the microscopically visible matrix-fiber interface debonding, to the degradation of the mechanical properties is discussed.

The results of the tensile cyclic tests on the pure matrix, fibers, and composites imply that the underlying mechanism producing the Mullins-type softening and permanent deformations can be attributed to the matrix-fiber interface debonding neither matrix nor fibers. It is supported by the matrix-fiber interface debonding observed using the micrographs captured during in situ tensile tests and is reflected in the residual deformations recorded through the stretch maps via digital image correlation after unloading. The information coming from the experiments is used as input parameters for damage modeling. We present a model covering almost the full phenomenology of hyperelastic fiber-reinforced materials, i.e. nonlinearity, anisotropy, Mullins type softening, and permanent deformations while being proposed for high efficiency and robustness in finite element application. The two latter are described by a phenomenological matrix-fiber damage potential, which delivers physically more meaningful behavior in a sense that the degradation of the mechanical properties is reported to be a result of the microscopic matrix-fiber interface debonding. The proposed model distinguishes between the contributions of the composite constituents on the elastic and the inelastic mechanical behaviors by means of applying the three following considerations. (i) Particular elastic and pseudo-elastic energy functions are primarily used enabling to distinguish between the respective contributions of the material constituents. (ii) Adopting pseudo-elasticity as damage framework, say, which allows us to obtain contributions on damage from any of the constituent materials independently of the elastic properties. (iii) The use of separate damage variables to distinguish between the inelastic mechanical behaviors such as the Mullins-type softening and the permanent strain. The model implemented in a user-defined subroutine is capable of reproducing the inelastic behaviors as a result of the matrix-fiber debonding for composites showing significant degradation in their mechanical properties.

In this work, we have identified a unique performance benefit by evaluating the extension-twist coupling potentials in flexible reinforced composites. To exploit the tunable flexibilities of the composites for effective load-coupling behaviors, a set of conflicting requirements are evaluated. As a result, a design space is introduced through which the capability of a laminate can be evaluated for

load-coupling applications. In this space, the load-coupling potential of each laminate can be displayed by only one point on the referred diagram. It shows that, in general, providing a higher degree of decoupling between end moment and longitudinal stress gives rise to a much higher amount of flexibility, which is highly desirable for load-coupling applications. They could be used in products such as morphing systems, which are characterized by conflicting requirements like "exhibit low in-plane stiffness while maintaining large strain capability and exceptional flexibility."

The present study provides the following advancements to hyperelastic material research. It clarifies the role of the "matrix-fiber mechanical interaction" for modeling the elastic and inelastic behaviors of inorganic, flexible fiber-reinforced materials, yet remains to wait for biomaterials, particularly since recently there are many interests in figuring out the effects of coupling between the collagen fibers and extracellular matrix. By performing comprehensive tests combined with finite element simulation studies, guidelines are presented for properly characterizing the complicated behavior of flexible composites. Moreover, the potential of soft composite laminates for load-coupling applications is shown, which makes soft materials a candidate for new applications such as morphing aircraft wings, artificial muscles, and many other applications that are under investigation by other research groups. To have a direct impact on the advancement of science, the research outputs are published in international peer-reviewed journals, and further, they are disseminated in national and international conferences.

5. REFERENCES

[1] Li S, Lotfi A, Shan Y, Wang KW, Rahn CD, & Bakis CE (eds.). A variable transverse stiffness sandwich structure using fluidic flexible matrix composites (F2MC). International Society for Optics and Photonics; 2008.
[2] Philen M, Shan Y, Bakis C, Wang KW, Rahn C (eds.). Variable stiffness adaptive structures utilizing hydraulically pressurized flexible matrix composites with valve control; 2006.
[3] Shan Y, Philen MP, Bakis CE, Wang K-W, Rahn CD. Nonlinear-elastic finite axisymmetric deformation of flexible matrix composite membranes under internal pressure and axial force. Composites Science and Technology 2006;66(15):3053–63.
[4] Shan Y, Philen M, Lotfi A, Li S, Bakis CE, Rahn CD et al. Variable stiffness structures utilizing fluidic flexible matrix composites. Journal of Intelligent Material Systems and Structures 2009;20(4):443–56.
[5] Connolly F, Wagner DA, Walsh CJ, Bertoldi K. Sew-free anisotropic textile composites for rapid design and manufacturing of soft wearable robots. Extreme Mechanics Letters 2019;27:52–8.
[6] Al-Fahaam HSH. Wearable exoskeleton systems based-on pneumatic soft actuators and controlled by parallel processing: University of Salford; 2019.
[7] Barbarino S, Bilgen O, Ajaj RM, Friswell MI, Inman DJ. A review of morphing aircraft. Journal of Intelligent Material Systems and Structures 2011;22(9):823–77.
[8] Murugan S, Flores EIS, Adhikari S, Friswell MI. Optimal design of variable fiber spacing composites for morphing aircraft skins. Composite Structures 2012;94(5):1626–33.
[9] Sun J, Guan Q, Liu Y, Leng J. Morphing aircraft based on smart materials and structures: A state-of-the-art review. Journal of Intelligent Material Systems and Structures 2016;27(17):2289–312.
[10] Murray G, Gandhi F, Bakis C. Flexible matrix composite skins for one-dimensional wing morphing. Journal of Intelligent Material Systems and Structures 2010;21(17):1771–81.
[11] Lu T, Shi Z, Shi Q, Wang TJ. Bioinspired bicipital muscle with fiber-constrained dielectric elastomer actuator. Extreme Mechanics Letters 2016;6:75–81.
[12] Philen MK, Shan Y, Prakash P, Wang KW, Rahn CD, Zydney AL et al. Fibrillar network adaptive structure with ion-transport actuation. Journal of Intelligent Material Systems and Structures 2007;18(4):323–34.
[13] Bishop-Moser JL. Design of Generalized Fiber-reinforced Elasto-fluidic Systems. (Doctoral dissertation) 2014.
[14] Felt W, Remy CD. A closed-form kinematic model for fiber-reinforced elastomeric enclosures. Journal of Mechanisms and Robotics 2018;10(1):14501.

[15] Felt W, Telleria MJ, Allen TF, Hein G, Pompa JB, Albert K et al. An inductance-based sensing system for bellows-driven continuum joints in soft robots. Autonomous Robots 2017:1–14.
[16] Nampy S, Smith E (eds.). Thermomechanical Behavior and Experimental Testing of Flexible Flexible Matrix Composite Box-Beams with Extension-Twist coupling; 14th Conference on Structural Dynamics and Materials, 2005.
[17] Nampy SN, & Smith EC (eds.). Design evaluation of model and full-scale flexible matrix composites tiltrotor blades with extension-twist coupling. American Helicopter Society; 2006.
[18] Nampy, S. N., & Smith, E. (ed.). Extension-twist coupled tiltrotor blades using flexible matrix composites. American Institute of Aeronautics and Astronautics Inc.(AIAA); 2005.
[19] Tiwari, C., Smith, E., & Bakis, C. (ed.). Non-linear modeling of extension-twist coupled energy absorbing composite tubes; 20th Structural Dynamics and Materials Conference; 2012.
[20] Sensini A, Cristofolini L. Biofabrication of electrospun scaffolds for the regeneration of tendons and ligaments. Materials 2018;11(10):1963.
[21] Benayahu D, Sharabi M, Pomeraniec L, Awad L, Haj-Ali R, Benayahu Y. Unique collagen fibers for biomedical applications. Marine drugs 2018;16(4):102.
[22] McMahan, W., Chitrakaran, V., Csencsits, M., Dawson, D., Walker, I.D., Jones, B.A., Pritts, M., Dienno, D., Grissom, M. and Rahn, C.D. (ed.). Field trials and testing of the OctArm continuum manipulator. IEEE; 2006.
[23] Cao X, Zhang M, Zhang Z, Xu Y, Xiao Y, Li T. Review of soft linear actuator and the design of a dielectric elastomer linear actuator. Acta Mechanica Solida Sinica 2019;32(5):566–79.
[24] Rodriguez DL, Aftosmis MJ, Nemec M, Anderson GR. Optimization of flexible wings with distributed flaps at off-design conditions. Journal of Aircraft 2016;53(6):1731–45.
[25] Holzapfel GA, Gasser TC. A viscoelastic model for fiber-reinforced composites at finite strains: Continuum basis, computational aspects and applications. Computer Methods in Applied Mechanics and Engineering 2001;190(34):4379–403.
[26] Milani AS, Nemes JA. An intelligent inverse method for characterization of textile reinforced thermoplastic composites using a hyperelastic constitutive model. Composites Science and Technology 2004;64(10-11):1565–76.
[27] Merodio J, Saccomandi G. Remarks on cavity formation in fiber-reinforced incompressible non-linearly elastic solids. Computational Materials Science 2006;25(5):778–92.
[28] Ren J, Zhou J, Yuan X. Instability analysis in pressurized three-layered fiber-reinforced anisotropic rubber tubes in torsion. International Journal of Engineering Science 2011;49(4):342–53.
[29] Fereidoonnezhad B, Naghdabadi R, Arghavani J. A hyperelastic constitutive model for fiber-reinforced rubber-like materials. International Journal of Engineering Science 2013;71:36–44.

[30] Chebbi E, Wali M, Dammak F. An anisotropic hyperelastic constitutive model for short glass fiber-reinforced polyamide. International Journal of Engineering Science 2016;106:262–72.
[31] Liu H, Holzapfel GA, Skallerud BH, Prot V. Anisotropic finite strain viscoelasticity: Constitutive modeling and finite element implementation. Journal of the Mechanics and Physics of Solids 2019;124:172–88.
[32] Connolly F, Wagner DA, Walsh CJ, Bertoldi K. Sew-free anisotropic textile composites for rapid design and manufacturing of soft wearable robots. Extreme Mechanics Letters 2019.
[33] Holzapfel GA, Gasser TC, Ogden RW. A New Constitutive Framework for Arterial Wall Mechanics and a Comparative Study of Material Models. Journal of elasticity and the physical science of solids 2000;61(1):1–48. https://doi.org/10.1023/A:1010835316564.
[34] Murphy JG. Transversely isotropic biological, soft tissue must be modelled using both anisotropic invariants. European Journal of Mechanics-A/Solids 2013;42:90–6.
[35] Alhayani AA, Rodríguez J, Merodio J. Competition between radial expansion and axial propagation in bulging of inflated cylinders with application to aneurysms propagation in arterial wall tissue. International Journal of Engineering Science 2014;85:74–89.
[36] Tricerri P, Dedè L, Gambaruto A, Quarteroni A, Sequeira A. A numerical study of isotropic and anisotropic constitutive models with relevance to healthy and unhealthy cerebral arterial tissues. International Journal of Engineering Science 2016;101:126–55.
[37] Chaimoon K, Chindaprasirt P. An anisotropic hyperelastic model with an application to soft tissues. European Journal of Mechanics-A/Solids 2019;78:103845.
[38] Wagner DR, Lotz JC. Theoretical model and experimental results for the nonlinear elastic behavior of human annulus fibrosus. Journal of orthopaedic research 2004;22(4):901–9.
[39] Peng XQ, Guo ZY, Moran B. An anisotropic hyperelastic constitutive model with fiber-matrix shear interaction for the human annulus fibrosus. J. Appl. Mech. 2006;73(5):815–24.
[40] Peng X, Guo G, Zhao N. An anisotropic hyperelastic constitutive model with shear interaction for cord–rubber composites. Composites Science and Technology 2013;78:69–74.
[41] Guo ZY, Peng XQ, Moran B. A composites-based hyperelastic constitutive model for soft tissue with application to the human annulus fibrosus. Journal of the Mechanics and Physics of Solids 2006;54(9):1952–71.

[42] Gong Y, Peng X, Yao Y, Guo Z. An anisotropic hyperelastic constitutive model for thermoplastic woven composite prepregs. Composites Science and Technology 2016;128:17–24.
[43] Gong Y, Yan D, Yao Y, Wei R, Hu H, Xu P et al. An anisotropic hyperelastic constitutive model with tension–shear coupling for woven composite reinforcements. International Journal of Applied Mechanics 2017;9(06):1750083.
[44] Melnik AV, Luo X, Ogden RW. A generalised structure tensor model for the mixed invariant I8. International Journal of Non-Linear Mechanics 2018. https://doi.org/10.1016/j.ijnonlinmec.2018.08.018.
[45] Holzapfel GA, Ogden RW. An Arterial Constitutive Model Accounting for Collagen Content and Cross-Linking. Journal of the Mechanics and Physics of Solids 2019:103682.
[46] Karger-Kocsis J, Mahmood H, Pegoretti A. Recent advances in fiber/matrix interphase engineering for polymer composites. Progress in Materials Science 2015;73:1–43.
[47] Kim J-K, Hodzic A. Nanoscale characterisation of thickness and properties of interphase in polymer matrix composites. The Journal of Adhesion 2003;79(4):383–414.
[48] Palola S, Vuorinen J, Noordermeer JWM, Sarlin E. Development in Additive Methods in Aramid Fiber Surface Modification to Increase Fiber-Matrix Adhesion: A Review. Coatings 2020;10(6):556.
[49] Drzal LT, Madhukar M. Fibre-matrix adhesion and its relationship to composite mechanical properties. J Mater Sci 1993;28(3):569–610.
[50] Mansouri MR, Beter J, Fuchs PF, Schrittesser B, Pinter G. Quantifying matrix-fiber mechanical interactions in hyperelastic materials. International Journal of Mechanical Sciences 2021;195:106268. https://doi.org/10.1016/j.ijmecsci.2021.106268.
[51] Schriefl AJ, Schmidt T, Balzani D, Sommer G, Holzapfel GA. Selective enzymatic removal of elastin and collagen from human abdominal aortas: Uniaxial mechanical response and constitutive modeling. Acta biomaterialia 2015;17:125–36.
[52] Weisbecker H, Viertler C, Pierce DM, Holzapfel GA. The role of elastin and collagen in the softening behavior of the human thoracic aortic media. J Biomech 2013;46(11):1859–65.
[53] Famaey N, Vander Sloten J, Kuhl E. A three-constituent damage model for arterial clamping in computer-assisted surgery. Biomechanics and modeling in mechanobiology 2013;12(1):123–36.
[54] Rodríguez JF, Cacho F, Bea JA, Doblaré M. A stochastic-structurally based three dimensional finite-strain damage model for fibrous soft tissue. Journal of the Mechanics and Physics of Solids 2006;54(4):864–86.

[55] Natali AN, Pavan PG, Carniel EL, Dorow C. A transversally isotropic elasto-damage constitutive model for the periodontal ligament. Computer methods in biomechanics and and biomedical engineering 2003;6(5-6):329–36.
[56] Calvo B, Peña E, Martinez MA, Doblaré M. An uncoupled directional damage model for fibred biological soft tissues. Formulation and computational aspects. Int. J. Numer. Meth. Engng 2007;69(10):2036–57.
[57] Peña E. Prediction of the softening and damage effects with permanent set in fibrous biological materials. Journal of the Mechanics and Physics of Solids 2011;59(9):1808–22.
[58] Peña E. Computational aspects of the numerical modelling of softening, damage and permanent set in soft biological tissues. Computers & Structures 2014;130:57–72.
[59] Dorfmann A, Ogden RW. A constitutive model for the Mullins effect with permanent set in particle-reinforced rubber. International Journal of Solids and Structures 2004;41(7):1855–78.
[60] Ogden RW, Roxburgh DG. A pseudo–elastic model for the Mullins effect in filled rubber. Proceedings of the Royal Society A: Mathematical, Physical and Engineering Sciences 1999;455(1988):2861–77.
[61] Volokh KY. Hyperelasticity with softening for modeling materials failure. Journal of the Mechanics and Physics of Solids 2007;55(10):2237–64.
[62] Volokh KY. Prediction of arterial failure based on a microstructural bi-layer fiber–matrix model with softening. J Biomech 2008;41(2):447–53.
[63] Gültekin O, Dal H, Holzapfel GA. Numerical aspects of anisotropic failure in soft biological tissues favor energy-based criteria: A rate-dependent anisotropic crack phase-field model. Computer Methods in Applied Mechanics and Engineering 2018;331:23–52.
[64] Raina A, Miehe C. A phase-field model for fracture in biological tissues. Biomechanics and modeling in mechanobiology 2016;15(3):479–96.
[65] Natali AN, Pavan PG, Carniel EL, Lucisano ME, Taglialavoro G. Anisotropic elasto-damage constitutive model for the biomechanical analysis of tendons. Med Eng Phys 2005;27(3):209–14.
[66] Peña E. Damage functions of the internal variables for soft biological fibred tissues. Mechanics Research Communications 2011;38(8):610–5.
[67] Holzapfel GA, Fereidoonnezhad B. Modeling of damage in soft biological tissues. In: Biomechanics of Living Organs. Elsevier; 2017, p. 101–123.
[68] Peña E, Peña JA, Doblaré M. On the Mullins effect and hysteresis of fibered biological materials: A comparison between continuous and discontinuous damage models. International Journal of Solids and Structures 2009;46(7-8):1727–35.

[69] Balzani D, Brinkhues S, Holzapfel GA. Constitutive framework for the modeling of damage in collagenous soft tissues with application to arterial walls. Computer Methods in Applied Mechanics and Engineering 2012;213:139–51.
[70] Peña E, Calvo B, Martínez MA, Doblaré M. On finite-strain damage of viscoelastic-fibred materials. Application to soft biological tissues. Int. J. Numer. Meth. Engng 2008;74(7):1198–218.
[71] Ehret AE, Itskov M. Modeling of anisotropic softening phenomena: application to soft biological tissues. International Journal of Plasticity 2009;25(5):901–19.
[72] Schmidt T, Balzani D, Holzapfel GA. Statistical approach for a continuum description of damage evolution in soft collagenous tissues. Computer Methods in Applied Mechanics and Engineering 2014;278:41–61.
[73] Maher E, Creane A, Lally C, Kelly DJ. An anisotropic inelastic constitutive model to describe stress softening and permanent deformation in arterial tissue. J Mech Behav Biomed Mater 2012;12:9–19.
[74] Ghasemi M, Nolan DR, Lally C. An investigation into the role of different constituents in damage accumulation in arterial tissue and constitutive model development. Biomechanics and modeling in mechanobiology 2018;17(6):1757–69.
[75] Fung YC, Fronek K, Patitucci P. Pseudoelasticity of arteries and the choice of its mathematical expression. American Journal of Physiology-Heart and Circulatory Physiology 1979;237(5):H620-H631.
[76] Franceschini G, Bigoni D, Regitnig P, Holzapfel GA. Brain tissue deforms similarly to filled elastomers and follows consolidation theory. Journal of the Mechanics and Physics of Solids 2006;54(12):2592–620.
[77] Doblaré M. An anisotropic pseudo-elastic approach for modelling Mullins effect in fibrous biological materials. Mechanics Research Communications 2009;36(7):784–90.
[78] Weisbecker H, Pierce DM, Regitnig P, Holzapfel GA. Layer-specific damage experiments and modeling of human thoracic and abdominal aortas with non-atherosclerotic intimal thickening. J Mech Behav Biomed Mater 2012;12:93–106.
[79] Fereidoonnezhad B, Naghdabadi R, Holzapfel GA. Stress softening and permanent deformation in human aortas: continuum and computational modeling with application to arterial clamping. J Mech Behav Biomed Mater 2016;61:600–16.
[80] Mo C, Jiang Y, Raney JR. Microstructural evolution and failure in short fiber soft composites: experiments and modeling. Journal of the Mechanics and Physics of Solids 2020:103973.
[81] Rausch MK, Humphrey JD. A microstructurally inspired damage model for early venous thrombus. J Mech Behav Biomed Mater 2016;55:12–20.

[82] Schmidt T, Balzani D. Relaxed incremental variational approach for the modeling of damage-induced stress hysteresis in arterial walls. J Mech Behav Biomed Mater 2016;58:149–62.
[83] Chagnon G, Rebouah M, Favier D. Hyperelastic Energy Densities for Soft Biological Tissues: A Review. J Elast 2015;120(2):129–60.
[84] Gracia LA, Peña E, Royo JM, Pelegay JL, Calvo B. A comparison between pseudo-elastic and damage models for modelling the Mullins effect in industrial rubber components. Mechanics Research Communications 2009;36(7):769–76.
[85] Guo Z, Sluys LJ. Computational modelling of the stress-softening phenomenon of rubber-like materials under cyclic loading. European Journal of Mechanics-A/Solids 2006;25(6):877–96.

PART II: COLLECTION OF PAPERS

European Journal of Mechanics / A Solids 85 (2021) 104081

Contents lists available at ScienceDirect

European Journal of Mechanics / A Solids

journal homepage: http://www.elsevier.com/locate/ejmsol

The contribution of mechanical interactions to the constitutive modeling of fiber-reinforced elastomers

M.R. Mansouri [a,*], P.F. Fuchs [a], J.C. Criscione [b], B. Schrittesser [a], J. Beter [a]

[a] Polymer Competence Center Leoben GmbH, 8700, Roseggerstreet 12, Leoben, Austria
[b] Department of Biomedical Engineering, Texas A&M University, College Station, TX, 77843-3120, College Station, USA

ARTICLE INFO

Keywords:
Mechanical interaction potential
Constitutive behavior
Fiber-reinforced elastomers
Non-symmetric deformations
Composite laminates

ABSTRACT

Hyperelastic fiber-reinforced materials are conventionally modeled based on the contributions of their constituent materials. A unified invariant-base constitutive model, named Matrix-Fiber-Interaction (MFI) model, is proposed to take into account particularly the mechanical interaction contribution of the constituent materials in fiber-reinforced elastomers with two fiber families. Its high predictive capability for the modeling of the behavior of composites with different material anisotropy is verified by several experiments. This model along with its structurally based framework of material characterization allows measuring distinct contributions of the matrix, fiber, and mechanical interactions in the sense that the latter can be determined regardless of the functional form of the fiber potential. Therefore, in this paper, the MFI model implemented in a user-defined subroutine is used to highlight the importance of mechanical interaction potential. Using three representative examples: uniaxial extension of single-layer plates with different material anisotropy, inflation-extension of a thin cylindrical tube, and load-coupling behaviors in composite laminates, its effect is analyzed. The comparisons of experiments with simulation results underline the prediction quality improvement using the interaction potential in the modeling of single-layer composites. For the two latter deformations, the simulation results comparatively indicate the effect of mechanical interaction potential for the modeling of more complicated structures.

1. Introduction

Flexible fiber-reinforced materials, including biological organs and inorganic composites, are considered as hyperelastic continuums in the sense that it is assumed there exists a potential function Ψ which represents the total stored energy of the continuum during the deformation. The majority of the works in the field of flexible fiber-reinforced materials are taken into account the potentials of the individual constituent materials, i.e. soft matrix and fibers, to model their constitutive behaviors. The papers by, for example, Holzapfel and Gasser (2001), Milani and Nemes (2004), Merodio and Saccomandi (2006), Ren et al. (2011), Fereidoonnezhad et al. (2013), Chebbi et al. (2016), Liu et al. (2019), Connolly et al. (2019) accounted the contributions of the matrix and fibers as constituent materials for modeling inorganic fiber-reinforced composites. In addition to, the works by Holzapfel et al. (2000), Murphy (2013), Alhayani et al. (2014), Tricerri et al. (2016), Chaimoon and Chindaprasirt (2019) are examples in which the contributions of the constituent materials are only considered for mechanical behavior modeling of soft biological tissues. Among others, Holzapfel-Gosser-Ogden (HGO) model (Holzapfel et al., 2000) provides a nice comparison between various relations for fibrous biological tissues. This model is also used frequently for constitutive modeling of the inorganic materials. We make no attempt to list a large number of the works done in this subject.

A few works considered the mechanical interaction potential for constitutive modeling of flexible fiber-reinforced materials. The interaction potential is introduced for the first time by Wagner and Lotz (2004) and Peng et al. (2006) for modeling the mechanical behavior of human annulus fibrosus. Since then, the interaction potential appears to be taken into account for modeling of cord-rubber composite (Peng et al., 2013), biological tissues (Guo et al., 2006), soft inorganic composites (Gong et al., 2016), and dry fabrics (Gong et al., 2017). Recently, Melnik et al. (2018) and Holzapfel and Ogden (2019) considered an interaction potential associated with coupling between dispersed collagens and cross-links for modeling of soft tissues. However, very little is known about the efficacy of including interaction potential in the constitutive behavior modeling of flexible fiber-reinforced materials.

The main goal of the present study is to propose a unified invariant-

* Corresponding author.
E-mail address: mohammad.mansouri@pccl.at (M.R. Mansouri).

https://doi.org/10.1016/j.euromechsol.2020.104081
Received 21 February 2020; Received in revised form 6 July 2020; Accepted 11 July 2020
Available online 6 August 2020

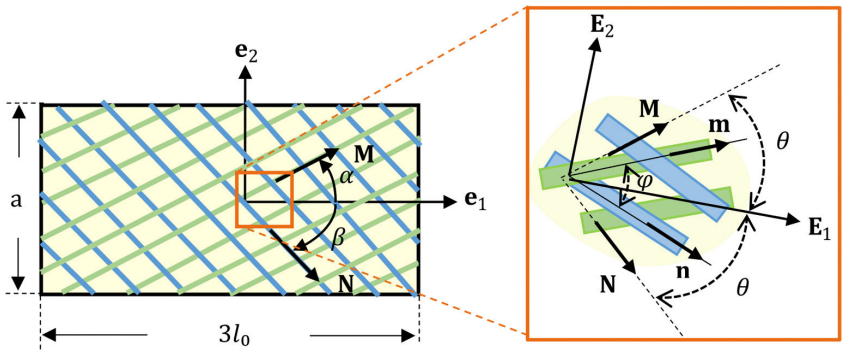

Fig. 1. Model geometry of the composite strips, left, with two fiber families $\boldsymbol{M} = \cos\theta\,\boldsymbol{E}_1 + \sin\theta\,\boldsymbol{E}_2$ and $\boldsymbol{N} = \cos\theta\,\boldsymbol{E}_1 - \sin\theta\,\boldsymbol{E}_2$, which are initially located in the reference configuration, right. The θ is half of the angle subtended by $\boldsymbol{M}$ and $\boldsymbol{N}$. Under a uniaxial extension in the loading direction $\boldsymbol{e}_1$, they are mapped to the spatial line elements $\boldsymbol{m}$ and $\boldsymbol{n}$ in the final configuration with the angle ϕ between. For simplicity, a fixed coordinate system $\{\boldsymbol{e}_1, \boldsymbol{e}_2, \boldsymbol{e}_3\}$ is here adopted for specifying the loading direction.

base constitutive model, so-called the MFI model, on the basis of extensional- and angular-base deformation invariants to take into account particularly the contribution of the mechanical interactions between constituent materials of the fiber-reinforced elastomers with two fiber families. It introduces a structurally based framework for characterizing the mechanical interactions regardless of the functional form of the fiber potential. Therefore, during a specific deformation, the contribution of mechanical interactions can be obtained without being perturbed by other contributions. Moreover, we take advantage of this model and capabilities of existing commercial software for nonlinear analysis in order to highlight for the first time the importance of the mechanical interaction potential in constitutive modeling of fiber-reinforced elastomers.

2. Model description

2.1. Kinematics

In this section, the notation and fundamental concepts of nonlinear continuum mechanics are outlined in order to describe the MFI constitutive model, the elasticity tensors and corresponding Cauchy stresses. Consider a continuum body B_r in the reference configuration of a material body. It is supposed that any material point be labelled by its position vector $\mathbf{X}$ in B_r. Let the body be deformed into the new configuration B so that the material point $\mathbf{X}$ takes up the position $\mathbf{x}$. This motion is introduced by the mapping $\mathbf{x} = \chi(\mathbf{X})$. The gradient of χ is defined by $\mathbf{F}(\mathbf{X}) = \mathrm{Grad}\ \mathbf{x}$ and referred to as the deformation gradient tensor that its determinant $J = \det\mathbf{F}(\mathbf{X}) > 0$ is called the local volume ratio. In terms of $\mathbf{F}$ the right Cauchy-Green strain tensor is given by $\mathbf{C} = \mathbf{F}^{\mathrm{T}}\mathbf{F}$ with the corresponding first and second invariants as

$$I_1 = \mathrm{tr}\,\mathbf{C} \quad \text{and} \quad I_2 = \frac{1}{2}\left[(\mathrm{tr}\mathbf{C})^2 - \mathrm{tr}\left(\mathbf{C}^2\right)\right] \tag{1}$$

Consider two material line elements in a fiber-reinforced material initially aligned along the unit vectors defined as $\mathbf{M} = \cos\theta\,\mathbf{E}_1 + \sin\theta\,\mathbf{E}_2$ and $\mathbf{N} = \cos\theta\,\mathbf{E}_1 - \sin\theta\,\mathbf{E}_2$, which are initially located in reference configuration, as shown in the right-hand side of Fig. 1. The parameter θ is half of the angle subtended by $\mathbf{M}$ and $\mathbf{N}$. They are mapped to the spatial line elements $\mathbf{m}$ and $\mathbf{n}$ in the final configuration by deformation gradient $\mathbf{F}$ through the motion $\mathbf{x} = \chi(\mathbf{X})$. During this deformation, the material line elements might experience a change of both the element length and the angle. Spencer (1984) introduced the pseudo-invariants for fiber-reinforced materials as follows,

$$I_4(\mathbf{M}) = \mathbf{C} : \mathbf{M} \otimes \mathbf{M}, \quad I_6(\mathbf{N}) = \mathbf{C} : \mathbf{N} \otimes \mathbf{N}, \quad I_8(\mathbf{M}, \mathbf{N}) = \mathbf{C} : \mathbf{M} \otimes \mathbf{N} \tag{2}$$

The pseudo-invariants I_4 and I_6 capture information about the square of stretch in the fiber directions $\mathbf{M}$ and $\mathbf{N}$, respectively. In the original work of Criscione and Hunter (2003), they introduced a scalar $\mathscr{B}$ that represents a change of the angle between equally deformed fibers. They found a relation between $\mathscr{B}$, the angle between deformed fibers (denoted by ϕ), and the right-hand side of the relations in (2) as

$$\cos\phi = \frac{\mathbf{C} : \mathbf{M} \otimes \mathbf{N}}{\sqrt{\mathbf{C} : \mathbf{M} \otimes \mathbf{M}}\sqrt{\mathbf{C} : \mathbf{N} \otimes \mathbf{N}}} = \frac{\mathscr{B}^2\cos^2\theta - \mathscr{B}^{-2}\sin^2\theta}{\mathscr{B}^2\cos^2\theta + \mathscr{B}^{-2}\sin^2\theta} \tag{3}$$

Upon replacing the relations (2) in (3), an angular-base invariant set in terms of the strain invariants as $I_8^* = I_8/\sqrt{I_4\ I_6} = \cos\phi$ is considered here to take into account the current angle between deformed fibers.

2.2. Modeling the mechanical interactions of the constituent materials

The extensional-base invariants I_4 and I_6 as well as the angular-base invariant I_8^* are employed by the fibers and mechanical interaction potentials, respectively, to form the MFI constitutive model (after the first initials of the contributions' names, i.e. Matrix-Fiber-Interaction) as

$$\Psi(\mathbf{C}, \{\mathbf{M}, \mathbf{N}\}) = \Psi_{\mathrm{M}}(I_1) + \Psi_{\mathrm{F}}(I_4,\ I_6) + \Psi_{\mathrm{I}}\left(I_8^*\right) - \frac{1}{2}q(I_4 - 1) - \frac{1}{2}r(I_6 - 1)$$
$$\begin{cases} I.\ \text{inextensible fibers} & I_4,\ I_6 = 1 \\ II.\ \text{extensible fibers} & q, r = 0 \end{cases} \tag{4}$$

with the respective deformation gradient

$$\mathbf{F} = \mathbf{Q}\,\mathbf{f} \tag{5}$$

where $\mathbf{Q}$ is a proper orthogonal tensor such that $\mathbf{Q}^{\mathrm{T}}\mathbf{Q} = \mathbf{I}$ and $\det\mathbf{Q} = 1$. The scalar quantities q and r are fiber tensions as reactions associated with the inextensibility constraints $I_4 = 1$ and $I_6 = 1$, respectively. Adding the term $\frac{1}{2}q(I_4 - 1) + \frac{1}{2}r(I_6 - 1)$ in Eq. (4) is relied on the fact that the mechanical interaction potential is a result of the rotation of fibers and not of the fibers' elongation. This term provides a structurally based framework for characterization of the mechanical interaction properties so as to enable them to be found regardless of the functional form of fibers potential. This experimental framework will be further elaborated in upcoming works. It is emphasized that since the fibers are generally

assumed to be extensible, this term is not considered for the computational implementation of the model, i.e.

For an incompressible and thin composite, it is straightforward to find specific forms of the deformation gradients associated with the constraints I and II, defined in Eq. (4), as $\mathbf{F}_I = \mathbf{Q}\,\mathbf{f}_\phi^*$ and $\mathbf{F}_{II} = \mathbf{Q}\,\mathbf{f}_\mathrm{f}^*$, respectively (it is shown in detail in Appendix A). $\mathbf{f}_\phi^*$ represents specifically change of the angle between fibers while $\mathbf{f}_\mathrm{f}^*$ accounts the elongation of the fibers. Accordingly, the constitutive model in Eq. (4) is specialized as

$$\Psi_I = \Psi_\mathrm{M}(I_1,\ I_2) + \Psi_\tau(I_8^*) - \frac{1}{2}q(I_4-1) - \frac{1}{2}r(I_6-1), \qquad \mathbf{F}_I = \mathbf{Q}\,f_\phi^* \tag{6}$$

$$\Psi_{II} = \Psi_\mathrm{M}(I_1,\ I_2) + \Psi_\mathrm{F}(I_4,\ I_6), \qquad \mathbf{F}_{II} = \mathbf{Q}\,\mathbf{f}_\mathrm{f}^* \tag{7}$$

The relations (6) and (7) introduce a new framework for material characterization of the mechanical interaction properties and fibers, respectively, which will be discussed in detail in upcoming works.

2.3. Energy functions

In a fiber-reinforced elastomer, as mentioned by Holzapfel and Ogden (2009), it is convenient and customary to make no distinction between the directions $\mathbf{M}$ and $-\mathbf{M}$ ($\mathbf{N}$ and $-\mathbf{N}$). Since $\Psi_\mathrm{F} = \Psi_\mathrm{F}(\mathbf{C}, \mathbf{M}\otimes\mathbf{M}, \mathbf{N}\otimes\mathbf{N})$, the fiber potential is an even function while $\Psi_\tau = \Psi_\tau(\mathbf{C}, \mathbf{M}\otimes\mathbf{N})$ is an odd function. Therefore, the interaction potential Ψ_τ can depend on the sign of arbitrary directions. To ensure Ψ_τ is independent of the sign of fiber directions and in order to predict a stress-free state in the un-deformed configuration, i.e. $\partial\Psi/\partial\mathbf{C} = 0$ when $\mathbf{C} = \mathbf{I}$, as well as the observation of the experimental trends, the angular-base set I_8^* is employed by an exponential-polynomial function as follows to form the interaction potential, i.e.

$$\Psi_\tau = \frac{c_1}{2c_2}\left[\exp\left(c_2\left(I_8^* - \cos(2\theta)\right)^2\right) - 1\right] + c_3\left(I_8^* - \cos(2\theta)\right)^2 \tag{8}$$

where c_1 and c_3 are positive material parameters with the dimension of stress and c_2 is a positive dimensionless parameter. The constant $\cos(2\theta)$ is the cosine of the angle between two line elements in fiber directions at un-deformed configuration. The polynomial term in the right-hand side of the relation (8) enhances greatly the accuracy of the material calibration that is discussed in Section 3. The constitutive behavior of the constituent materials has been well established and is not critical here. So, the isotropic neo-Hookean model (Treloar, 1943) for matrix and the anisotropic model proposed by Holzapfel et al. (2000) are used, i.e.

$$\Psi_\mathrm{F} = \frac{k_1}{2k_2}\sum_{i=4,6}\left[\exp\left(k_2(I_i-1)^2\right) - 1\right], \qquad \Psi_\mathrm{M} = c_{10}(I_1-3) - p(J-1) \tag{9}$$

where k_1 and c_{10} are positive material parameters with the dimension of stress and k_2 is a positive dimensionless material parameter. The scalar p serves as an indeterminate Lagrange multiplier which can be identified as hydrostatic pressure.

Table 1
Material constants of the MFI model.

Contribution	c_{10}, MPa	k_1, MPa	k_2, –	c_1, MPa	c_2, –	c_3, MPa
Matrix	0.380					
Fiber		697.0	1.125e-11			
Interaction				0.0355	9.6790	1.3770

2.4. Cauchy stress

In the following, the decoupled forms $\boldsymbol{\sigma}_I$ and $\boldsymbol{\sigma}_{II}$ of the overall Cauchy stress tensors $\boldsymbol{\sigma}$ corresponding to the potentials (6), (7), and (4), respectively, are presented. A push-forward operation on the second Piola-Kirchhoff stress tensor $\mathbf{S} = 2\partial\Psi(\mathbf{C},\ \{\mathbf{M},\mathbf{N}\})/\partial\mathbf{C}$ with $\mathbf{F}$ results in the Cauchy stress tensor $\boldsymbol{\sigma}$ defined as

$$\boldsymbol{\sigma} = 2\mathbf{F}\frac{\partial\Psi(\mathbf{C},\ \{\mathbf{M},\mathbf{N}\})}{\partial\mathbf{C}}\mathbf{F}^\mathrm{T} = -p\mathbf{I} + 2\frac{\partial\Psi_\mathrm{M}}{\partial I_1}\mathbf{b} + 2\frac{\partial\Psi_\mathrm{F}}{\partial I_4}(\mathbf{m}\otimes\mathbf{m}) + 2\frac{\partial\Psi_\mathrm{F}}{\partial I_6}(\mathbf{n}\otimes\mathbf{n}) + \frac{\partial\Psi_\tau}{\partial I_8^*}\left(\frac{\mathbf{m}\otimes\mathbf{n}+\mathbf{n}\otimes\mathbf{m}}{\sqrt{I_4 I_6}} - I_8^*\left(\frac{\mathbf{m}\otimes\mathbf{m}}{I_4} + \frac{\mathbf{n}\otimes\mathbf{n}}{I_6}\right)\right), \qquad \mathbf{F} = \mathbf{Q}\,\mathbf{f} \tag{10}$$

with $\mathbf{b} = \mathbf{F}\mathbf{F}^\mathrm{T}$, $\mathbf{m} = \mathbf{F}\mathbf{M}$, and $\mathbf{n} = \mathbf{F}\mathbf{N}$ with the components defined as

$$\{\mathbf{m}\} = \{\mathbf{F}\mathbf{M}\} = \begin{bmatrix} m_1 \\ m_2 \\ m_3 \end{bmatrix} = \begin{bmatrix} F_{11}\cos\theta + F_{12}\sin\theta \\ F_{21}\cos\theta + F_{22}\sin\theta \\ 0 \end{bmatrix}, \quad \{\mathbf{n}\} = \{\mathbf{F}\mathbf{N}\} = \begin{bmatrix} n_1 \\ n_2 \\ n_3 \end{bmatrix} = \begin{bmatrix} F_{11}\cos\theta - F_{12}\sin\theta \\ F_{21}\cos\theta - F_{22}\sin\theta \\ 0 \end{bmatrix} \tag{11}$$

The Cauchy stress tensors $\boldsymbol{\sigma}_I$ corresponding to the potential (6) can be determined as

$$\boldsymbol{\sigma}_I = -p\mathbf{I} + 2\frac{\partial\Psi_I}{\partial I_1}\mathbf{b} + \frac{\partial\Psi_I}{\partial I_8^*}\left(\mathbf{m}\otimes\mathbf{n} + \mathbf{n}\otimes\mathbf{m} - I_8^*(\mathbf{m}\otimes\mathbf{m} + \mathbf{n}\otimes\mathbf{n})\right) - \frac{1}{2}q(\mathbf{m}\otimes\mathbf{m}) - \frac{1}{2}r(\mathbf{n}\otimes\mathbf{n}), \quad \mathbf{F}_I = \mathbf{Q}\,\mathbf{f}_\phi^* \tag{12}$$

The indeterminate terms $\mathbf{q} = q(\mathbf{m}\otimes\mathbf{m})$ and $\mathbf{r} = r(\mathbf{n}\otimes\mathbf{n})$ are identified as reaction stresses associated with the fibers inextensibility constraints, with the fiber tensions q and r. The term $1/2\mathbf{q} + 1/2\mathbf{r}$ simplifies the interaction calibration procedure and is not generally considered for computational implementation of the model. The same operation on Ψ_{II} results in

$$\boldsymbol{\sigma}_{II} = -p\mathbf{I} + 2\frac{\partial\Psi_{II}}{\partial I_1}\mathbf{b} + 2\frac{\partial\Psi_{II}}{\partial I_4}(\mathbf{m}\otimes\mathbf{m}) + 2\frac{\partial\Psi_{II}}{\partial I_6}(\mathbf{n}\otimes\mathbf{n}), \quad \mathbf{F}_{II} = \mathbf{Q}\,\mathbf{f}_\mathrm{f}^* \tag{13}$$

3. Constitutive parameter identification

Depending on the chosen coordinate system and complexity of the adopted deformation, the material calibration procedure can become straightforward or difficult. In this work, by adopting simple deformation states the components of the deformation gradient $\mathbf{F}_I$ and $\mathbf{F}_{II}$,

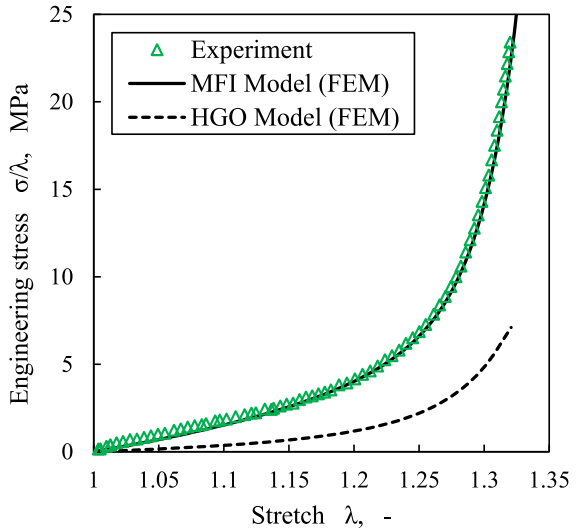

Fig. 2. Comparison of the experimental results of symmetric deformations ($\alpha = -\beta = \pi/4$) with finite element simulation results obtained using the MFI model for the uniaxial extensions in the e_1 direction (The material properties provided in Table 1 are used for the simulations). Additionally, the MFI model is compared with the HGO model for the same deformation.

introduced in the previous section, can be easily determined. Upon obtaining their components, the constitutive equations (6) and (7) are rebuilt so as to reconstruct the Cauchy stresses defined in (12) and (13), respectively.

Constituent materials: The material properties of the matrix can be found by performing uniaxial deformation (for more accurate results equi-biaxial tests can be performed optionally) on a pure matrix. For a detailed discussion on the constitutive modeling and experimental characterization of isotropic elastomers, the readers are referred to, for example, Mansouri and Darijani (2014) and Mansouri et al. (2017). Keeping the material parameters of the matrix, unidirectional composites are subjected to uniaxial tests along the fibers direction with a stretch of λ to calibrate the material constants of the fibers potential Ψ_F, i.e. k_1 and k_2. The Cauchy stress (13) with its corresponding deformation gradient $\mathbf{F}_{II} = \mathbf{Q}\,\mathbf{f}_f^*$ is used. For this specific deformation $\mathbf{Q} = \mathbf{I}$ and the deformation gradient is simplified to $\mathbf{F}_{II} = \mathbf{f}_f^* = \mathrm{diag}[\lambda, \lambda^{-1/2}, \lambda^{-1/2}]$. The material properties of the matrix and fibers are given in Table 1.

Mechanical Interactions: Silicone/glass fiber composites with two fiber families, aligned in the $\mathbf{M} = \cos\alpha\,\mathbf{e}_1 + \sin\alpha\mathbf{e}_2$ and $\mathbf{N} = \cos\beta\mathbf{e}_1 + \sin\beta\mathbf{e}_2$ directions with $\alpha = \beta = -\pi/4$, are subjected to uniaxial extensions in the loading direction $\mathbf{e}_1$ to evaluate the interaction properties. The model geometry of the composite strips with a dimension of $a \times 3l_0$ is shown in the left-hand side of Fig. 1, where $l_0 = a/\tan\alpha$ and a is the width of the strips. The stress-stretch experimental results of this symmetric deformation are given in Fig. 2. A fixed coordinate system such as $\{\mathbf{e}_1, \mathbf{e}_2, \mathbf{e}_3\}$ is adopted for specifying the loading direction. Bearing in mind that the interaction mechanism is activated due to the rotation of fibers and not of the fibers' elongation, the kinematic constraint I with respective Cauchy stress σ_I defined in (12) is recalled wherein $\mathbf{F}_I = \mathbf{Q}\,\mathbf{f}_\phi^*$. For this specific deformation $\mathbf{Q} = \mathbf{I}$ and the deformation gradient is given by

$$\mathbf{F}_I = \mathbf{f}_\phi^* = \begin{bmatrix} \lambda & 0 & 0 \\ 0 & \sqrt{2-\lambda^2} & 0 \\ 0 & 0 & \dfrac{1}{\lambda\sqrt{2-\lambda^2}} \end{bmatrix} \tag{14}$$

where λ is the value of the uniaxial stretch in the loading direction $\mathbf{E}_1$. In order to obtain the unknown scalars of the Cauchy stress (12) with respect to its deformation gradient specified in the above equation, the stress-free boundary conditions are enforced. Using $(\sigma_I)_{33} = 0$ the scalar $p = 2B_{33}\partial\Psi/\partial I_1$ can be determined. The scalars q and r in the Cauchy stress (12) can be also found from $(\sigma_I)_{22} = 0$. Since both families of fibers have the same contributions to the deformation, thus

$$|q| = |\ r| = \frac{2\frac{\partial\Psi_I}{\partial I_1}(b_{22} - b_{33}) + \frac{\partial\Psi_I}{\partial I_8^*}\left(2m_2n_2 - I_8^*\left(m_2^2 + n_2^2\right)\right)}{m_2^2 + n_2^2} \tag{15}$$

Replacing the values of the scalars p, q, and r in (12), the only non-zero component of the Cauchy stress can be determined as

$$\sigma_I = 2\frac{\partial\Psi_I}{\partial I_1}\left(b_{11} - b_{33} - (b_{22} - b_{33})\frac{m_1^2 + n_1^2}{m_2^2 + n_2^2}\right) + 2\frac{\partial\Psi_I}{\partial I_8^*}\left(m_1n_1 - m_2n_2\frac{m_1^2 + n_1^2}{m_2^2 + n_2^2}\right) \tag{16}$$

where $I_1 = \mathrm{tr}(\mathbf{C}_I)$, $I_8^* = \mathbf{C}_I : \mathbf{M} \otimes \mathbf{N}$. The values of m_i, n_i, and b_{ij} $i, j \in \{1, 2, 3\}$, are calculated based on the deformation gradient defined in (14). Finally, replacing these values, the Cauchy stress (16) is simplified to

$$\sigma_I = 2\lambda^2\left(\lambda^2 - 1\right)\left(\frac{2\mu}{\lambda^4\left(2 - \lambda^2\right)^2} + c_1\exp\left(c_2\left(\lambda^2 - 1\right)^2\right) + 2c_3\right) \tag{17}$$

This explicit relation for the Cauchy stress in terms of λ, which is reconstructed within the introduced framework, is used for calibration of the mechanical interaction potential to the experimental results. To do this, the Cauchy stress (17), is fitted to the stress-stretch experimental results of the symmetric deformations provided in Fig. 2 using a non-linear least-squares optimization tool from Matlab. The unknown material constants of the mechanical interaction potential obtained from the calibration procedure are provided in Table 1.

4. Verification of the constitutive behavior

The mechanical interaction potential (Ψ_τ) so calibrated within the

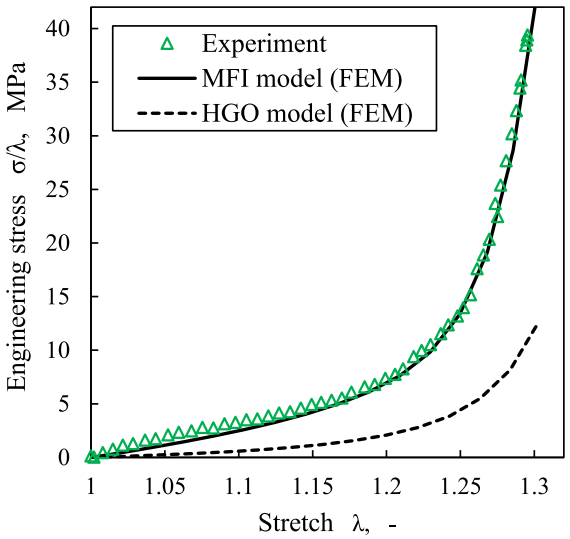

Fig. 3. Comparison of the experimental results of non-symmetric deformations ($\alpha = \pi/6$, $\beta = -\pi/3$) with finite element simulation results obtained using the MFI model for the uniaxial extensions in the e_1 direction (The material properties provided in Table 1 are used for the simulations). Additionally, the MFI model is compared with the HGO model for the same deformation.

introduced framework of material characterization (refer to the previous section) and the calibrated constituent potentials (Ψ_M and Ψ_F) are now summed up to form the MFI constitutive model presented in Eq. (4). The MFI model is now verified against two symmetric and non-symmetric deformation states. In doing so, the model is first implemented in the FEM commercial program ABAQUS using a user-defined interface UMAT (the implementation of the model using decoupled forms of the Cauchy stress and elasticity tensors in an Eulerian description is discussed in the upcoming works). The material properties provided in Table 1 are used for the finite element simulations. The geometries are discretized with 3D reduced integration, eight-node linear solid elements with hybrid formulation (C3D8RH). To enforce the incompressibility condition, a large value of the bulk modulus $\kappa = 10^5$ Pa is adopted. The model geometry and the boundary conditions used for the simulations are initially the same as those used in the experiments.

The stress-stretch experimental results provided in Fig. 2 are used as symmetric deformations ($\alpha = \beta = -\pi/4$) for comparison of the model with finite element simulation results. The proposed model is further evaluated in Fig. 3 with comparison to non-symmetric deformation states. In this case, the composites with two fiber families, aligned in the $\mathbf{M} = \cos\alpha\,\mathbf{e}_1 + \sin\alpha\mathbf{e}_2$ and $\mathbf{N} = \cos\beta\mathbf{e}_1 + \sin\beta\mathbf{e}_2$ directions with $\alpha = \pi/6$ and $\beta = -\pi/3$, are subjected to uniaxial extensions in the loading direction $\mathbf{e}_1$. The results respective to both sates of the deformations demonstrate that the predicted responses of the model, so calibrated based on the introduced framework of the material characterization, are in good qualitative agreement with the experimentally observed mechanical behavior of the composites with different material anisotropy.

Note that, the experimental data in Fig. 2 are used for calibration of the mechanical interaction contribution Ψ_τ regardless of the fiber potential Ψ_F through the proposed structurally based framework of the material characterization. The same data are used also for verification of the model against symmetric deformations. These two are different treatments in that the latter is conducted considering both the fibers and the mechanical interaction contributions while the former is done independently of the potential of the fibers. Although the fibers are too stiff, however, they have a considerable contribution to the deformation. That is, both the calibration of the model and its verification through the finite element simulation are independent even though the same experimental data are used for them.

5. The importance of the mechanical interaction potential

There is no any notable declaration on the modifying aspects of including the mechanical interaction potential in overall behavior modeling of the composites until now with exception of a few papers as Guo et al. (2006) and Peng et al. (2013), which are limited to the fitting procedure. As stated, the MFI model along with its structurally based framework of material characterization enables us to obtain distinct contributions of the matrix, fibers, and mechanical interactions. This allows us to highlight the contributions of respective potentials, especially the importance of the mechanical interaction potential, in the modeling of fiber-reinforced elastomers. Toward this end, in the following three representative examples are evaluated: simple uniaxial extension of single layer composites with different material anisotropy, inflation-extension of a cylindrical tube, and load-coupling behaviors in composite laminates with various layups.

5.1. Uniaxial extension of single-layer composites

In the first example, the importance of the mechanical interaction potential Ψ_τ in behavior modeling of composite with different material anisotropy is shown by comparisons of the experimental results with finite element simulations. When the interaction potential is neglected the MFI constitutive model is reduced to the Holzapfel-Gasser-Ogden (HGO) model presented by Holzapfel et al. (2000). Fig. 4 compares

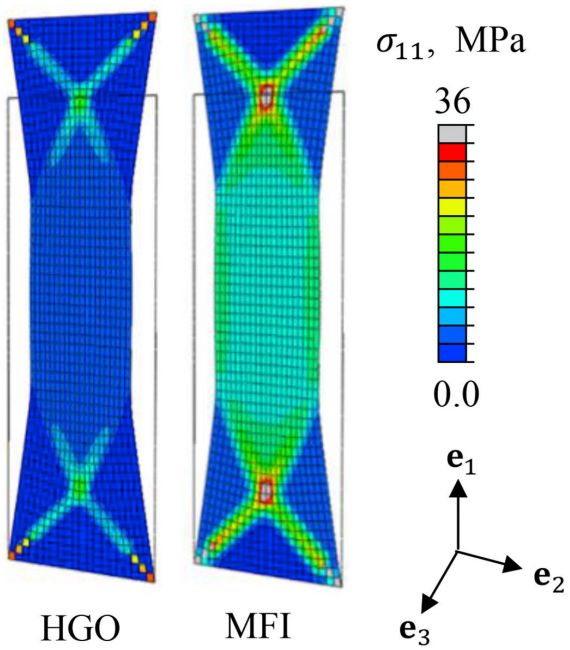

Fig. 4. Spatial distributions of the Cauchy stress σ_{11} using HGO and MFI models for a single layer fiber-reinforced elastomers with two fiber families as $\boldsymbol{M} = \cos\alpha\,\boldsymbol{e}_1 + \sin\alpha\,\boldsymbol{e}_2$ and $\boldsymbol{N} = \cos\beta\,\boldsymbol{e}_1 + \sin\beta\,\boldsymbol{e}_2$ with material anisotropy $\alpha = -\beta = \pi/4$ subjected to a uniaxial stretch of $\lambda_1 = 1.26$ in the $\boldsymbol{e}_1$ direction. The material properties provided in Table 1 are used for simulations

the finite element results of the MFI and HGO models for composites with material anisotropy $\alpha = -\beta = \pi/4$ subjected to the uniaxial extension tests. As it is evident, since the HGO model ignores the mechanical interaction contribution, it underestimates significantly the overall mechanical responses of the composites while the MFI constitutive model predicts the test results accurately. This issue is general and can be extended to all models in which the very important contribution of the mechanical interaction is ignored. In order to show graphically the effect of Ψ_τ for modeling of the latter symmetric deformation, the Cauchy stress distribution σ_{11} corresponding to a stretch of $\lambda_1 = 1.16$ is illustrated in Fig. 4. The geometry and boundary conditions used for simulation is exactly similar to that is used initially by the experiment. The results show a significant difference in the spatial stress distributions made by the incorporation of the interaction potential.

It should be mentioned that the HGO model is originally proposed for modeling the constitutive behavior of biological tissues. However, it is widely used by researchers to model fiber-reinforced inorganic materials, even more so now that it has been implemented in several finite element programs. Accordingly, in this work, the most cited constitutive model of fiber-reinforced elastomers, namely the HGO model, is used for comparative reasons. However, in this work, since the fibers are stiff (recall the material properties of the fibers provided in Table 1, where $k_1 \gg 0$ and $k_2 \approx 0$) an alternative quadratic function with respect to the invariants I_4 and I_6, rather than an exponential function as HGO, can also describe the mechanical behavior of the fibers, i.e.

$$\Psi_F = \frac{k_1}{2}\sum_{i=4,6}(I_i - 1)^2 \tag{18}$$

In the case of non-symmetric deformation states, Fig. 3 compares the finite element results of the MFI and HGO models for composites with material anisotropy $\alpha = \pi/6, \beta = -\pi/3$ subjected to uniaxial extension

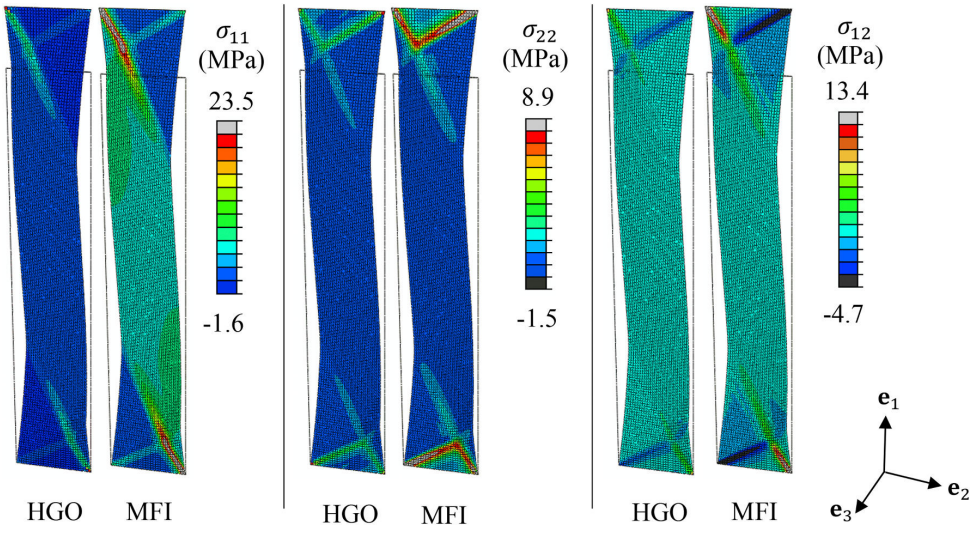

Fig. 5. Finite element simulation of uniaxial extension of a composite with two fiber families as $\boldsymbol{M} = \cos\alpha\,\boldsymbol{e}_1 + \sin\alpha\,\boldsymbol{e}_2$ and $\boldsymbol{N} = \cos\beta\,\boldsymbol{e}_1 + \sin\beta\,\boldsymbol{e}_2$, $\alpha = \pi/6$ and $\beta = -\pi/3$, subjected to a stretch of $\lambda_1 = 1.20$ in the loading direction $\boldsymbol{e}_1$. The effects of the interaction potential Ψ_τ are illustrated by the comparison of the stress distributions obtained from simulation results using the MFI and HGO models, whereas the latter neglects interaction contributions. The material properties provided in Table 1 are used for simulations

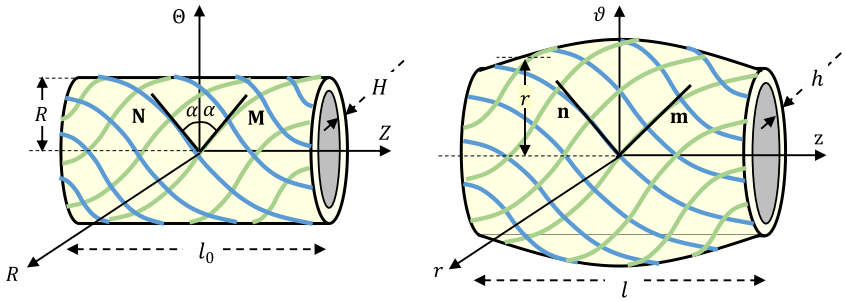

Fig. 6. Section of a long thin-walled cylindrical tube with two fiber families at un-deformed, left, and pressurized configurations, right.

tests explained earlier. As it is evident, again, the HGO model underestimates substantially the mechanical response of the composite while the MFI constitutive model predicts the test results accurately. For further illustrations, respective spatial distributions of the stress components σ_{11}, σ_{12}, and σ_{22} are depicted in Fig. 5 using MFI and HGO models. The same boundary conditions as in the experiment are used for all simulations so that all the nodes of the bottom face of the geometry are constrained and let the top face to be extended freely only in the loading direction $\mathbf{e}_1$ with a stretch of $\lambda_1 = 1.20$ at the top face. The results signify considerable effects of the interaction potential in mechanical behavior modeling of non-symmetric deformation states.

5.2. Inflation-extension of a cylindrical tube

To further illustrate the influence of the mechanical interaction potential in the overall constitutive behavior of fiber-reinforced elastomers, we now consider a complicated deformation as for example inflation-extension of a thin-walled cylindrical tube with closed ends. The cylindrical tubes are popular structures in finite elasticity and are used frequently for evaluation of the mechanical behavior of soft materials under pressure loads (Horný et al., 2015; Masson et al., 2010; Topol et al., 2019; Zidi and Cheref, 2002). The cylindrical tube chosen in this work is subjected to internal pressure P and uniform axial force (due to the internal pressure) at the closed ends of the tube. The two fiber families are initially disposed symmetrically about the circumferential axis Θ with unit vectors $\mathbf{M} = \cos\alpha\,\mathbf{E}_\Theta + \sin\alpha\,\mathbf{E}_Z$ and $\mathbf{N} = \cos\alpha\,\mathbf{E}_\Theta - \sin\alpha\,\mathbf{E}_Z$, $\alpha > 0$, that causes the tube to deform uniformly without twisting, shown in Fig. 6. This figure illustrates a section of a long cylindrical tube with a material point initially located at a Cylindrical basis vector $\{R,\ \Theta,\ Z\}$. During the deformation, this point is mapped into $\{r, \vartheta,\ z\}$ by a motion with the deformation gradient $\mathbf{F} = \mathrm{diag}[\lambda_r, \lambda_\vartheta, \lambda_z]$, i.e.

$$r = \lambda_\vartheta R, \quad h = \lambda_r H, \quad z = \lambda_z Z, \quad \vartheta = \Theta \tag{19}$$

where λ_z, λ_ϑ and λ_r are principal stretches in axial, circumferential, and radial directions. Here, r and h respectively denote middle radius and thickness with regard to deformed configuration, and H is the initial thickness of the tube. The invariants of the deformation are given by $I_1 = \lambda_r^2 + \lambda_\vartheta^2 + \lambda_z^2$, $I_2 = \lambda_r^{-2} + \lambda_\vartheta^{-2} + \lambda_z^{-2}$, $I_4 = I_6 = \lambda_\vartheta^2\cos^2\alpha + \lambda_z^2\sin^2\alpha$ and $I_8 = \lambda_\vartheta^2\cos^2\alpha - \lambda_z^2\sin^2\alpha$. For a thin-walled tube, the Cauchy stress in the thickness direction can be considered zero, i.e. $\sigma_{rr} = 0$. Hence, from (10) one obtains the value of the Lagrange multiplier as $p = 2\lambda_r^2\partial\Psi/\partial I_1$. The circumferential and axial components of the Cauchy stress can be found

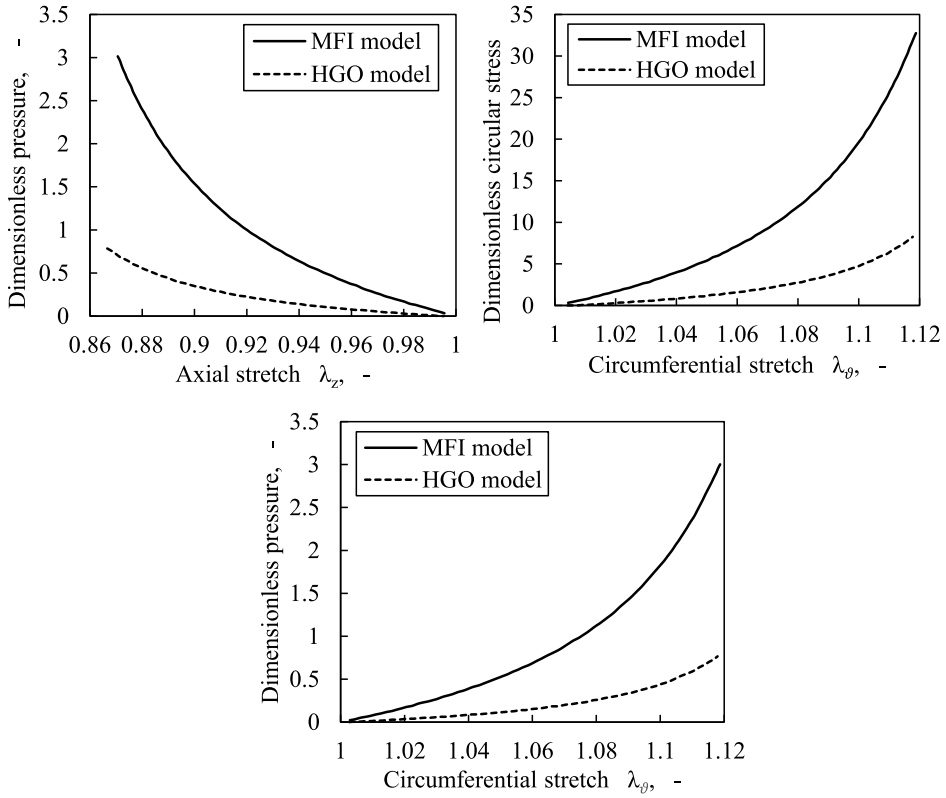

Fig. 7. Inflation-extension responses of a thin-walled cylindrical tube ($\alpha = \pi/4$) using the MFI and HGO models. The weight of the mechanical interaction potential Ψ_τ is featured showing its effects when neglected by comparison of constitutive responses of MFI and HGO models for different quantities. The material properties provided in Table 1 are used for simulations.

by applying equilibrium states of a pressurized tube with internal pressure P as

$$\sigma_{\vartheta\vartheta} = \frac{Pr}{h}, \quad \sigma_{zz} = \frac{Pr}{2h} \quad \text{or} \quad \sigma_{\vartheta\vartheta} - 2\sigma_{zz} = 0 \tag{20}$$

Substituting kinematics (19) in (20) gives

$$\sigma_{\vartheta\vartheta} = \frac{P_d}{\varepsilon}\lambda_\vartheta^2\lambda_z, \quad \sigma_{zz} = \frac{P_d}{2\varepsilon}\lambda_\vartheta^2\lambda_z \tag{21}$$

with the dimensionless denotations $\varepsilon = H/R$ and $P_d = P/\ c_{10}$. The circumferential and axial components of the Cauchy stress can be also found from the constitutive equation (10), respectively, as

$$\sigma_{\vartheta\vartheta} = -p + 2c_{10}\lambda_\vartheta^2 + 4\frac{\partial\Psi_F}{\partial I_4}\lambda_\vartheta^2\cos^2\alpha + \frac{2}{I_4}\frac{\partial\Psi_\tau}{\partial I_8^*}\left(1 - I_8^*\right)\lambda_\vartheta^2\cos^2\alpha \tag{22}$$

$$\sigma_{zz} = -p + 2c_{10}\lambda_z^2 + 4\frac{\partial\Psi_F}{\partial I_4}\lambda_z^2\sin^2\alpha - \frac{2}{I_4}\frac{\partial\Psi_\tau}{\partial I_8^*}\left(1 + I_8^*\right)\lambda_z^2\sin^2\alpha \tag{23}$$

Note that herein, the deformation is homogeneous and hence the shear components of the stress are zero. From the incompressibility condition, one obtains $\lambda_r = \lambda_\vartheta^{-1}\lambda_z^{-1}$. Substituting the values of p and λ_r in (22) and (23) gives $\sigma_{\vartheta\vartheta}$ and σ_{zz} as functions of both circumferential and axial stretches. To find numerically a relation between the stretches λ_ϑ and λ_z the equilibrium function defined in Eq. $(20)_2$ is solved by minimizing the objective function of $\langle\sigma_{\vartheta\vartheta} - 2\sigma_{zz}\rangle^2$. It is done for unknown λ_z with prescribed values of λ_ϑ. Next, combining equations (21)–(23), one obtains relations that govern inflation load (P_d) to circumferential and axial directions (λ_ϑ, λ_z). Inflation-extension behavior of the thin-walled cylindrical tube considering the MFI and HGO constitutive models is plotted in Fig. 7 using the material properties provided in Table 1 and considering $\varepsilon = 0.1$. In view of these results, one can claim the substantial weight of the mechanical interaction potential for behavior modeling of the pressurized thin-walled cylindrical tubes.

5.3. Load-coupling behaviors

The primary purpose of the mechanical characterization of the single-layer composites is designing composite laminates aiming at pronounced functionalities. Load coupling effects, e.g. extension-twist coupling, are among interesting functionalities offering a huge potential for completely new application concepts such as the field of elastofluidics (Bishop-Moser, 2014; Felt et al., 2017; Felt and Remy, 2018). In this section, the importance of mechanical interaction potential is evaluated for modeling the load-coupling behaviors in fiber-reinforced composite laminates. To do this, a composite laminate with two layers and material anisotropy as [+ 45 − 45/+ 30 − 60] is subjected to a uniaxial displacement of $d = 5$ mm in the loading direction $\mathbf{e}_1$ applied on the front face as shown in Fig. 8. The material anisotropy of each layer is disposed about the direction $\mathbf{e}_1$. Each layer has the same model geometry with the dimension of 100 × 50 × 2 (mm ×mm ×mm) aligned with the axes $\mathbf{e}_1$, $\mathbf{e}_2$, and $\mathbf{e}_3$. All nodes of the front and back face of the geometry are fixed with the exception that the nodes of the front face are allowed to elongate and rotate along and about $\mathbf{e}_1$, respectively. During the extension of the composite, load coupling effects in the form of

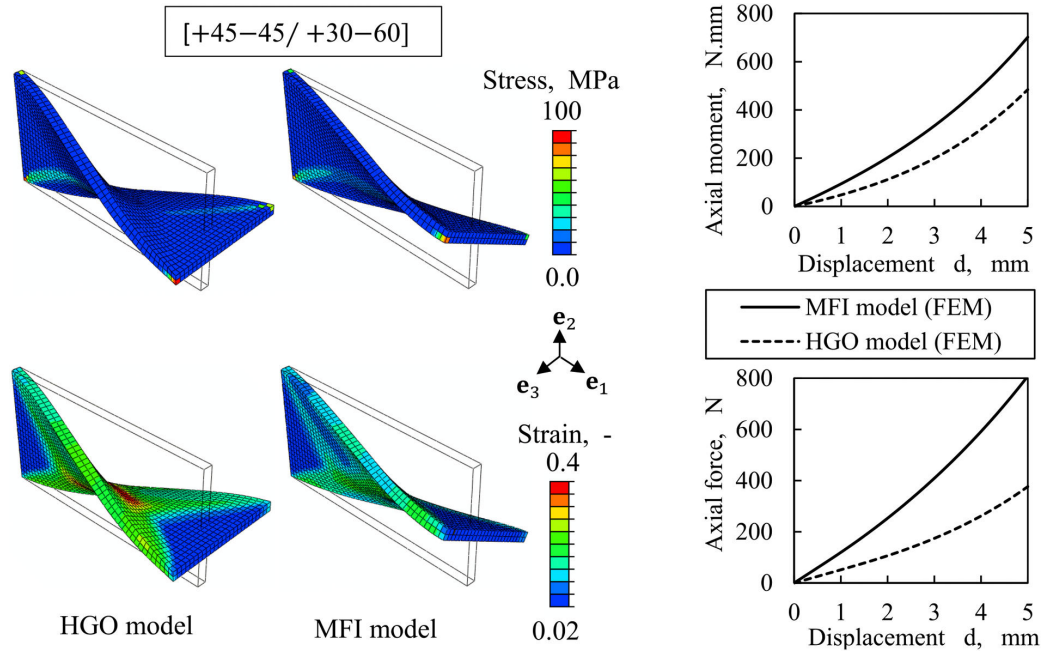

Fig. 8. The effect of the mechanical interaction potential in load-coupling behavior modeling of a composite laminate using the MFI and HGO constitutive models for a displacement of $d = 5$ mm in the loading direction $\boldsymbol{e}_1$. Moment-displacement and force-displacement responses are also compared.

extension-twist deformations are observed in Fig. 8. In this figure, the load-coupling behaviors are modeled using the MFI and HGO constitutive models and the corresponding spatial distributions of the stresses and strains are shown there. The results indicate that not only significant differences are observed in the stresses and strains distributions but also the mechanical interaction contribution highly affects the amount of twisting, which results in different final configurations. For a quantitative evaluation of the interaction potential, the force-displacement and moment-displacement responses of the same laminate are provided in this figure.

6. Conclusions

A unified invariant-base constitutive model for hyperelastic fiber-reinforced elastomers with two fiber families considering the contributions of the matrix, fiber, and particularly the mechanical interactions, so-called the MFI model, is proposed. An extensional-base invariant set is used by the fibers' potential and an angular-base invariant is employed by an exponential-polynomial function to form the mechanical interaction potential. In an effort to find the mechanical interaction properties regardless of the fibers potential, a workless reaction term consistent with the kinematics of the mechanical interactions is added to the mechanical interaction potential. The above-mentioned adoptions introduce a structurally based framework for material characterization of such composites. The following features can be stated for the MFI model characterized within the introduced framework of material characterization:

- Experimental advantage. The anisotropy can be characterized completely with the least number of required tests using simple uniaxial extension tests rather than complicated ones such as biaxial deformations.
- Accuracy. The proposed model enables us to capture the mechanical behavior of fiber-reinforced elastomers with two fiber families and with different material anisotropy (see the previous section). It is shown by the comparison of experiments with finite element simulations for symmetric and non-symmetric deformation states.
- Utility. The mechanical interaction properties are obtained within the introduced framework by fitting the Cauchy stress (17) to the stress-stretch response of the symmetric deformations featured in Section 4.

In order to show the importance of the mechanical interactions in constitutive modeling of fiber-reinforced elastomers, three representative examples are provided: uniaxial extension of single-layer composites with different material anisotropy, inflation-extension of a thin-walled cylindrical tube, and extension-twist coupling behaviors in composite laminates subjected to uniaxial extensions are all modeled using the MFI and HGO constitutive models. The results imply that the mechanical interaction potential affects substantially the constitutive behavior of the fiber-reinforced elastomers. This work contributes to the importance of the mechanical interaction for modeling of inorganic materials, yet remains to wait for biomaterials, particularly since recently Holzapfel and Ogden (2019) proposed a model accounting for coupling between the collagen fiber and cross-link directions in arterial walls.

CRediT authorship contribution statement

M.R. Mansouri: Conceptualization, Software, Investigation, Formal analysis, Writing - original draft. **P.F. Fuchs:** Funding acquisition, Supervision, Writing - review & editing. **J.C. Criscione:** Writing - review & editing. **B. Schrittesser:** Supervision, Writing - review & editing. **J. Beter:** Investigation.

Declaration of competing interest

The authors declare that they have no known competing financial

interests or personal relationships that could have appeared to influence the work reported in this paper.

Acknowledgement

The research work was performed at the Polymer Competence Center Leoben GmbH (PCCL, Austria) within the framework of the COMET-program of the Federal Ministry of Science, Research and Economy with contributions by Montanuniversitaet Leoben (Chair of Materials Science and Testing of Polymers, Austria).

Appendix A

The free energy of fiber-reinforced elastomers must be unchanged if a deformed configuration by $\mathbf{f}$ occupying a region as $\overline{\mathbf{\Omega}}$ undergoes a rotation described by the proper orthogonal tensor $\mathbf{Q}$ such that $\mathbf{Q}^{\mathrm{T}}\mathbf{Q} = \mathbf{I}$ and $\det\mathbf{Q} = 1$. The deformed region $\overline{\mathbf{\Omega}}$ relative to the deformation gradient $\mathbf{f}$ is rotated to the final configuration B, i.e.

$$\mathbf{F} = \mathbf{Q}\,\mathbf{f} \tag{A.1}$$

Since $\mathbf{C} = \mathbf{F}^{\mathrm{T}}\mathbf{F} = \mathbf{f}^{\mathrm{T}}\mathbf{f} = \mathbf{U}^2$, the deformation gradients $\mathbf{F}$ and $\mathbf{f}$ share the same Lagrangian strain.

Criscione and Hunter (2003) proposed three strain attributes in the basis of three scalars $\{\alpha_c,\ \mathscr{B},\ \gamma\}$ for *thin incompressible* fiber-reinforced elastomers with two fiber families (For a detailed discussion, the authors are referred to the referenced paper). The scalar α_c is area ratio of the fiber plane $(\mathbf{E}_1 - \mathbf{E}_2)$ due to distortion keeping the fibers angle without change, $\mathscr{B}$ represents the change of the angle between fibers of the same stretch, and γ is a shear strain in the fiber plane that differentially changes the length of deformed elements yet does not perturb the angle. They introduced the following relations between the strain attributes and invariants of the deformation described earlier as

$$\sqrt{I_4 I_6} = \alpha_c\left(\mathscr{B}^2 c^2 + \mathscr{B}^{-2} s^2\right) \tag{A.2}$$

$$\frac{\sqrt{I_4}}{\sqrt{I_6}} = \frac{\sqrt{1+\gamma^2 s^2 c^2} - \gamma sc}{\sqrt{1+\gamma^2 s^2 c^2} + \gamma sc} \tag{A.3}$$

wherein $c = \cos\theta$ and $s = \sin\theta$. They factored $\mathbf{f}$ into modes of deformation corresponding to the three scalar strain attributes as follows:

$$\mathbf{f} = \mathbf{f}_{\alpha_c}\mathbf{f}_{\mathscr{B}}\mathbf{f}_{\gamma} \tag{A.4}$$

Upon setting the kinematics constraint I (recall Eq. (4)), i.e. $I_4 = I_6 = 1$, in Eqs. (A.2) and (A.3), and considering the relation $(3)_2$, it is straightforward to show, respectively, that

$$\alpha_c = \left(\mathscr{B}^2 c^2 + \mathscr{B}^{-2} s^2\right)^{-1},\ \gamma = 0,\ \mathscr{B} = g(\phi) \tag{A.5}$$

where g shows a functional dependency of β to the current angle ϕ. The three relations in (A.5) show that, under constraint I, all the deformation scalars $\{\alpha_c,\ \mathscr{B},\ \gamma\}$ are reduced to $\{\mathscr{B}\}$ and therefore, from $\mathscr{B} = g(\phi)$, depend on ϕ. Now upon replacing the scalars of (A.5) in (A.4) it is found that the components of $\mathbf{f}$ can be given in terms of ϕ, i.e. $\mathbf{f} = \mathbf{f}^*_{\phi}$. Accordingly, under constraint I, the *entire* deformation field given by (A.1) is then defined specifically in terms of the change of the angle between fibers through $\mathbf{f}^*_{\phi}$ super-imposed by a rigid-body motion, $\mathbf{Q}$, i.e.

$$\mathbf{F}_I = \mathbf{Q}\,\mathbf{f}^*_{\phi} \tag{A.6}$$

The second kinematic constraint defined in Eq. (4) represents the case where the current angle between fibers, ϕ, is held constant while the elongation of the fibers is allowed. Hence, replacing the constraint $\phi = 2\theta$ in $(3)_2$ yields

$$\cos 2\,\theta = \frac{1-\tan^2\theta}{1+\tan^2\theta} = \frac{\mathscr{B}^2\cos^2\theta - \mathscr{B}^{-2}\sin^2\theta}{\mathscr{B}^2\cos^2\theta + \mathscr{B}^{-2}\sin^2\theta} \tag{A.7}$$

Upon doing some algebra on the right-hand side of the equation, it is found that $\mathscr{B} = 1$. With substitution into (A.2) and considering the equation (A.3), the three scalars can be written as

$$\alpha_c = \sqrt{I_4 I_6}\ ,\qquad \mathscr{B} = 1,\qquad \gamma = h(I_4, I_6) \tag{A.8}$$

where $\gamma = h(I_4, I_6)$ shows functional dependency of γ to the extensional-base invariants I_4 and I_6. Bearing in mind that γ differentially changes the length of deformed elements yet does not perturb the angle and replacing the scalars defined in (A.8) into relation (A.4) it yields $\mathbf{f} = \mathbf{f}^*_{\mathrm{f}}$, where the components of $\mathbf{f}^*_{\mathrm{f}}$ have a functional dependency on the extensional-base invariants I_4 and I_6. For this case, the deformation gradient (A.1) is therefore defined as

$$\mathbf{F}_{II} = \mathbf{Q}\,\mathbf{f}^*_{\mathrm{f}} \tag{A.9}$$

References

Alhayani, A.A., Rodríguez, J., Merodio, J., 2014. Competition between radial expansion and axial propagation in bulging of inflated cylinders with application to aneurysms propagation in arterial wall tissue. Int. J. Eng. Sci. 85, 74–89.

Bishop-Moser, J.L., 2014. Design of Generalized Fiber-Reinforced Elasto-Fluidic Systems.

Chaimoon, K., Chindaprasirt, P., 2019. An anisotropic hyperelastic model with an application to soft tissues. Eur. J. Mech. Solid. 78, 103845.

Chebbi, E., Wali, M., Dammak, F., 2016. An anisotropic hyperelastic constitutive model for short glass fiber-reinforced polyamide. Int. J. Eng. Sci. 106, 262–272.

Connolly, F., Wagner, D.A., Walsh, C.J., Bertoldi, K., 2019. Sew-free anisotropic textile composites for rapid design and manufacturing of soft wearable robots. Extreme Mechan. Lett. 27, 52–58.

Criscione, J.C., Hunter, W.C., 2003. Kinematics and elasticity framework for materials with two fiber families. Continuum Mech. Therm. 15 (6), 613–628.

Felt, W., Remy, C.D., 2018. A closed-form kinematic model for fiber-reinforced elastomeric enclosures. J. Mech. Robot. 10 (1), 14501.

Felt, W., Telleria, M.J., Allen, T.F., Hein, G., Pompa, J.B., Albert, K., Remy, C.D., 2017. An inductance-based sensing system for bellows-driven continuum joints in soft robots. Aut. Robots 1–14.

Fereidoonnezhad, B., Naghdabadi, R., Arghavani, J., 2013. A hyperelastic constitutive model for fiber-reinforced rubber-like materials. Int. J. Eng. Sci. 71, 36–44.

Gong, Y., Peng, X., Yao, Y., Guo, Z., 2016. An anisotropic hyperelastic constitutive model for thermoplastic woven composite prepregs. Compos. Sci. Technol. 128, 17–24.

Gong, Y., Yan, D., Yao, Y., Wei, R., Hu, H., Xu, P., Peng, X., 2017. An anisotropic hyperelastic constitutive model with tension–shear coupling for woven composite reinforcements. Int. J. Appl. Mech. 9 (6), 1750083.

Guo, Z.Y., Peng, X.Q., Moran, B., 2006. A composites-based hyperelastic constitutive model for soft tissue with application to the human annulus fibrosus. J. Mech. Phys. Solid. 54 (9), 1952–1971.

Holzapfel, G.A., Gasser, T.C., 2001. A viscoelastic model for fiber-reinforced composites at finite strains: continuum basis, computational aspects and applications. Comput. Methods Appl. Mech. Eng. 190 (34), 4379–4403.

Holzapfel, G.A., Gasser, T.C., Ogden, R.W., 2000. A new constitutive framework for arterial wall mechanics and a comparative study of material models. J. Elasticity Phys. Sci. solids 61 (1), 1–48. https://doi.org/10.1023/A:1010835316564.

Holzapfel, G.A., Ogden, R.W., 2009. Constitutive modelling of passive myocardium: a structurally based framework for material characterization. Phil. Trans. Roy. Soc. Lond.: Math. Phys. Eng. Sci. 367 (1902), 3445–3475.

Holzapfel, G.A., Ogden, R.W., 2019. An arterial constitutive model accounting for collagen content and cross-linking. J. Mech. Phys. Solid. 103682.

Horný, L., Netušil, M., Horák, Z., 2015. Limit point instability in pressurization of anisotropic finitely extensible hyperelastic thin-walled tube. Int. J. Non Lin. Mech. 77, 107–114.

Liu, H., Holzapfel, G.A., Skallerud, B.H., Prot, V., 2019. Anisotropic finite strain viscoelasticity: constitutive modeling and finite element implementation. J. Mech. Phys. Solid. 124, 172–188.

Mansouri, M.R., Darijani, H., 2014. Constitutive modeling of isotropic hyperelastic materials in an exponential framework using a self-contained approach. Int. J. Solid Struct. 51 (25), 4316–4326. https://doi.org/10.1016/j.ijsolstr.2014.08.018.

Mansouri, M.R., Darijani, H., Baghani, M., 2017. On the correlation of FEM and experiments for hyperelastic elastomers. Exp. Mech. 57 (2), 195–206. https://doi.org/10.1007/s11340-016-0236-0.

Masson, I., Fassot, C., Zidi, M., 2010. Finite dynamic deformations of a hyperelastic, anisotropic, incompressible and prestressed tube. Applications to in vivo arteries. Eur. J. Mech. Solid. 29 (4), 523–529.

Melnik, A.V., Luo, X., Ogden, R.W., 2018. A generalised structure tensor model for the mixed invariant I8. Int. J. Non Lin. Mech. https://doi.org/10.1016/j.ijnonlinmec.2018.08.018.

Merodio, J., Saccomandi, G., 2006. Remarks on cavity formation in fiber-reinforced incompressible non-linearly elastic solids. Comput. Mater. Sci. 25 (5), 778–792.

Milani, A.S., Nemes, J.A., 2004. An intelligent inverse method for characterization of textile reinforced thermoplastic composites using a hyperelastic constitutive model. Compos. Sci. Technol. 64 (10–11), 1565–1576.

Murphy, J.G., 2013. Transversely isotropic biological, soft tissue must be modelled using both anisotropic invariants. Eur. J. Mech. Solid. 42, 90–96.

Peng, X., Guo, G., Zhao, N., 2013. An anisotropic hyperelastic constitutive model with shear interaction for cord–rubber composites. Compos. Sci. Technol. 78, 69–74.

Peng, X.Q., Guo, Z.Y., Moran, B., 2006. An anisotropic hyperelastic constitutive model with fiber-matrix shear interaction for the human annulus fibrosus. J. Appl. Mech. 73 (5), 815–824.

Ren, J.-s., Zhou, J.-w., Yuan, X., 2011. Instability analysis in pressurized three-layered fiber-reinforced anisotropic rubber tubes in torsion. Int. J. Eng. Sci. 49 (4), 342–353.

Spencer, A.J.M., 1984. Constitutive theory for strongly anisotropic solids. In: Continuum Theory of the Mechanics of Fibre-Reinforced Composites. Springer, pp. 1–32.

Topol, H., Demirkoparan, H., Pence, T.J., 2019. Morphoelastic fiber remodeling in pressurized thick-walled cylinders with application to soft tissue collagenous tubes. Eur. J. Mech. Solid. 77, 103800.

Treloar, L.R.G., 1943. The elasticity of a network of long-chain molecules. I. Trans. Faraday Soc. 39, 36–41.

Tricerri, P., Dedè, L., Gambaruto, A., Quarteroni, A., Sequeira, A., 2016. A numerical study of isotropic and anisotropic constitutive models with relevance to healthy and unhealthy cerebral arterial tissues. Int. J. Eng. Sci. 101, 126–155.

Wagner, D.R., Lotz, J.C., 2004. Theoretical model and experimental results for the nonlinear elastic behavior of human annulus fibrosus. J. Orthop. Res. 22 (4), 901–909.

Zidi, M., Cheref, M., 2002. Finite deformations of a hyperelastic, compressible and fibre reinforced tube. Eur. J. Mech. Solid. 21 (6), 971–980.

International Journal of Mechanical Sciences 195 (2021) 106268

Contents lists available at ScienceDirect

International Journal of Mechanical Sciences

journal homepage: www.elsevier.com/locate/ijmecsci

Quantifying matrix-fiber mechanical interactions in hyperelastic materials

M.R. Mansouri [a,*], J. Beter [a], P.F. Fuchs [a], B. Schrittesser [a], G. Pinter [b]

[a] Polymer Competence Center Leoben GmbH, Leoben, Austria
[b] Department Polymer Engineering and Science, Montanuniversitaet Leoben, Leoben, Austria

ARTICLE INFO

Keywords:
Matrix-fiber interaction
In situ test
Finite element analysis

ABSTRACT

Hyperelastic fiber-reinforced materials are commonly characterized and modeled in terms of the contributions of the constituent materials, while their matrix-fiber mechanical interactions have been received little attention. This work is an initial attempt to quantify the matrix-fiber mechanical interactions using a combined experimental, analytical, and simulation study. For the experiments, the local stretch maps are captured via digital image correlation during tensile tests on polydimethylsiloxane-glass fiber (PDMS-GF) and polyurethane-glass fiber (PUR-GF) composites with different aspect ratios and various material anisotropy. Moreover, *in situ* optical measurements during mechanical loadings are carried out on transparent PDMS-GF composites to monitor the change of angle between deformed fibers, as the origin of the matrix-fiber interactions. The stress-stretch responses of all composite materials are then presented, showing different behaviors based on the sample aspect ratios for a specific material anisotropy. The analytical study is carried out within a constitutive framework by adapting a matrix-fiber-interaction model proposed for the modeling of mechanical interactions. The constitutive framework, including an angular-base invariant, a specific deformation gradient, and the stress-stretch behavior of the model, is compared against the experimental results. An FE-implementation using user-defined subroutines is presented, which allows us to perform a combined experimental and simulation study of the matrix-fiber mechanical interactions. Finally, the underlying mechanism contributing to the mechanical behavior of hyperelastic fiber-reinforced materials is discussed via performing a couple of finite element analysis.

1. Introduction

A combination of soft elastomers with stiff fibers enables the build-up of a composite with more distinct direction-dependent properties [1,2] than the classical resin-based composite systems, which makes them an interesting option for load coupling applications. Hyperelastic fiber-reinforced materials are commonly characterized and modeled in terms of the contributions of the constituent materials, while their matrix-fiber mechanical interactions have been received little attention. The papers by, for example, [3–9] accounted the contributions of the matrix and fibers as constituent materials for modeling inorganic fiber-reinforced composites. Besides, the works by [10–14], are examples in which the contributions of the constituent materials are considered for mechanical behavior modeling of soft biological tissues. We make no attempt to list a large number of the works done in this subject.

The matrix-fiber interaction is introduced by [15] and [16] for modeling the mechanical behavior of human annulus fibrosus. Since then, it has been considered for modeling of a cord-rubber composite [17], biological tissues [18], soft inorganic composites [19,20], and dry fabrics [21]. However, the experimental characterization, the analytical analysis in a constitutive framework, and the finite element simulation of the matrix-fiber mechanical interactions have not yet been quantified satisfactorily in the literature, with exception of a few papers as [17,18,22], which are limited to the fitting procedure. Quantifying the mechanical interactions becomes more crucial especially if there exists a considerable difference between the stiffness of the constituent materials.

In this paper, the matrix-fiber mechanical interaction is experimentally studied for PDMS-GF and PUR-GF composites using digital image correlation to quantify the local stretch maps and *in situ* optical imaging at the length scale of the fibers to measure the angle change between deformed fibers, as a source of mechanical interactions. Moreover, the tensile stress-stretch responses of the composites with different aspect ratios and various material anisotropy are reported. The experimental results are analyzed analytically in a constitutive framework using a matrix-fiber-interaction model of fiber-reinforced materials. After finite element implementation of the model, for the reader interested in using it, the particular contributions of the material phases in the mechanical behavior of composites are quantified through performing a couple of finite element simulations.

* Corresponding author.
E-mail address: mohammad.mansouri@pccl.at (M.R. Mansouri).

https://doi.org/10.1016/j.ijmecsci.2021.106268
Received 12 October 2020; Received in revised form 9 December 2020; Accepted 1 January 2021
Available online 5 January 2021
0020-7403/

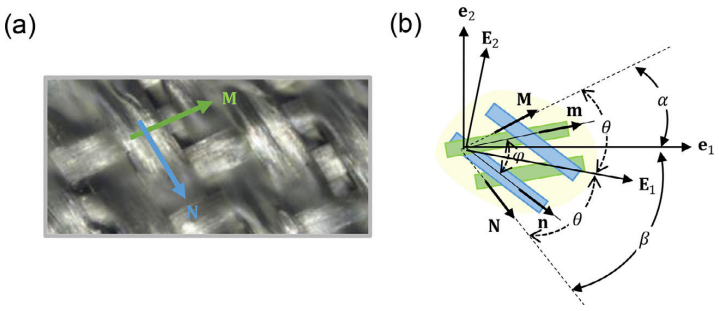

Fig. 1. Change of fiber angle during deformation: (a) micrographs of an undeformed region with two fiber families shown by the directions $\boldsymbol{M}$ and $\boldsymbol{N}$; (b) schematic illustrations of the fiber directions after deformation, shown by $\boldsymbol{m}$ and $\boldsymbol{n}$, where $\boldsymbol{E}_1$ in the orthogonal coordinate system $\{\boldsymbol{E}_1,\boldsymbol{E}_2\}$ is the bisector of fibers at undeformed state. A fixed coordinate system such as $\{\boldsymbol{e}_1,\boldsymbol{e}_2\}$ is applied for specifying the loading in the $\boldsymbol{e}_1$ direction.

Table 1
Test samples represented by the fiber orientations $[+\ \alpha\ -\ \beta]_n$, numbered by n, and the aspect ratio of $\xi = l/a$, where a and $\boldsymbol{l}$ denote width and length of the samples, respectively.

Sample $[+\ \alpha\ -\ \beta]_n$	a × l, mm × mm	$\xi = l/a$, -
[+0− 90]	30 × 90	3
$[+45- 45]_1$	40 × 80	2
$[+45- 45]_2$	30 × 90	3/tan α
$[+45- 45]_3$	35 × 105	3/tan α
$[+45- 45]_4$	40 × 120	3/tan α
$[+30- 60]_1$	30 × 90	3
$[+30- 60]_2$	35 × 105	3
$[+30- 60]_3$	40 × 120	3
$[+30- 60]_4$	30 × 156	3/tan α
$[+30- 60]_5$	40 × 208	3/tan α

2. Materials and methods

Fiber-reinforced composites with polydimethylsiloxane (PDMS) and polyurethane (PUR) as two matrix and endless, twill woven E-glass fibers (GF) as reinforcement are manufactured using the vacuum assisted resin infusion (VARI) method with a vacuum pressure of 20 mbar. The commercial E-glass fibers purchased from CS Interglas AG are considered with the classification EC9-69 × 5t0, an area weight of 220 g/m^2 and a mean fiber diameter of approximately 10 μm. The PDMS used here is an addition-curing two-component system with a hardness of 35 Shore A, a density of 1.02 g/cm^3 and a viscosity in uncured state of 3500 mPas and pot life of about 90 min at room temperature while the polyurethane reveals a hardness of 50 Shore A with a density of 1.04 g/cm^3 and a viscosity of 250 mPas with a corresponding pot lifetime of about 25 min at room temperature. The elastomeric matrix materials are mixed and cured with the mixing ratio recommended by the suppliers and a curing time of 60 min at 70°C in an oven.

In this work, the manufactured composites contain two fiber families in the form of woven fabrics (see Fig. 1(a)) that are initially aligned in the $\mathbf{M} = \cos\alpha\,\mathbf{e}_1 + \sin\alpha\mathbf{e}_2$ and $\mathbf{N} = \cos\beta\mathbf{e}_1 + \sin\beta\mathbf{e}_2$ directions, $\alpha > 0$ and $\beta < 0$, where a fixed coordinate system such as $\{\mathbf{e}_1,\mathbf{e}_2,\mathbf{e}_3\}$ is applied for specifying the loading in the $\mathbf{e}_1$ direction. Samples with a preferred fiber orientation represented by $[+\ \alpha\ -\ \beta]$, such as [+0− 90], [+45− 45], and [+30− 60] are prepared to have a thickness of approximately 0.4 mm. For the preparation of the two latter composites, various sample geometries defined by an aspect ratio of $\xi = l/a$ are considered, where a is the width and l denotes the length of samples between the clamps, respectively. All the PDMS-GF and PUR-GF composites are numbered by n, i.e. $[+\ \alpha\ -\ \beta]_n$, presented in Table 1. Since characterizing the composites with the fiber orientation [+0− 90] is not critical, only one setting with the specifications shown in Table 1 is considered for that. Tensile tests are performed on all samples and the average stress-stretch response of three samples cut through from the same sheet is reported for each setting (60 composite samples with 20 settings). Tests are carried out by the universal testing machine Z250 (Zwick Roell GmbH & Co. KG) at a quasi-static rate of 10 mm/min. To map the local stretches for all samples, 3D full-field, high-resolution images are captured via a digital image correlation system (Aramis 4M, GOM GmbH, Braunschweig, Germany).

In situ microscale tests are performed to monitor the current angle between deformed fibers during loading experiments. The PDMS-GF samples with fiber oreintation [+45− 45] are placed in a custom-designed *in situ* tensile test device, while they are under an optical microscope (Alicona InfiniteFocusG5 Plus, Austria) with objective magnification of 100x. Moreover, the distortion of the fibers at their intersections are captured during stretching the composites, which is indicative of the fiber-fiber interactions. Both the change of fiber angle and the fiber-fiber interactions contribute to the mechanical interaction potential. The term 'matrix-fiber mechanical interaction' is concisely referred to herein as both matrix-fiber and fiber-fiber mechanical interactions.

3. Constitutive framework

A matrix-fiber-interaction constitutive model is adopted here, by which the individual contributions of the matrix, the fibers, and the mechanical interactions can be obtained distinctly, see [19]. The model introduces a constitutive framework, based on which the contribution of the mechanical interaction potential can be determined independently of the fibers' potential. The constitutive framework, including an angular-base invariant, a specialized deformation gradient, and stress-stretch constitutive relations, is explained in this section.

3.1. A matrix-fiber-interaction model

A unified, invariant-based model for hyperelastic fiber-reinforced elastomers with two fiber families proposed in [19] is described here. The model is decomposed into three contributions: matrix, fiber, and (mechanical) interactions and is named the MFI model [19]. The general form of the MFI strain-energy density function is defined as

$$\Psi(\mathbf{C},\ \{\mathbf{M},\mathbf{N}\}) = \Psi_{\mathrm{M}}(I_1) + \Psi_{\mathrm{F}}(I_4,\ I_6) + \Psi_{\tau}(I_8^*) - \frac{1}{2}q(I_4-1) - \frac{1}{2}r(I_6-1)$$

$$\begin{cases} \text{I. inextensible fibers} & I_4,\ I_6 = 1 \\ \text{II. extensible fibers} & q,\ r = 0 \end{cases} \tag{1}$$

where the subscripts M, F, and τ denote matrix, fiber, and mechanical interaction contributions, respectively. In the equation above, $I_1 = \mathrm{tr}\,\mathbf{C}$, where $\mathbf{C} = \mathbf{F}^{\mathrm{T}}\mathbf{F}$ is the right Cauchy-Green strain tensor, and $\mathbf{F}$ is the deformation gradient. The extensional-based invariants with definitions $I_4(\mathbf{M}) = \mathbf{C}\colon \mathbf{M}\otimes\mathbf{M}$ and $I_6(\mathbf{N}) = \mathbf{C}\colon \mathbf{N}\otimes\mathbf{N}$ are employed by the fiber potential Ψ_{F}, where $\mathbf{M} = \cos\theta\mathbf{E}_1 + \sin\theta\mathbf{E}_2$ and $\mathbf{N} = \cos\theta\mathbf{E}_1 - \sin\theta\mathbf{E}_2$ are defined as preferred fiber directions in the undeformed configuration. According to [23], the two invariants I_4 and I_6 have a clear kinematical interpretation since they define the square of the stretch in the directions $\mathbf{M}$ and $\mathbf{N}$, respectively. It is assumed that two fiber families do not

contribute to the deformation when they are compressed. Hence, the potentials reconstructed by them are assumed to be zero when $I_4 < 1$ and $I_6 < 1$. This assumption is due to the fact that the soft nature of the matrix makes it rather impossible for the *thin* composite to bear in-plane compressible loads. The angle θ is half of the angle subtended by **M** and **N** in the undeformed configuration. A relation for the cosine of the current angle between deformed fibers is presented in [24] as the left-hand side of the following equation [19]

$$\cos\varphi = \frac{\mathbf{C} : \mathbf{M}\otimes\mathbf{N}}{\sqrt{\mathbf{C} : \mathbf{M}\otimes\mathbf{M}}\,\sqrt{\mathbf{C} : \mathbf{N}\otimes\mathbf{N}}} = \frac{I_8}{\sqrt{I_4\, I_6}} = I_8^* \tag{2}$$

Replacing the invariants I_4, I_6 (defined above), and $I_8(\mathbf{M}, \mathbf{N})$=**C**: **M**⊗**N** in the left-hand equation, an angular-base invariant such as the right-hand equation is considered in [19]. Because the interaction mechanism of the constituent materials is a result of the fiber rotation, the angular-base invariant $I_8^* = I_8/\sqrt{I_4\, I_6} = \cos\varphi$ is employed by the mechanical interaction potential Ψ_τ. The scalar quantities q and r are fiber tensions as reactions associated with the inextensibility constraints presented in Eq. (1) such as $I_4 = 1$ and $I_6 = 1$, respectively. The functional forms of the potentials in Eq. (1) are defined as [19]

$$\Psi_{\mathrm{M}} = c_{10}\big(I_1 - 3\big) - p(J-1),\ \Psi_{\mathrm{F}} = \frac{k_1}{2}\sum_{i=4,6}\big(I_i - 1\big)^2 \tag{3}$$

and

$$\Psi_{\tau} = \frac{c_1}{2c_2}\left[\exp\Big(c_2\big(I_8^* - \cos(2\theta)\big)^2\Big) - 1\right] + c_3\big(I_8^* - \cos(2\theta)\big)^2. \tag{4}$$

The constants c_{10}, k_1, c_1, and c_3 are positive material parameters with the dimension of stress, while c_2 is a positive, dimensionless parameter. The contribution of the mechanical interactions including matrix-fiber and fiber-fiber interactions are determined by the parameters (c_1, c_2, c_3). The latter is originated from the distortion of fibers at their intersections while the former is a result of the angle change between fibers. They are experimentally shown in next sections (see Section 5.4). The scalar p serves as an indeterminate Lagrange multiplier that can be identified as hydrostatic pressure. The constant $\cos(2\theta)$ is the cosine of the current angle between fibers in the undeformed configuration. For a representative region corresponding to the undeformed composite shown in Fig. 1(a), the relations between (α, β, θ, φ) are illustrated in Fig. 1(b) (modified from [19]).

Remark 3.1. In addition to the quadratic function, the first term in potential (4) in the form of an exponential function is necessary for a better conformability of the constitutive model with experimental data of composites with various flexibilities. In the next sections (see Section 6) it is shown that generally, the quadratic or the exponential terms alone does not fit properly the experimental results of the flexible PDMS-GF composite while the latter is individually able to fit the stress-stretch responses of the PUR-GF composite with less flexibility.

3.2. Material characterization framework

When determining the material parameters of the mechanical interaction potential, the constraint (I) in Eq. (1) is considered, while, the constraint (II) is applied for obtaining the material constants of the fibers. For a composite with orthogonal fibers (i.e. $2\theta = \pi/2$) stretched in the $\mathbf{E}_1$ direction, the constraint (I) gives the deformation gradient as

$$\mathbf{F}_I = \begin{bmatrix} \lambda & 0 & 0 \\ 0 & \sqrt{2-\lambda^2} & 0 \\ 0 & 0 & \frac{1}{\lambda\sqrt{2-\lambda^2}} \end{bmatrix} \tag{5}$$

while the deformation gradient corresponding to the constraint (II) is simplified to $\mathbf{F}_{II} = \mathrm{diag}[\lambda, \lambda^{-1/2}, \lambda^{-1/2}]$, where λ denotes the value of the stretch in the direction $\mathbf{E}_1$.

Remark 3.2. It is noted that the angle 2θ can be varied depending on the woven fabric used as reinforcement. Therefore, the constitutive framework is also usable for composite that its fibers are not necessarily orthogonal at the undeformed state. For instance, for a composite with $2\theta = \pi/3$ (θ is half of the angle subtended by **M** and **N**) stretched in the $\mathbf{E}_1$ direction, Eq. (5) reads

$$\mathbf{F}_I = \begin{bmatrix} \lambda & 0 & 0 \\ 0 & \sqrt{4-3\lambda^2} & 0 \\ 0 & 0 & \frac{1}{\lambda\sqrt{4-3\lambda^2}} \end{bmatrix} \tag{6}$$

Considering the strain-energy in Eq. (1) with the predefined potentials in (3) and (4), the Cauchy stresses corresponding to the deformation gradients $\mathbf{F}_I$ (recall Eq. (5)) and $\mathbf{F}_{II}$ can be obtained, respectively, as

$$\sigma_I = 2\lambda^2\big(\lambda^2-1\big)\left\{\frac{2\mu}{\lambda^4\big(2-\lambda^2\big)^2} + c_1\exp\Big[c_2\big(\lambda^2-1\big)^2\Big] + 2c_3\right\} \tag{7}$$

and

$$\sigma_{II} = 2\mu\big(\lambda^2 - \lambda^{-1}\big) + 2k_1\lambda^2\big(\lambda^2-1\big) \tag{8}$$

The material properties of the mechanical interaction (c_1, c_2, c_3) as well as the fiber constant (k_1) can be determined independently through the Eqs. (7) and (8), respectively, without needing inverse finite element simulations or analytical solutions. Before that, the constant of the matrix (μ) appeared in the two above equations should be obtained (for a detailed discussion on the constitutive modeling and experimental characterization of isotropic elastomers, the reader is referred to, for example, [25] and [26] and references therein). The angular-base invariant, the deformation gradient, and the constitutive relations presented in this section, i.e. (I_8^*, F_I, σ_I, σ_{II}), form a constitutive framework, based on which the matrix-fiber mechanical interaction can be analytically quantified.

4. Finite element modeling

The material is treated as nearly incompressible; therefore, for the finite element simulations, the MFI model is decomposed into volumetric and isochoric parts. Accordingly, the Cauchy stress and elasticity tensors should be decoupled into volumetric and isochoric parts in an Eulerian description, which are given in Appendix A for the reader interested in using the model. The model is implemented through a user-defined interface UMAT in the commercial nonlinear FE software Abaqus. For the algorithmic implementation, it is assumed that two fiber families do not contribute to the deformation when they are compressed. Hence, the potentials reconstructed by them are assumed to be zero when $\bar{I}_4 < 1$ and $\bar{I}_6 < 1$. The volumetric contribution $\mathrm{U}_{\mathrm{vol}}(J)$ is characterized by the bulk modulus $\kappa > 0$, which is independent of the deformation. This parameter is treated as a penalty parameter by using a large value of the bulk modulus as $\kappa = 10^5$ MPa. For an approximation technique such as the finite element method, the tangent stiffness matrix $\mathbb{D}$, i.e. DDSDDE variable in Abaqus, becomes increasingly ill-conditioned for increasing κ. For that case, the reduced integration method and hybrid finite element methods are used to weaken the penalty function. Hence, the geometries are discretized with 3D reduced integration, eight-node linear solid elements with hybrid formulation (C3D8RH). Two representative examples are presented in Appendix A in order to illustrate the performance of the constitutive model through the finite element implementation by comparison to the analytical solutions. The uniaxial extension and simple shear tests on a unit cube with dimension $1 \times 1 \times 1$ mm^3 are carried out. For verification of the model performance, the computational (FEM) and analytical solutions associated with both examples are compared

5. Experimental

5.1. Enhanced interface properties

A combination of a soft matrix with stiff fibers results in remarkable fiber-fiber and matrix-fiber mechanical interactions due to the chemically formed adhesion bonds at the interfaces so that weak adhesion

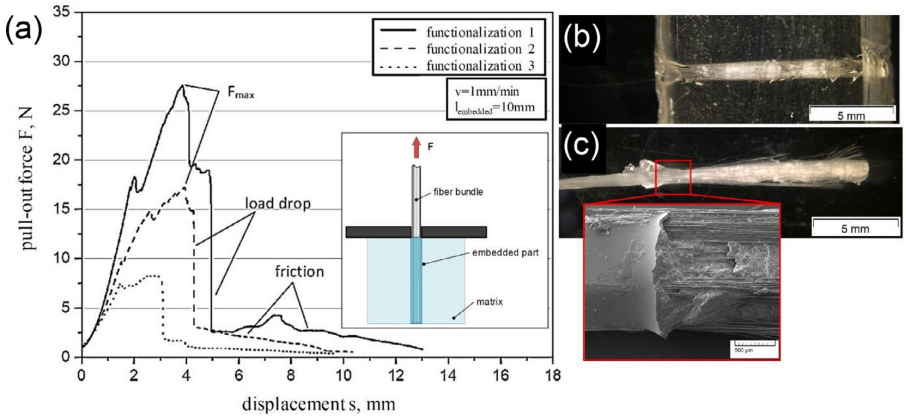

Fig. 2. Enhanced interface properties using fiber bundle pull-out tests: (a) load-displacement curve with schematic test performance of the fiber bundle pull-out test; (b) optical analyses of the matrix before the test; (c) fiber bundle including an SEM picture after the testing.

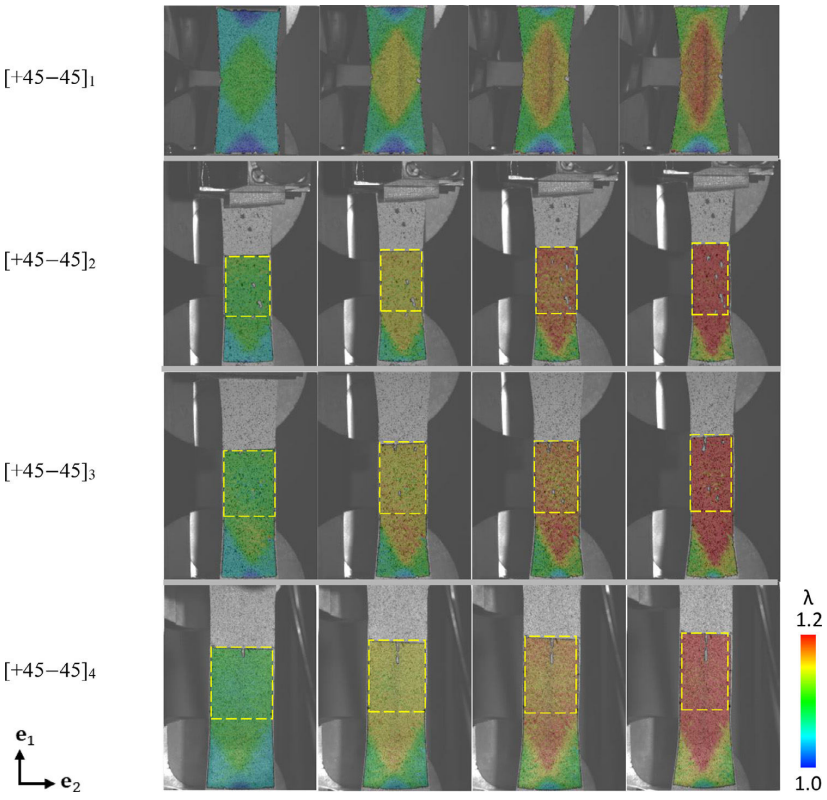

Fig. 3. 3D full-field, local stretch maps of samples with the fiber orientation [+45− 45] shown for the PDMS-GF composites for the stretches $\lambda_1 = (1.09,\ 1.14,\ 1.17,\ 1.2)$.

bonds result in early matrix-fiber debonding [27]. Effective mechanical interaction is not achieved unless an enhanced bonding between the constituent materials of the composite is formed in advance. Hence, fiber bundle pull-out tests are conducted to investigate the interface properties between a bundle and the surrounding matrix (fiber debond techniques can be found in [28,29]). The first results revealed that the surface treatment on the bundle has a significant effect on the pull-out performance and further on the matrix-fiber bonding, shown in Fig. 2.

It can be seen that each surface modification reveals a clearly different load-displacement behavior depending on the tailored matrix-fiber adhesion. In this work, the optimal fiber surface treatment (functionalization 1, organosiliane-based treatment with vinyltriethoxysilane-groups) for the preparation of the composite samples is considered, which is essential for the pronounced strength of the matrix-fiber adhesion. The samples, so prepared, are expected to show their optimal performance in regard to the contribution of the mechanical interaction.

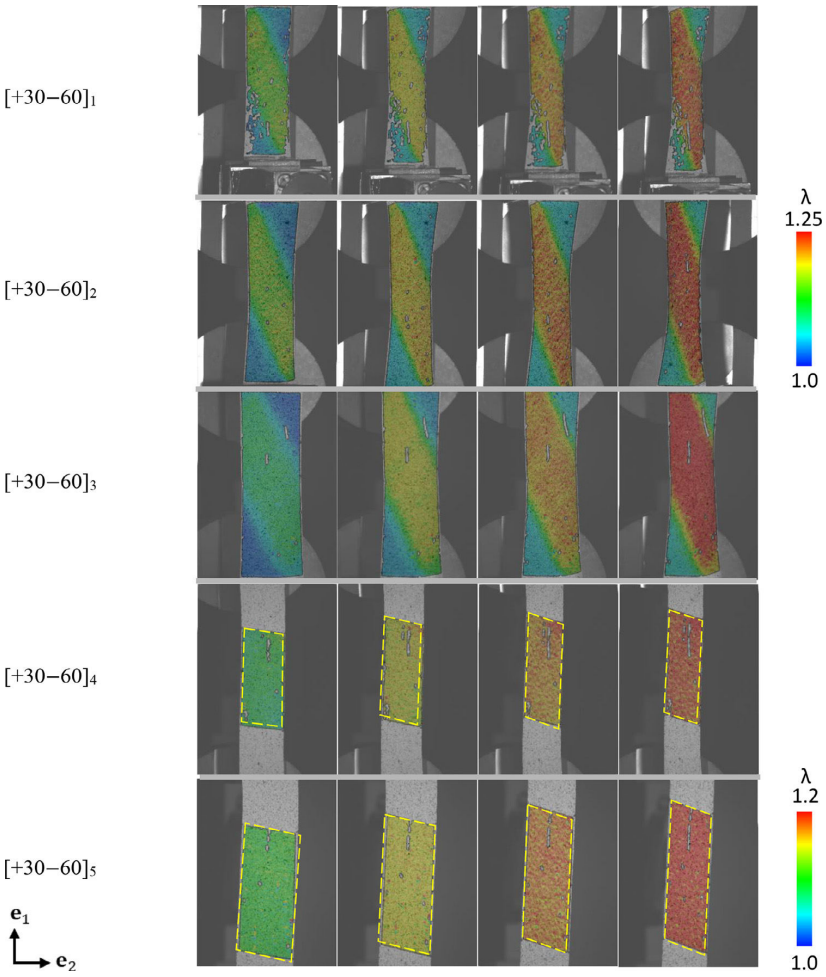

Fig. 4. 3D full-field, local stretch maps of samples with the fiber orientation [+30− 60] shown for the PDMS-GF composites for the stretches $\lambda_1 = (1.09,\ 1.14,\ 1.17,\ 1.2)$.

5.2. 3D full-field stretch analysis and sample geometry

3D full-field, high-resolution images are captured via the DIC method. It is carried out for the samples presented in Table 1 during tensile tests on PDMS-GF and PUR-GF composites. The local stretch maps corresponding to the samples $[+45{-}45]_{1,2,3,4}$ and $[+30{-}60]_{1,2,3,4,5}$ are depicted respectively in Figs. 3 and 4 for the PDMS-GF composites, shown for the stretches $\lambda_1 = (1.09, 1.14, 1.17, 1.2)$. Movies of stretch maps during tensile loadings are provided in supplementary materials [30]. Additional information is available upon request. Identical stretch maps are also observed for PUR-GF composites (not shown) and are presented in the supplementary materials.

In the literature, for the purpose of the material characterization using thin tensile samples, stress-free boundary conditions in both the transverse direction to the loading and through thickness are assumed, aiming at finding a relation between principal stretches. Similarly, in this work, the constitutive Eqs. (7) and (8) were determined by imposing stress-free boundary conditions such as $\sigma_{22} = 0$ and $\sigma_{33} = 0$. The material characterization procedure necessitates finding a region by which a homogeneous stretch map can be identified and the condition $\sigma_{22} = 0$ is satisfied as well. Doing so enables us to determine the principal stretches λ_1 and λ_2 in a large enough evaluation region so that, at a specific deformation, their values do not change a lot across the region. The local stretch maps shown in Figs. 3 and 4 indicate that this condition is fulfilled by samples having an aspect ratio of $\xi = 3/\tan\alpha$. This aspect ratio introduces a sample geometry as shown in Fig. 5, which is featured by an 'interest area'. This sample geometry provides a homogeneous stretch map across the interest area. The interest area is defined in a way that none of the fibers inside this region are clamped in the fixture, and therefore no clamping effects have to be considered. The stretches in the loading direction $\mathbf{e}_1$ are calculated based on changes in the length of the interest area. Accordingly, $\lambda_1 = L/(\mathrm{a}/\tan\alpha)$, where L is the length of the interest area in the deformed configuration, while $\mathrm{a}/\tan\alpha$ denotes its undeformed length, shown in the figure. For samples with an aspect ratio other than $\xi = 3/\tan\alpha$, a representative region for the interest area can not be identified, therefore the stretches are calculated based on changes in the length of the samples in the loading direction $\mathbf{e}_1$.

5.3. Stress-stretch responses of tensile tests

The average stress-stretch results of the PDMS-GF and PUR-GF composites corresponding to the samples tabulated in Table 1 are presented in Fig. 6(a) and (b) and Fig. 6(c) and (d), respectively. It is seen that for

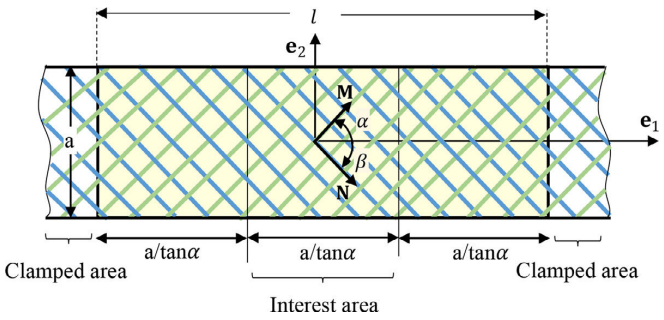

Fig. 5. The sample geometry featured by an interest area and aspect ratio of $\xi = 3/\tan\alpha$ corresponding to a fiber-reinforced material with two fiber families initially aligned in $\boldsymbol{M} = \cos\alpha\boldsymbol{e}_1 + \sin\alpha\boldsymbol{e}_2$ and $\boldsymbol{N} = \cos\beta\boldsymbol{e}_1 + \sin\beta\boldsymbol{e}_2$ directions.

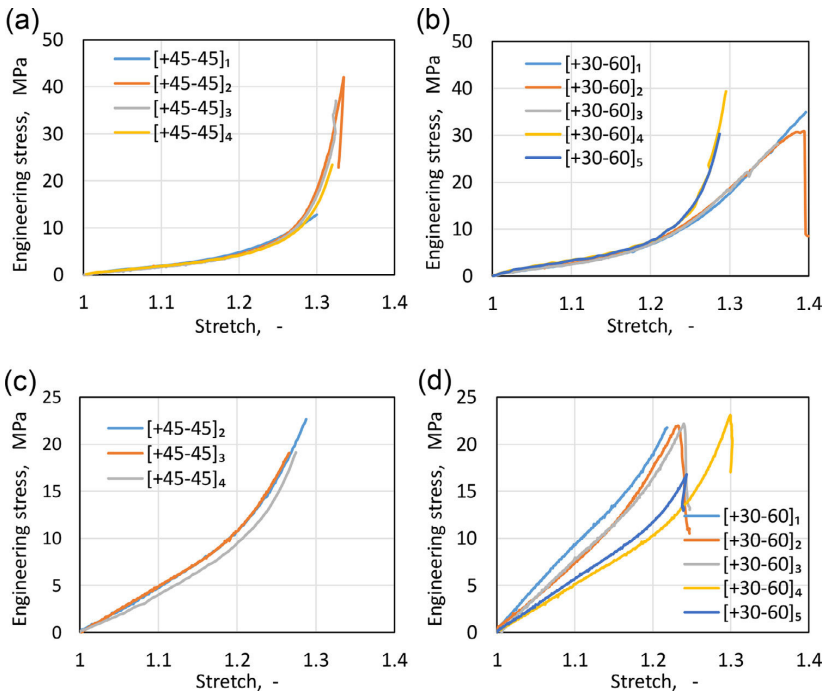

Fig. 6. Experimental stress-stretch responses of samples: (a) and (b) PDMS-GF composites; (c) and (d) PUR-GF composites (the results of the two samples $[+45-\ 45]_4$ and $[+30-\ 60]_4$ given respectively in the panel a and b are adapted from [19]).

a specific material anisotropy, regardless of the dimension of the samples but the same aspect ratio, they show relatively similar mechanical responses.

5.4. Microscale in situ optical characterization

To monitor the local change of the fiber angle during stretching the composites, microscale *in situ* optical characterizations are conducted using the sample $[+45-\ 45]_4$. Unlike the opaque PUR-GF composites, the transparency of the PDMS-GF samples allows us to monitor optically the change of fiber angle during loading experiments. The change of fiber angle is the origin of the mechanical interactions. It is quantified for the finite orange region indicated in Fig. 7(a) as the cosine of the current angle between deformed fibers denoted by $\cos\varphi$. The results are shown in Fig. 7(b) and optically illustrated in Fig. 7(c) for specific stretches. It is noted that since a homogeneous stretch map for the blue region indicated in Fig. 7(a) is already observed (see the stretch maps in Fig. 3 for the sample $[+45-\ 45]_4$), therefore, a finite area chosen therein, such as the orange region, is almost representative of a bigger area. Further illustrations concerning the mechanical interactions can be referred to the distortion of fibers at their intersections. It is shown optically in Fig. 8, which is representative of significant fiber-fiber interaction.

5.5. Wrinkling of stretched samples

The thin, flexible samples are prone to the formation of unwanted wrinkles when stretched. The presence of wrinkles affects directly the resultant driving force along the loading direction [31,32]. While it is a common phenomenon in stretched thin samples, however, it should be treated with caution. It is evaluated by visualizing the out-of-plane deformation maps taken via DIC. The wrinkling patterns at the mid-cross-section of a stretched composite are displayed exemplarily for the sample $[+45-\ 45]_1$ in Fig. 9(a). In general, the wrinkling is determined using the wrinkle wavelength as well as the amplitude of the wrinkles, see Fig. 9 (b), which both are related together [31,32]. The shape of the wrinkles for the composites $[+45-\ 45]_1$, $[+45-\ 45]_4$, $[+30-\ 60]_3$, and $[+30-\ 60]_4$ are plotted in Fig. 9(c), (d), (e), (f), respectively, for specific stretches. Note that the same wrinkling patterns are observed

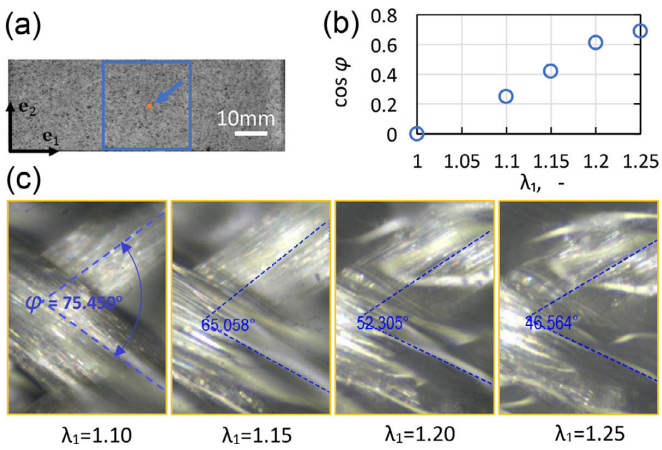

Fig. 7. Microscale in situ optical characterization of the current angle between deformed fibers during loading experiments: (a) an orange region representative of the blue area is chosen; (b) experimental results with respect to the current angle between deformed fibers determined for the orange region indicated in panel a; and (c) respective optical illustrations.

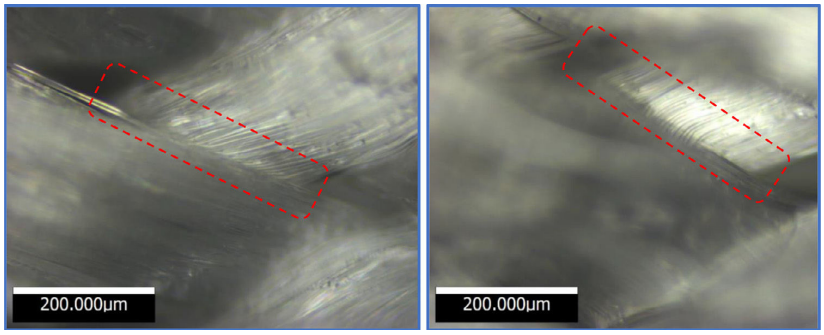

Fig. 8. Fiber distortion at the region of the intersection of the fibers results in extensive fiber-fiber mechanical interaction.

for the composites $[+45-45]_{2,3,4}$ and $[+30-60]_{4,5}$, therefore, only one was shown for each.

6. Results

6.1. Correlation of analytical and experimental studies

The analytical study on the mechanical interactions presented in a constitutive framework in Section 3 is further evaluated against the experimental results in three stages as follows. Since the analytical solutions are obtained based on the samples with the material anisotropy as [+45− 45], therefore, herein the experimental data of PDMS-GF and PUR-GF materials reported for the sample $[+45-45]_4$ are used for the three stages (except for the evaluation of the angle change between fibers where the data of PDMS-GF is only used, in that, the opacity of PUR-GF does not allow to monitor the change of fiber angle).

(i) The principal stretches defined in the deformation gradient $\mathbf{F}_I$ (Eq. (5)) are compared with the stretch maps obtained via digital image correlaltion in the loading direction, denoted by λ_1, and transverse to the loading, represented by λ_2. The results are shown in Fig. 10(a) and (b) for the PDMS-GF and PUR-GF materials, respectively. The stretch maps are reported based on the average stretches determined across the interest area (see Fig. 3).

(ii) The angular-base deformation invariant denoted by I_8^* (recall Eq. (2)) is plotted in Fig. 11 against the loading stretches $\lambda_1 \equiv \lambda$. Considering the constraint *(I)* and therefore $\theta = \pi/4$ (see Section 3.2), they give the deformation gradient as $\mathbf{F}_I$, defined in Eq. (5). For this specific deformation state, $\mathbf{C}_I = \mathbf{F}_I{}^{\mathrm{T}}\mathbf{F}_I$, $\mathbf{M} = \cos(\pi/4)(\mathbf{E}_1+\mathbf{E}_2)$, $\mathbf{N} = \cos(\pi/4)(\mathbf{E}_1-\mathbf{E}_2)$ and $I_8 = \mathbf{C}_I$: $\mathbf{M}\otimes\mathbf{N}$. Replacing now the former relations into the latter equation yields $I_8 = \lambda^2 - 1$. In Section 3.1, the angular-base invariant is defined as $I_8^* = I_8/\sqrt{I_4\, I_6}$ that considering the constraint *(I)*, i.e. $I_4 = I_6 = 1$, it gives $I_8^* = I_8$. Therefore, the angular-base invariant is simply defined as $I_8^* = \lambda^2 - 1$ ($\lambda_1 \equiv \lambda$). Included in the figure are the test results corresponding to the cosine of the current angle between deformed fibers, i.e. cos φ, captured via the micrographs in Section 5.4.

(iii) Representative conformability of the constitutive equation σ_I (Eq. (7)) with experimental results is visualized in Fig. 12(a) and (b) for the PDMS-GF and PUR-GF composites, respectively, indicating good qualitative agreements. It is carried out simply by fitting Eq. (7) to the respective stress-stretch responses of the composites, without needing the fibers' properties. Before that, the material properties of the PDMS and PUR matrix (i.e. μ) are obtained using uniaxial tensile tests. Keeping now the matrix parameter, the material constant of the fibers, i.e. k_1, are determined simply by fitting Eq. (8) to the results of tensile tests on composites in their fiber directions. Since the two fiber families have the same contributions to the deformation, therefore, they share an identical material constant. Upon fitting, the material parameters are given in Tables 2 and 3 for the PDMS-GF and PUR-GF composites, respectively. The data fitting is

Table 2
Material constants of the PDMS-GF composite (adapted from [19]).

Contribution	μ, MPa	k_1, MPa	c_1, MPa	c_2, –	c_3, MPa
Matrix	0.380				
Fiber		697.0			
Interaction			0.0355	9.6790	1.3770

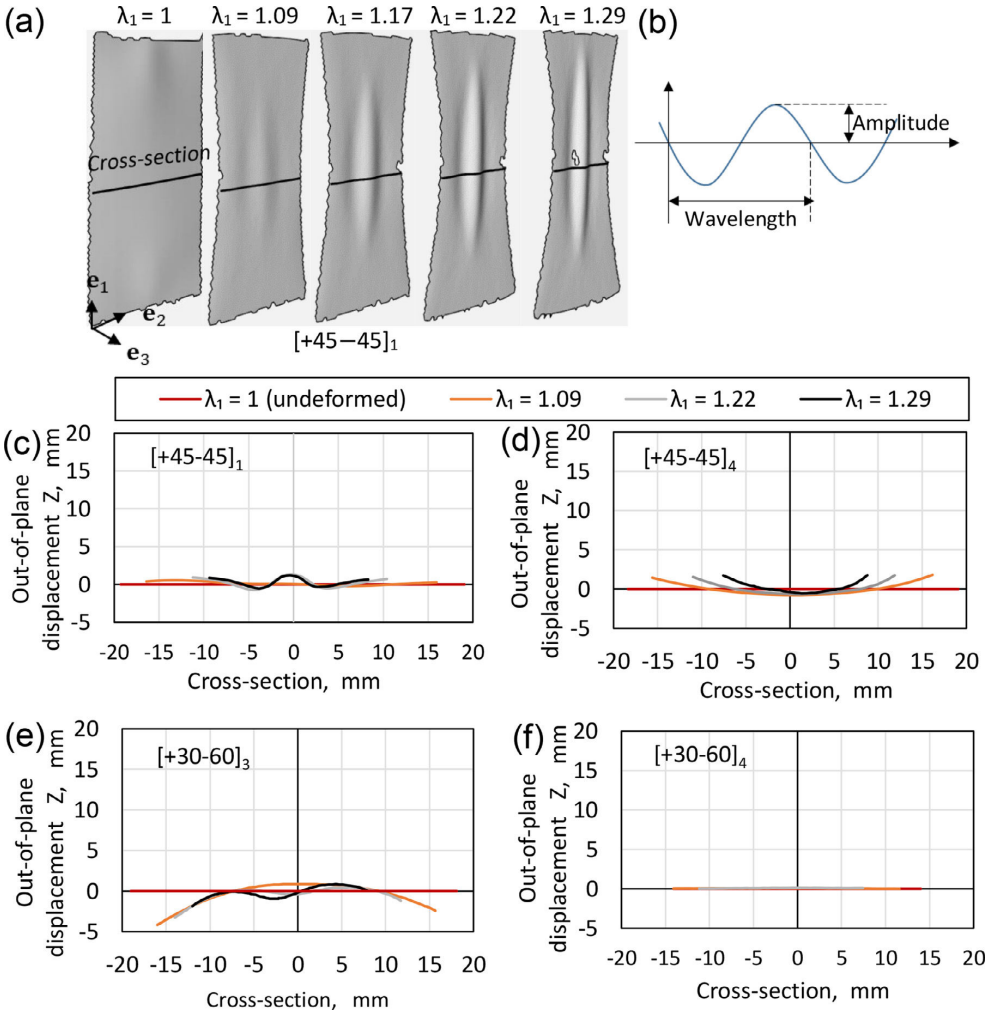

Fig. 9. a) The illustrations of the wrinkling as out-of-plane displacement in the e_3 direction for the stretched samples recorded by the DIC.

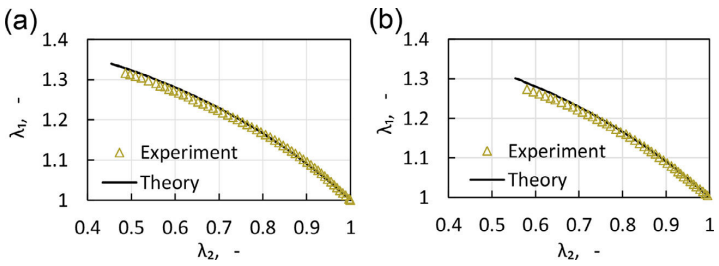

Fig. 10. Representative stretch maps recorded via DIC compared with the theory.

Table 3
Material constants of the PUR-GF composite.

Contribution	μ, MPa	k_1, MPa	c_1, MPa	c_2, –	c_3, MPa
Matrix	0.480				
Fiber		697.0			
Interaction			0.02180	12.990	3.7550

performed using a non-linear least-squares optimization tool from Matlab to minimize the discrepancy between the model results and the experimental data via the function

$$\chi = \sum_{i=1}^{k} \left\| \sigma_i^{\text{model}} - \sigma_i^{\text{experiment}} \right\|^2. \tag{9}$$

where n is the number of experimental points and σ_i are components of the respective stress vectors. It is noted that for a large number of ma-

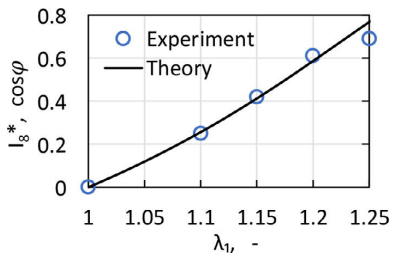

Fig. 11. The current angle between deformed fibers determined by the theory (I_8^*) and in situ optical imaging represented by cos φ.

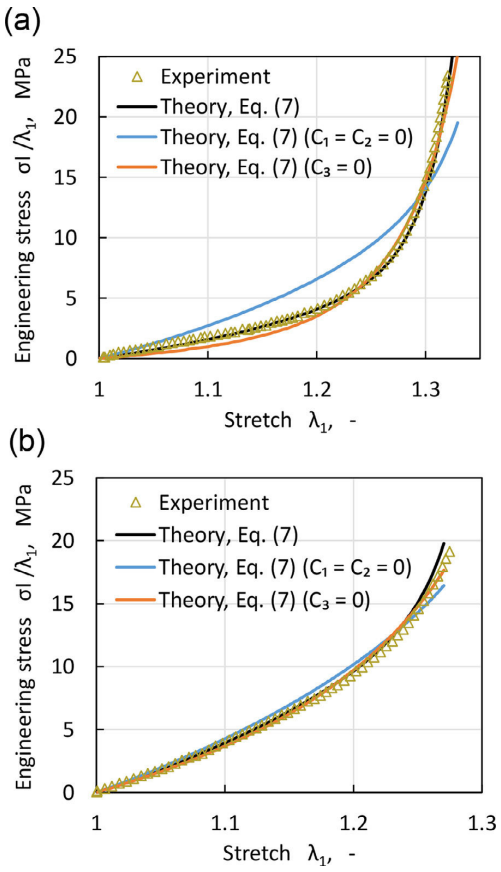

Fig. 12. Plots showing the conformability of the constitutive framework with stress-stretch responses of the composites as well as the effet of the quadratic and the exponential terms of the constitutive model: (a) PDMS-GF samples; (b) PUR-GF composites.

terial parameters the least-squares optimization can lead to problems of non-uniqueness associated with the sensitivity of the material parameters to the initial starting point provided by the user [33]. Whereas the mechanical interaction potential with only three constants is fitted independently of the matrix and the fiber parameters, nevertheless, different sets of initially-guessed interaction parameters are tested as these may lead to different fitting results. In all tests, considering physically-reasonable cases, the interaction parameters are nearly identical.

Further illustrations in Fig. 12 show the effect of the exponential and the quadratic terms of Eq. (4) in the conformability of the constitutive model with the respective experimental data when neglected. It is generally seen that the quadratic or the exponential terms alone does not fit properly the experimental results of the flexible PDMS-GF composite showing high nonlinearity, while, the latter is individually able to fit the stress-stretch responses of PUR-GF composites satisfactorily. Therefore, based on the nonlinearity degree of the stress-stretch responses of a certain composite, particular terms can be considered.

Remark 6.1. Note that the theoretical results given in Fig. 12 are based on the contributions of the matrix and mechanical interaction potentials assuming inextensible fibers, i.e. $\Psi_M + \Psi_\tau - \frac{1}{2}q(I_4 - 1) - \frac{1}{2}r(I_6 - 1)$. While, for the purpose of the finite element simulations the contributions of the fibers are involved, i.e. the constitutive equation is computed based on $\Psi_M + \Psi_F + \Psi_\tau$. Therefore, the results computed by the fitting and from the finite element simulation should be distinguished.

6.2. The importance of sample aspect ratio

Whereas there are standards for characterizing the constituent materials of a composite, the characterization of their mechanical interactions is not yet evaluated satisfactorily in the literature. In this section, the importance of the sample aspect ratio is illustrated by a combined

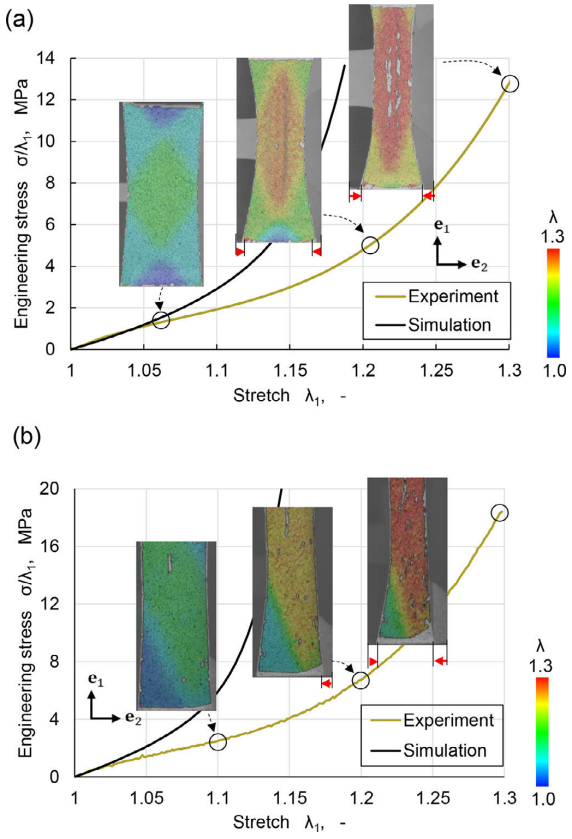

Fig. 13. The importance of the sample aspect ratio is illustrated comparing the experimental and simulation stress-stretch results: (a) the sample $[+45-45]_1$ with an aspect ratio of $\xi = 2$; (b) the sample $[+30-60]_3$ with $\xi = 3$. The transverse slippages at clamps are indicated by red arrows (the material parameters from Table 2 are used for the simulations).

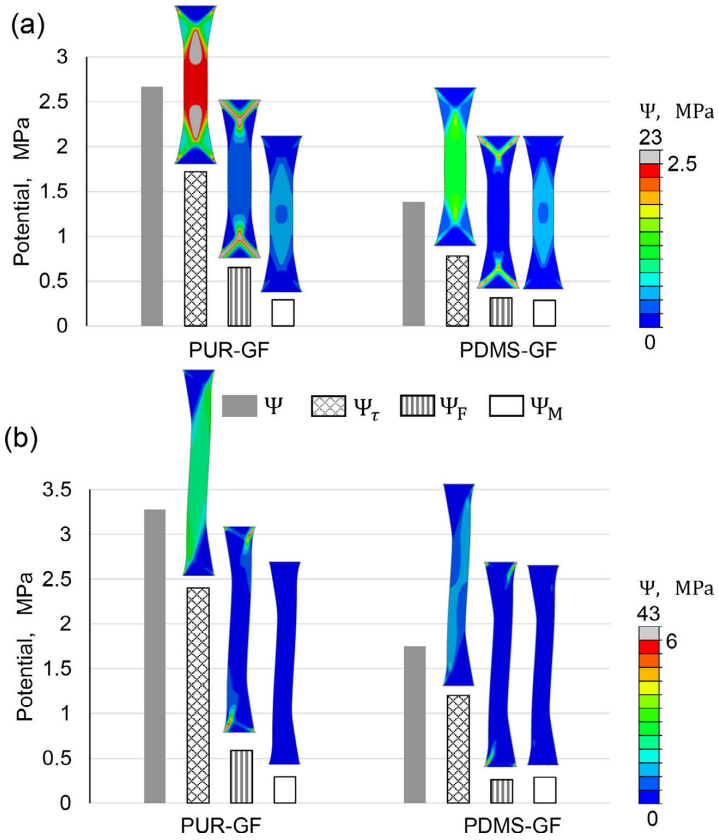

Fig. 14. Contribution of the material phases shown for (a) sample $[+45-\ 45]_4$ and (b) sample $[+30-\ 60]_4$, subjected to a stretch of $\lambda_1 = 1.25$. It is indicated by the spatial distribution and the quantitative measurement of the potentials associated with the matrix, fibers, mechanical interactions, and total energy stored in the composites.

experimental and simulation study on composites given in Table 1 with aspect ratios other than that is suggested by Fig. 5 as $\xi = 3/\tan\alpha$. To end this, the stress-stretch responses of the PDMS-GF composites considering the samples $[+45-\ 45]_1$ with $\xi = 2$ and $[+30-\ 60]_3$ with $\xi = 3$ are compared with the simulation results in Fig. 13(a) and (b), respectively. It is noted that the samples $[+30-\ 60]_{1,2,3}$ show similar mechanical responses as depicted already in Fig. 6(d), therefore, one of them is only chosen, say $[+30-\ 60]_3$. For the finite element simulations, the material properties of the PDMS-GF given in Table 2 are used. Although a new clamping system was designed to avoid slippage of the specimens in the loading direction $\mathbf{e}_1$, which applies the clamping forces on five different areas of samples, it is seen that however, the presence of the transverse slippage at clamps, shown by red arrows in Fig. 13, causes substantial deviations between the results. The reason can be related to the inappropriate choice of the sample aspect ratio causing a high-stress field throughout the sample, which is continued to the clamping area. The matrix in the clamping area, because of its soft nature, cannot withstand high-stress values and therefore transverse slippages of the samples occur in the clamps. The results necessitate considering an appropriate aspect ratio when preparing the tensile samples, especially if there is a significant difference between the stiffness of the constituent materials.

Remark 6.2. It is noted that, in addition to the transverse slippage of the specimen at clamps, the matrix-fiber slippage might be another reason for the substantial deviations between the experimental and simulation stress-stretch results shown in Fig. 13. However, monitoring the local deformations via the micrographs (such as Fig. 7) and especially the stretch maps shown in Figs. 3 and 4 are not indicative of suspicious regions reflecting the matrix-fiber slippage. This issue is more likely to occur in dry woven structures.

The importance of the sample aspect ratio is further discussed by the evaluation of the shape of wrinkling in stretched samples. The presence of wrinkles directly affects the resultant driving force along the loading direction [31,32], while, the latter is used in the material calibration procedure as input data. It is seen that in Fig. 9 the composites with the aspect ratio of $\xi = 3/\tan\alpha$ show less wrinklings. It implies that the stress-stretch responses of the stretched samples with this aspect ratio are more reliable for the purpose of the material calibration.

6.3. Contribution of material phases

To understand how much is the individual contributions of the material phases in the mechanical behavior of fiber-reinforced materials, composites are simulated at a certain deformation. The results of previous sections indicate that the composites with an aspect ratio of $\xi = 3/\tan\alpha$, such as $[+45-\ 45]_{2,3,4}$ and $[+30-\ 60]_{4,5}$, exhibit reliable mechanical responses—i.e. low wrinkling, a large area of homogenuous deformation, and conformability of the constitutive equation to the stress-stretch data. Accordingly, the PDMS-GF and PUR-GF materials considering the samples $[+45-\ 45]_4$ and $[+30-\ 60]_4$ are chosen and then simulated up to a stretch of $\lambda_1 = 1.25$. The spatial distributions of the stored energies associated with the matrix (Ψ_M), fibers (Ψ_F), and mechanical interactions (Ψ_τ) as well as the total strain-energy density (Ψ) are displayed in Fig. 14. It is emphasized that the contributions of the three material phases are obtained independently of one another. It

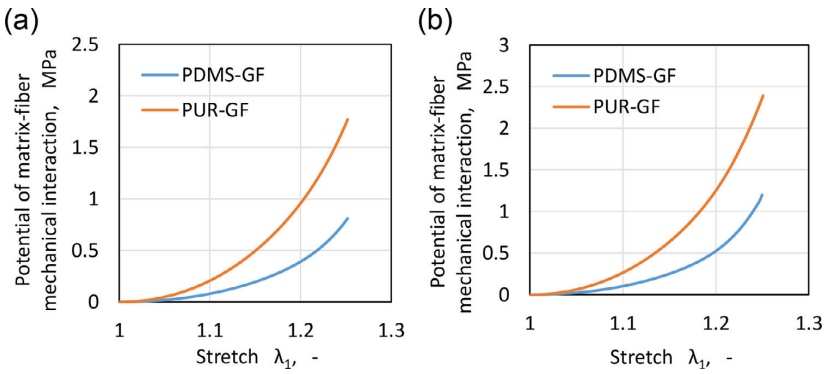

Fig. 15. Finite element results associated with the potentials of the matrix-fiber mechanical interactions shown for PDMS-GF and PUR-GF composites during uniaxial tensions: (a) $[+45-45]_4$; (b) $[+30-60]_4$ samples.

provides a clear understanding of the features involved in the mechanical behavior. Moreover, how the potentials associated with the matrix-fiber mechanical interaction for PDMS-GF and PUR-GF composites are varied under tensile deformations are illustrated in Fig. 15(a) and (b) for $[+45-45]_4$ and $[+30-60]_4$ samples, respectively. The quantitative measurements together with the spatial distributions of the respective potentials signify that the matrix-fiber mechanical interaction is the underlying mechanism contributing to the constitutive behavior of hyperelastic fiber-reinforced composites.

7. Conclusion

In summary, a combined experimental, analytical, and simulation study is carried out to quantify the matrix-fiber mechanical interactions in hyperelastic fiber-reinforced materials. To end this, fiber bundle pull-out tests are perfomed considering different matrix-fiber interphase properties and then optimal fiber surface treatment for the preparation of the composite samples is considered. Since there does not exist standards for characterization of matrix-fiber mechanical interactions, several samples with different aspect ratios and various material anisotropy are fabricated with soft, nearly incompressible matrix and endless, twill woven fabrics as reinforcement. For the purpose of characterizing the matrix-fiber mechanical interactions, local stretch maps of composites are captured via digital image correaltion during loading experiments. Moreover, the local change of angle between deformed fibers, as the origin of the mechanical interactions, is monitored using *in situ* optical imaging. The stress-stretch responses of all samples as well as the wrinkling patterns of specific composites are reported. The analytical study is carried out within a constitutive framework specialized for the matrix-fiber mechanical interactions [19]. The framework including angular-base invariant, deformation gradient, and constitutive behavior is compared with the respective experimental results explained above, showing good qualitative agreements in all comparisons. The finite element implementation of the model is then presented for reader interested in using the model. A couple of combined experimental and simulation study is carried out to highlight the importance of the sample aspect ratio for the characterization of the matrix-fiber mechannical interactions. The finite element analysis of different composites signify that the underlying mechanism contributing to the mechanical response of fiber-reinforced elastomers is attributed to the matrix-fiber mechanical interactions.

Declaration of Competing Interest

The authors declare that they have no known competing financial interests or personal relationships that could have appeared to influence the work reported in this paper.

CRediT authorship contribution statement

M.R. Mansouri: Conceptualization, Investigation, Software, Formal analysis, Writing - original draft. **J. Beter:** Investigation, Writing - original draft. **P.F. Fuchs:** Funding acquisition, Supervision, Writing - review & editing. **B. Schrittesser:** Supervision, Writing - review & editing. **G. Pinter:** Writing - review & editing.

Acknowledgment

The research work was performed at the Polymer Competence Center Leoben GmbH (PCCL, Austria) within the framework of the COMET-program of the Federal Ministry of Science, Research and Economy with contributions by Montanuniversitaet Leoben (Chair of Materials Science and Testing of Polymers, Austria), Grant No. 854178.

Supplementary materials

Supplementary material associated with this article can be found, in the online version, at doi:10.1016/j.ijmecsci.2021.106268.

Appendix A. Finite element implementation

A.1. Decoupled form of the model

For the computational implementation, the proposed model is treated as a nearly incompressible material. For nearly incompressible materials, the deformation gradient $\mathbf{F}$ and corresponding strain measure $\mathbf{C}$ are multiplicatively decomposed into volume-changing (volumetric) and volume-preserving (isochoric) parts as $\mathbf{F} = J^{1/3}\bar{\mathbf{F}}$ and $\mathbf{C} = J^{2/3}\bar{\mathbf{C}}$, in which $J = \det \mathbf{F}(\mathbf{X}) > 0$ represents the local volume ratio at point $\mathbf{X}$ with $\det \bar{\mathbf{F}} \equiv 1$. Because $\mathbf{F}$ is decoupled it is assumed that the total potential function Ψ defined in Eq. (1) (considering $q,\ r = 0$) can be described in terms of an energy contribution $U_{vol}(J)$ dependent only on J, i.e. a purely volumetric contribution, and a contribution $\bar{\Psi}^0(\overline{\mathbf{C}},\{\mathbf{M},\mathbf{N}\})$ from the isochoric deformation via $\bar{\mathbf{C}}$. Thus,

$$\Psi(\mathbf{C},\ \{\mathbf{M},\mathbf{N}\}) = \bar{\Psi}^0\left(\overline{\mathbf{C}},\{\mathbf{M},\mathbf{N}\}\right) + U_{vol}(J) \tag{A.1}$$

with isochoric potential function $\bar{\Psi}^0$ as

$$\bar{\Psi}^0\left(\overline{\mathbf{C}},\{\mathbf{M},\mathbf{N}\}\right) = \bar{\Psi}^0_M(\bar{I}_1,\bar{I}_2) + \bar{\Psi}^0_F(\bar{I}_4,\bar{I}_6) + \bar{\Psi}^0_\tau(\bar{I}^*_8) \tag{A.2}$$

where isochoric invariants are $\bar{I}_1 = J^{-2/3}I_1$, $\bar{I}_2 = J^{-4/3}I_2$, $\bar{I}_i = J^{-2/3}I_i$, $i = 4,\ 6,\ 8$, and $\bar{I}^*_8 = I^*_8$.

The volumetric strain energy U_{vol} is not critical here (as it is used as penalty function), and it is convenient to adopt the form of U_{vol} as

$$U_{vol}(J) = \frac{1}{4}\kappa\left(J^2 - 1 - 2\ln J\right) \tag{A.3}$$

where κ is the compressibility parameter with the dimension of the stress.

A.2. Cauchy stress tensor

The decoupled form of the Cauchy stress corresponding to Eq. (A.1) is obtained. First, the fictitious second Piola-Kirchhoff stress tensor $\bar{\mathbf{S}}^0$ is defined by differentiating Eq. (A.2) with respect to $\bar{\mathbf{C}}/2$ that reads

$$\bar{\mathbf{S}}^0 = 2\frac{\partial\bar{\Psi}^0}{\partial\bar{\mathbf{C}}} = 2\frac{\partial\bar{\Psi}^0_{\mathrm{M}}}{\partial\bar{I}_1}\mathbf{I} + 2\frac{\partial\bar{\Psi}^0_{\mathrm{F4}}}{\partial\bar{I}_4}(\mathbf{M}\otimes\mathbf{M}) + 2\frac{\partial\bar{\Psi}^0_{\mathrm{F6}}}{\partial\bar{I}_6}(\mathbf{N}\otimes\mathbf{N}) + 2\frac{\partial\bar{\Psi}^0_{\tau}}{\partial\bar{I}^*_8}\left(\frac{\mathbf{M}\otimes\mathbf{N}+\mathbf{N}\otimes\mathbf{M}}{\sqrt{\bar{I}_4\bar{I}_6}} - \bar{I}^*_8\left(\frac{\mathbf{M}\otimes\mathbf{M}}{\bar{I}_4}+\frac{\mathbf{N}\otimes\mathbf{N}}{\bar{I}_6}\right)\right) \tag{A.4}$$

in which the isochoric fiber potential $\bar{\Psi}^0_{\mathrm{F}}$ is assumed to be the sum of the contributions of two fiber families, i.e. $\bar{\Psi}^0_{\mathrm{F}} = \bar{\Psi}^0_{\mathrm{F4}} + \bar{\Psi}^0_{\mathrm{F6}}$. A push-forward operation on $\bar{\mathbf{S}}^0$ with $\bar{\mathbf{F}}$ to the current configuration results in the fictitious Cauchy stress tensor $\bar{\boldsymbol{\sigma}}$ defined as [34]

$$\bar{\boldsymbol{\sigma}}^0 = J^{-1}\bar{\mathbf{F}}\,\bar{\mathbf{S}}^0\,\bar{\mathbf{F}}^{\mathrm{T}} \tag{A.5}$$

The Cauchy stress should be decomposed into a volumetric and isochoric elastic response, i.e.

$$\boldsymbol{\sigma} = \boldsymbol{\sigma}_{\mathbf{iso}} + \boldsymbol{\sigma}_{\mathbf{vol}} \tag{A.6}$$

The isochoric and volumetric parts of the Cauchy stress is then determined as

$$\boldsymbol{\sigma}_{\mathbf{iso}} = \mathbb{P} : \bar{\boldsymbol{\sigma}}^0,\ \boldsymbol{\sigma}_{\mathbf{vol}} = p\mathbf{I} \tag{A.7}$$

where $\mathbb{P} = \mathbb{I} - \frac{1}{3}\mathbf{I}\otimes\mathbf{I}$ is the symmetric fourth-order Eulerian project tensor [34], and $\mathbb{I}$ is a fourth-order unit tensor with the components $(\mathbb{I})_{ijkl} = \frac{1}{2}(\delta_{ik}\delta_{jl}+\delta_{il}\delta_{jk})$. The constitutive equation for the hydrostatic pressure is given by $p = \partial \mathrm{U}_{\mathrm{vol}}/\partial J$. Replacing the Eq. (A.4) in (A.5) and then using the relations in (A.7), the total Cauchy stress defined in Eq. (A.6) can be constructed. The total Cauchy stress $\boldsymbol{\sigma}$ is then implemented in the user-defined interface UMAT.

A.3. Elasticity tensors

The linearized principle of virtual work constituents the starting point for approximation techniques such as the finite element method. In this method, the linearized principle of virtual work should be formulated in the Eulerian description [35]. Its derivation requires the calculation of the spatial elasticity tensor c in the Eulerian description. In addition, a consistent Jacobian matrix, which is referred to DDSDDE variable in UMAT user material subroutine, is needed as

$$\mathbb{D} = c + \mathbb{H},\ (\mathbb{H})_{ijkl} = \frac{1}{2}\left(\sigma_{ik}\delta_{jl} + \sigma_{jl}\delta_{ik} + \sigma_{il}\delta_{jk} + \sigma_{jk}\delta_{il}\right) \tag{A.8}$$

The consistent Jacobian matrix $\mathbb{D}$ has only 21 independent components at each strain state, i.e.

$$\mathbb{D} = \begin{bmatrix} D_{1111} & D_{1122} & D_{1133} & D_{1112} & D_{1113} & D_{1123} \\ D_{1122} & D_{2222} & D_{2233} & D_{2212} & D_{2213} & D_{2223} \\ D_{1133} & D_{2233} & D_{3333} & D_{3312} & D_{3313} & D_{3323} \\ D_{1112} & D_{2212} & D_{3312} & D_{12121} & D_{1213} & D_{1223} \\ D_{1113} & D_{2213} & D_{3313} & D_{1213} & D_{1313} & D_{1323} \\ D_{1123} & D_{2223} & D_{3323} & D_{1223} & D_{1323} & D_{2323} \end{bmatrix} \tag{A.9}$$

In the following the elasticity tensor c in the Eulerian description required for updating the DDSDDE is provided. For the purpose of computational implementation, it is more customary to decouple c into volumetric and isochoric elastic responses as

$$c = c_{iso} + c_{vol} \tag{A.10}$$

In addition to, the fictitious elasticity tensor in the Lagrangian description is needed that is defined as

$$(\bar{\mathbb{C}})^0 = 2J^{-4/3}\frac{\partial\bar{\mathbf{S}}^0}{\partial\bar{\mathbf{C}}} \tag{A.11}$$

The fictitious elasticity tensor in the Eulerian description $\bar{c}^0$ can be found from a push-forward operation of $\bar{\mathbb{C}}^0$ with $\mathbf{F}$, i.e.

$$\bar{c}^0 = 2\,\overline{\mathbf{F}\,\mathbf{F}}\,\frac{\partial\bar{\mathbf{S}}^0}{\partial\bar{\mathbf{C}}}\,\bar{\mathbf{F}}^{\mathbf{T}}\bar{\mathbf{F}}^{\mathbf{T}} \tag{A.12}$$

Finally, with Eqs. (A.5), $(A.7)_1$, and (A.12) the decoupled terms of the elasticity tensor c in the Eulerian description can be developed as [34]

$$c_{\mathrm{iso}} = J^{-1}(\mathbb{P}) :\ \bar{c}^0 :\ (\mathbb{P}) + \frac{2}{3}tr\left(\bar{\boldsymbol{\sigma}}^0\right)(\mathbb{P}) - \frac{2}{3}\left(\mathbf{I}\otimes\boldsymbol{\sigma}_{\mathbf{iso}} + \boldsymbol{\sigma}_{\mathbf{iso}}\otimes\mathbf{I}\right) \tag{A.13}$$

and

$$c_{\mathrm{vol}} = \left(p + \frac{\partial p}{\partial J}\right)(\mathbf{I}\otimes\mathbf{I}) - 2p(\mathbb{I}) \tag{A.14}$$

A.4. Verification

In this section, two representative examples are presented in order to illustrate the performance of the constitutive model through finite element implementation. The uniaxial extension and simple shear tests on a unit cube with dimension $1 \times 1 \times 1$ mm^3 are carried out. For verification of the model performance, the computational (FEM) and analytical solutions associated with both examples are compared. The model geometries are discretized with an 8-node hexahedral element (Abaqus element type C3D8). In the two aforementioned deformations, the cube consists of two families of fibers $\mathbf{M}$ and $\mathbf{N}$ that should be constructed in Cartesian basis vectors ($\mathbf{e}_1$, $\mathbf{e}_2$, $\mathbf{e}_3$).

In the first example, a unit cube composed of one element that consists of two families of fibers initially aligned along the unit vectors $\mathbf{M} = \cos\alpha\,\mathbf{e}_1 + \sin\alpha\,\mathbf{e}_2$ and $\mathbf{N} = \cos\beta\,\mathbf{e}_1 + \sin\beta\,\mathbf{e}_2$, $\alpha > 0$, $\beta < 0$, are subjected to uniaxial deformation, where its cross-section normal to $\mathbf{e}_3$ with loading direction aligned in $\mathbf{e}_1$ are shown in Fig. A.1. The deformation gradient in matrix form is given by $\mathbf{F} = \mathrm{diag}[\lambda_1,\lambda_2,\lambda_3]$. The incompressible counterpart of the Cauchy stress $\bar{\boldsymbol{\sigma}}^0$ (defined in Eq. (A.5)) is used for calculation of the stresses associated with the uniaxial deformation. For the uniaxial extension test, it is taken that $\sigma_{33} = 0$, by which the Lagrange multiplier p is calculated. In addition, the boundary condition shown in Fig. A.1 implies that $\sigma_{22} = 0$ while it shows σ_{11} is a non-zero component of the Cauchy stress. From the incompressibility condition, one obtains $\lambda_3 = \lambda_1^{-1}\lambda_2^{-1}$. Substituting the calculated amounts of p and λ_3 into the governing equations of σ_{11} and σ_{22} and considering that $\sigma_{22} = 0$ it leads to a system of nonlinear equations from which the relation between the stretches λ_1 and λ_2 can be found numerically. It is done using an Optimization package in Matlab. Then, with the experimental results taken from Table 2, the uniaxial Cauchy stress σ_{11} versus the stretch λ_1 is plotted in Fig. A.1 for a composite with $\alpha = 30$ and $\beta = -60$. Also shown in the figure are the computational and analytical solutions for the case in which the principal stretches λ_1 and λ_2 are evaluated. There are very good agreements between the computational (FEM) and analytical solutions. To evaluate a more general case, the Holzapfel-Gasser-Ogden (HGO) model [10] considering $k_1 = k_2$ is taken here for verification of the model, which is reduced to Ψ_{F} in Eq. (3) when $k_2 \approx 0$, as

$$\Psi_{\mathrm{F}} = \frac{k_1}{2k_2}\sum_{i=4,6}\left[\exp\left(k_2\left(I_i - 1\right)^2\right) - 1\right] \tag{A.15}$$

In the second example, as shown in Fig. A.2, the same unit cube is subjected to a simple shear deformation. The bottom nodes of the cube are fixed and then a shear deformation γ along $\mathbf{e}_1$ on the top nodes is applied. The deformation gradient is given by

$$\mathbf{F} = \begin{bmatrix} 1 & \gamma & 0 \\ 0 & 1 & 0 \\ 0 & 0 & 1 \end{bmatrix} \tag{A.16}$$

One possibility to determine the Lagrange multiplier p is to set $\sigma_{33} = 0$. The non-zero components of the Cauchy stress, i.e. two normal stresses σ_{11} and σ_{22} and the shear stress σ_{12}, can be easily found

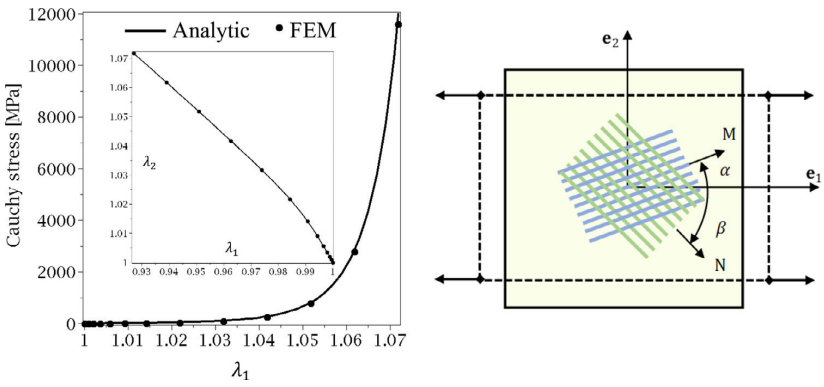

Fig. A.1. Comparison of the FEM results and the analytical solutions. The uniaxial extension of a unit cube in the $\mathbf{e}_1$ direction containing the two fiber families **M** and **N** with $\alpha = 30$ and $\beta = -60$. The solid line shows the undeformed and the dashed line shows the deformed configurations.

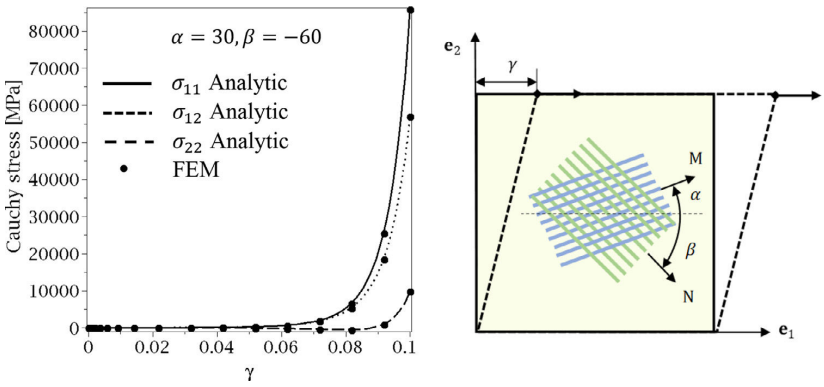

Fig A.2. Comparison of the FEM results and the analytical solutions. The simple shear deformation of a unit cube in the $\mathbf{e}_1$ direction with the amount of γ containing the two fiber families **M** and **N** with $\alpha = 30$ and $\beta = -60$. The solid line shows the undeformed and the dashed line shows the deformed configurations.

from the incompressible counterpart of the Cauchy stress $\bar{\boldsymbol{\sigma}}^0$. Note that the shear stress σ_{12} is independent of the p and the normal stress σ_{22} is independent of the matrix property. For the comparison, the analytical results (solid line) and computational solutions obtained by FEM are plotted in Fig. A.2 for a composite with $\alpha = 30$ and $\beta = -60$. Again, a very good agreement is observed between the two solutions.

References

[1] Rodriguez ED, Weed DC, Mather PT. Anisotropic Shape-Memory Elastomeric Composites: Fabrication and Testing. Macromol Chem Phys 2013;214(11):1247–57. doi:10.1002/macp.201300086.

[2] Shintake J, Cacucciolo V, Floreano D, Shea H. Soft robotic grippers. Adv Mater 2018:1707035.

[3] Chen Y, Wu B, Su Y, Chen W. Effects of strain stiffening and electrostriction on tunable elastic waves in compressible dielectric elastomer laminates. Int J Mech Sci 2020:105572.

[4] Milani AS, Nemes JA. An intelligent inverse method for characterization of textile reinforced thermoplastic composites using a hyperelastic constitutive model. Compos Sci Technol 2004;64(10–11):1565–76.

[5] Merodio J, Saccomandi G. Remarks on cavity formation in fiber-reinforced incompressible non-linearly elastic solids. Eur J Mech-A/Solids 2006;25(5):778–92.

[6] Ren J, Zhou J, Yuan X. Instability analysis in pressurized three-layered fiber-reinforced anisotropic rubber tubes in torsion. Int J Eng Sci 2011;49(4):342–53.

[7] Chebbi E, Wali M, Dammak F. An anisotropic hyperelastic constitutive model for short glass fiber-reinforced polyamide. Int J Eng Sci 2016;106:262–72.

[8] Liu H, Holzapfel GA, Skallerud BH, Prot V. Anisotropic finite strain viscoelasticity: Constitutive modeling and finite element implementation. J Mech Phys Solids 2019;124:172–88.

[9] Connolly F, Wagner DA, Walsh CJ, Bertoldi K. Sew-free anisotropic textile composites for rapid design and manufacturing of soft wearable robots. Extreme Mech Lett 2019;27:52–8.

[10] Holzapfel GA, Gasser TC, Ogden RW. A new constitutive framework for arterial wall mechanics and a comparative study of material models. J Elasticity Phys Sci Solids 2000;61(1):1–48. doi:10.1023/A:1010835316564.

[11] Pandolfi A, Vasta M. Fiber distributed hyperelastic modeling of biological tissues. Mech Mater 2012;44:151–62.

[12] Murphy JG. Transversely isotropic biological, soft tissue must be modelled using both anisotropic invariants. Eur J Mech-A/Solids 2013;42:90–6.

[13] Tricerri P, Dedè L, Gambaruto A, Quarteroni A, Sequeira A. A numerical study of isotropic and anisotropic constitutive models with relevance to healthy and unhealthy cerebral arterial tissues. Int J Eng Sci 2016;101:126–55.

[14] Chaimoon K, Chindaprasirt P. An anisotropic hyperelastic model with an application to soft tissues. Eur J Mech-A/Solids 2019;78:103845.

[15] Wagner DR, Lotz JC. Theoretical model and experimental results for the nonlinear elastic behavior of human annulus fibrosus. J Orthop Res 2004;22(4):901–9.

[16] Peng XQ, Guo ZY, Moran B. An anisotropic hyperelastic constitutive model with fiber-matrix shear interaction for the human annulus fibrosus. J Appl Mech 2006;73(5):815–24.

[17] Peng X, Guo G, Zhao N. An anisotropic hyperelastic constitutive model with shear interaction for cord–rubber composites. Compos Sci Technol 2013;78:69–74.

[18] Guo ZY, Peng XQ, Moran B. A composites-based hyperelastic constitutive model for soft tissue with application to the human annulus fibrosus. J Mech Phys Solids 2006;54(9):1952–71.

[19] Mansouri MR, Fuchs PF, Criscione JC, Schrittesser B, Beter J. The contribution of mechanical interactions to the constitutive modeling of fiber-reinforced elastomers. Eur J Mech-A/Solids 2020:104081.

[20] Gong Y, Peng X, Yao Y, Guo Z. An anisotropic hyperelastic constitutive model for thermoplastic woven composite prepregs. Compos Sci Technol 2016;128:17–24.

[21] Gong Y, Yan D, Yao Y, Wei R, Hu H, Xu P, et al. An anisotropic hyperelastic constitutive model with tension–shear coupling for woven composite reinforcements. Int. J. Appl. Mech. 2017;9(06):1750083.

[22] Horgan CO, Murphy JG. A constitutive model for fibre-matrix interaction in fibre-reinforced hyperelastic materials. Appl Eng Sci 2020;2:100008.

[23] Ogden RW. Nonlinear elasticity with application to soft fibre-reinforced materials. In: Nonlinear mechanics of soft fibrous materials. Springer; 2015. p. 1–48.

[24] Criscione JC, Hunter WC. Kinematics and elasticity framework for materials with two fiber families. Continuum Mech Thermodyn 2003;15(6):613–28.

[25] Mansouri MR, Darijani H. Constitutive modeling of isotropic hyperelastic materials in an exponential framework using a self-contained approach. Int J Solids Struct 2014;51(25–26):4316–26. doi:10.1016/j.ijsolstr.2014.08.018.

[26] Mansouri MR, Darijani H, Baghani M. On the correlation of FEM and experiments for hyperelastic elastomers. Exp Mech 2017;57(2):195–206. doi:10.1007/s11340-016-0236-0.

[27] Drzal LT, Madhukar M. Fibre-matrix adhesion and its relationship to composite mechanical properties. J Mater Sci 1993;28(3):569–610.
[28] Beter J, Schrittesser B, Maroh B, Sarlin E, Fuchs PF, Pinter G. Comparison and impact of different fiber debond techniques on fiber reinforced flexible composites. Polymers 2020;12(2):472.
[29] Karger-Kocsis J, Mahmood H, Pegoretti A. Recent advances in fiber/matrix interphase engineering for polymer composites. Prog Mater Sci 2015;73:1–43.
[30] Mansouri Mohammad Reza. Quantifying matrix-fiber mechanical interactions in hyperelastic materials. Mendeley data V1; 2020. doi:1017632/k7bzmf6mn61.
[31] Cerda E, Mahadevan L. Geometry and physics of wrinkling. Phys Rev Lett 2003;90(7):74302.
[32] Iwasa T. Approximate estimation of wrinkle wavelength and maximum amplitude using a tension-field solution. Int J Solids Struct 2017;121:201–11.
[33] Ogden RW, Saccomandi G, Sgura I. Fitting hyperelastic models to experimental data. Comput Mech 2004;34(6):484–502.
[34] Holzapfel GA. Nonlinear solid mechanics: a continuum approach for engineering science. Meccanica 2002;37(4):489–90.
[35] Bonet J, Wood RD. Nonlinear continuum mechanics for finite element analysis. Cambridge University Press; 1997.

Composites Part B

Matrix–fiber interfacial debonding in soft materials: Modeling and microstructural evolution

--Manuscript Draft--

Manuscript Number:	JCOMB-D-21-05125
Article Type:	Full Length Article
Keywords:	A. Polymer-matrix composites (PMCs), B. Microstructures, C. Damage mechanics, D. Optical microscopy
Corresponding Author:	Mohammad Reza Mansouri Polymer Competence Center Leoben GmbH (PCCL) Leoben, Austria Austria
First Author:	Mohammad Reza Mansouri
Order of Authors:	Mohammad Reza Mansouri
	Peter Filipp Fuchs, Dr.
	Mostafa Baghani
	Clara Schuecker
Manuscript Region of Origin:	Europe
Abstract:	It is apparent from the literature that the matrix–fiber mechanical interaction, as a result of interfacial adhesive bonds at the interface, significantly contribute to the macroscopic constitutive response of hyperelastic fiber-reinforced materials. This study bridges the degradation of macroscopic mechanical properties to the microscopically visible matrix–fiber interfacial debonding for cyclically deformed soft composites. The present work is an initial attempt to model matrix–fiber interfacial debonding in the context of pseudoelasticity by evaluating inelastic phenomena such as discontinuous Mullins softening and residual strain due to matrix damage, fiber rupture, and matrix–fiber interfacial debonding. The pseudoelastic model is based on hyperelastic strain energy functions consisting of two damage variables for each matrix, fiber, and matrix–fiber mechanical interaction. Each material and damage parameter is characterized independently by performing a comprehensive set of monotonic loading and cyclic tensile tests, respectively. Furthermore, finite element analysis is implemented using a user-defined subroutine, and the computationally calculated results are compared with the experimental data.
Suggested Reviewers:	Thomas Antretter, PhD Professor, Montanuniversität Leoben: Montanuniversitat Leoben Thomas.Antretter@unileoben.ac.at
	Gerald Pinter, PhD Professor, Montanuniversität Leoben: Montanuniversitat Leoben gerald.pinter@unileoben.ac.at
Opposed Reviewers:	

Polymer Competence Center Leoben

We acknowledge that the work submitted to the *Composites Part B: Engineering* contains

- **Novelty:**
  - This work is an initial attempt to characterize the matrix-fiber interfacial debonding using optical microscopy in soft composites.
  - This work models matrix-fiber interfacial debonding based on the degradation of macroscopic mechanical properties.
  - This study bridges the degradation of macroscopic mechanical properties to the microscopically visible matrix–fiber interfacial debonding for cyclically deformed soft composites.

- **Significance for the research community**
  - This work signifies that the underlying mechanism contributing to the degradation of the mechanical response of fiber-reinforced elastomers (i.e., Mullins softening, and permanent deformations) is attributed to the matrix-fiber interfacial debonding not matrix or fibers. It is supported by macroscopic and microscopic experimental observations.

To the best of the authors' knowledge, the above-mentioned aspects of soft composites have been noted for the first time by the submitted work.

Yours Sincerely
M.R. Mansouri

Polymer Competence Center Leoben GmbH
Roseggerstraße 12, A-8700 Leoben
www.pccl.at

Tel: +43 3842 42962-0
Fax: +43 3842 42962-6
office@pccl.at

Firmenbuch: LG Leoben
FN 223698v
UID-Nr. ATU 54829208

Steiermärkische Sparkasse
IBAN AT41 2081 5000 4032 7439
BIC STSPAT2GXXX

Matrix–fiber interfacial debonding in soft materials: Modeling and microstructural evolution

M.R. Mansouri[a,1,*], P.F. Fuchs[a], M. Baghani[b], C. Schuecker[c]

[a] Polymer Competence Center Leoben GmbH, Leoben, Austria

[b] University of Tehran, College of Engineering, School of Mechanical Engineering, Tehran, Iran

[c] Department of Polymer Engineering and Science, Montanuniversitaet Leoben, Leoben, Austria

ABSTRACT

It is apparent from the literature that the matrix–fiber mechanical interaction, as a result of interfacial adhesive bonds at the interface, significantly contribute to the macroscopic constitutive response of hyperelastic fiber-reinforced materials. This study bridges the degradation of macroscopic mechanical properties to the microscopically visible matrix–fiber interfacial debonding for cyclically deformed soft composites. The present work is an initial attempt to model matrix–fiber interfacial debonding in the context of pseudoelasticity by evaluating inelastic phenomena such as discontinuous Mullins softening and residual strain due to matrix damage, fiber rupture, and matrix–fiber interfacial debonding. The pseudoelastic model is based on hyperelastic strain energy functions consisting of two damage variables for each matrix, fiber, and matrix–fiber mechanical interaction. Each material and damage parameter is characterized independently by performing a comprehensive set of monotonic loading and cyclic tensile tests, respectively. Furthermore, finite element analysis is implemented using a user-defined subroutine, and the computationally calculated results are compared with the experimental data.

[1] Mohammad Reza Mansouri
Tel.: (43) 384242962-713
E-mail: mohammad.mansouri@pccl.at

Keywords:

A. Polymer–matrix composites (PMCs), B. Microstructures, C. Damage mechanics, D. Optical microscopy.

1. Introduction

Intriguing microscopic-defect-induced inelastic behaviors such as Mullins softening and irreversible permanent strain have not yet been investigated satisfactorily for individual composite phases in hyperelastic fiber-reinforced composites. In addition, debonding between constituent materials; that is, matrix–fiber interfacial/interphasal debonding, intensifies such inelastic behaviors of fibrous materials. However, there is no clear understanding of the extent to which damage in fiber-reinforced materials stems from the individual contributions of the matrix, fibers, and matrix–fiber debonding. In addition, the distinct contribution of matrix–fiber debonding to the degradation of the mechanical properties of fiber-reinforced materials has not yet been satisfactorily addressed in the literature. Although the responses of various hyperelastic fiber-reinforced materials have been modeled using a decoupled representation by assuming separate contributions of individual constituents, determining the actual mechanical contributions of the individual constituents is challenging, as reflected in the immense variety of the proposed models. In addition to constitutive modeling, it is crucial to characterize individual material constituents because their individual contributions to the overall material response might be confounded. Therefore, as a starting point for elucidating the features involved in the overall material response, both the molecular topology of the individual constituents and their respective damage mechanisms must be investigated.

Flexible composites consist of at least an elastomeric matrix, fibers, and a recognizable interphase [1,2] or a zero-thickness interface, as shown in Fig.1. The matrix–fiber interface/interphase, which is referred to as an adhesion bond, guarantees the stress transfer from the soft matrix to the stiff fiber and is the key factor determining the composite performance [1,3–5]. The chemically formed adhesion bonds directly influence the mechanical interactions between the matrix and the fibers such that weak adhesion bonds result in early matrix–fiber debonding [6] and, therefore, the matrix–fiber mechanical interactions contribute less to the overall composite performance [7,8].

Elastomers are another material phase featuring polymer chains, an entangled polymer-chain network, and covalent cross linkages and can be imagined as shown in Fig 1. Although the causes of physical damage in elastomers remain controversial, many studies have reported that under finite deformations, damage could be attributed to chain breakdown [9–12], covalent-crosslink breakage [13–15], and chain disentanglement [16]. In fiber-reinforced materials, a fiber usually consists of a bundle of filaments, as shown in Fig. 1. Although a single filament cannot bear high applied loads, a fiber bundle can. Because constituents often exhibit considerably different stiffnesses, flexible fiber-reinforced materials usually do not sufficiently deform in the fiber direction, and functionality (such as exceptional and multidirectional flexibilities, which are highly desirable for flexible fiber-reinforced composites [17]) is achieved when composites are loaded in directions different from the fiber orientation. Therefore, it is expected that within the *operating limits* of flexible composites, damage is more likely to occur in the soft matrix and/or at the matrix–fiber interface rather than among the fibers. Nevertheless, fiber-damage-induced inelastic behavior should be considered in constitutive modeling after its probability has been experimentally identified.

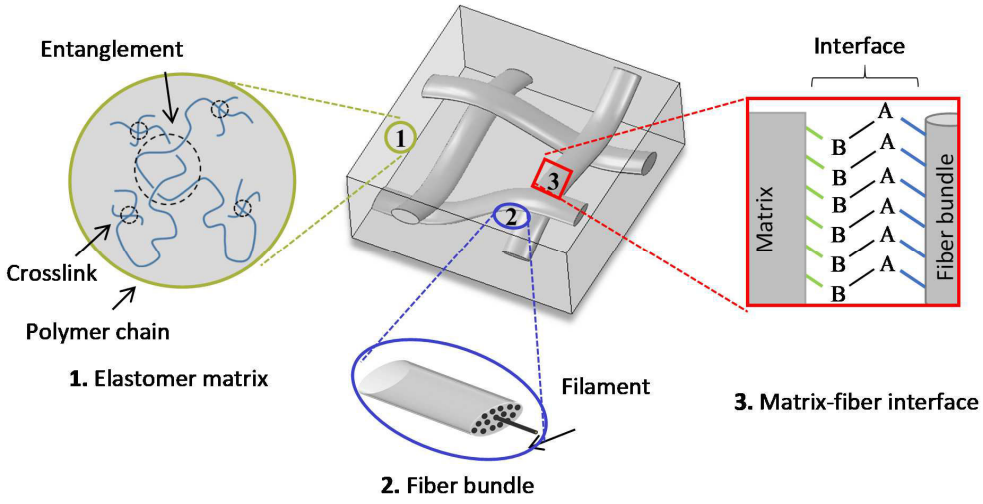

Fig. 1. Three phases of fiber-reinforced material: Molecular topologies of elastomer matrix, fiber bundle composed of single filaments, and matrix–fiber interface.

Damage models developed to account for damage-induced inelastic phenomena can be roughly categorized as continuum damage mechanics (CDM) and pseudoelasticity based. (For an overview of the pseudoelasticity method, please refer to [18] and [19].) Although CDM and pseudoelasticity approches are able to model the separate contributions of damage originating from the matrix, fibers, and interfaces, this alone is insufficient to model damage in hyperelastic fiber-reinforced materials. Compared to CDM-based models, pseudoelasticity ones can be formulated such that material parameters can be calibrated using the experimental data independently of damage parameters [20,21]. Unlike pseudoelastic models, CDM combined with hyperelasticity cannot distinguish the contribution of the stress softening and permanent strain to the damage in fiber-reinforced materials because both share the same damage parameters, which has not been previously pointed out in the literature. Furthermore, material calibration is more difficult using CDM models than using pseudoelastic ones [22], and CDM does not satisfactorily reproduce the

Mullins softening in hyperelastic materials showing highly reduced stiffness owing to inelastic dissipation [23], which is common in elastomers [24,25]. This issue has already been pointed out in [26–29]. Therefore, the works supporting pseudoelasticity approaches are reviewed here, emphasizing their ability to account for the distinct contributions of the matrix damage, fiber rupture, and matrix–fiber debonding by reproducing inelastic behaviors such as Mullins softening and permanent strain.

An alternative pseudoelasticity-based approach was introduced in Ref. [30] in which materials are treated as elastic during loading while showing inelastic behavior during unloading to model inelastic damage attributes in fiber-reinforced materials. This approach was extended by [19] to model the Mullins softening in filled rubbers and was further developed by [18] to model the Mullins softening and permanent strain in particle-reinforced rubbers. A pseudoelastic model for soft tissues was presented in [26] that incorporated stress softening in both the isotropic ground matrix and fibers without considering the permanent strain. A model was developed by [20] to describe Mullins softening in aortic layers loaded beyond the physiological range. However, the permanent strain observed in the experimental results was not considered. This work was extended by [31] to account for Mullins softening and permanent strain in arterial tissues. Their damage model assumed that Mullins softening occurred only in collagen fibers, while both the matrix and fibers contributed simultaneously to the permanent strain. Recently, the work presented in Ref. [32] studied Mullins softening in short fibers and soft composites within the pseudoelasticity framework by considering damage to both the matrix and fibers. However, unlike the experimental observations, the modeling did not account for permanent strain. They assumed that matrix–fiber debonding contributed to the matrix damage term owing to void nucleation at bonding sites and further evaluated their model against the cyclic uniaxial extension of specimens in which fibers were oriented parallel to the loading direction.

To the best of our knowledge, inelastic damage attributes such as Mullins softening and permanent strain as a result of the matrix-fiber debonding have not yet been modeled—as reflected in proposed models wherein the individual contributions of only the matrix and fibers have been determined, while matrix–fiber debonding would be associated with a third material phase called the "matrix–fiber interface/interphase" (see Fig. 1) consisting of neither the matrix nor fibers. Furthermore, although pseudoelasticity is a method wherein material and damage parameters can be obtained independently, employing a relevant constitutive model that accounts for distinct contributions of composite material phases is pivotal with this approach. The present work aims to determine inelastic damage attributes due to matrix damage, fiber rupture, and matrix–fiber interfacial debonding in the context of the pseudoelasticity theory to elucidate the extent of the damage stemming from any of the particular material phases in fiber-reinforced elastomers

2. Experimental

2.1. Materials and methods

Fiber-reinforced composites consisting of a polydimethylsiloxane (PDMS) matrix and endless twill woven glass fiber (GF) reinforcement are manufactured using vacuum-assisted resin infusion (VARI) at 20 mbar. The PDMS is an addition–curing two-component system exhibiting a hardness of 35 Shore A, a density of 1.02 g/cm^3, a noncured viscosity of 3500 mPa·s, and a pot life of approximately 90 min at room temperature. Two layers of woven fabric are placed in a mold and then exposed to a matrix flow. The impregnated composite is cured at $70\,^{\circ}\mathrm{C}$ for 1 h in a temperature chamber. Composite samples with exhibiting an aspect ratio of $\xi = 3/\tan\alpha$ with two fiber families initially aligned in the $\mathbf{M} = \cos\alpha\,\mathbf{e}_1 + \sin\alpha\,\mathbf{e}_2$ and $\mathbf{N} = \cos\beta\,\mathbf{e}_1 + \sin\beta\,\mathbf{e}_2$ directions, where $\alpha > 0$ and $\beta < 0$, were considered. A fixed

coordinate system $\{\mathbf{e}_1, \mathbf{e}_2, \mathbf{e}_3\}$ is applied to specify the loading in the $\mathbf{e}_1$ direction. Then, composites exhibiting a preferred fiber orientation represented by $[+\alpha/-\beta]$, such as [+45/−45] and [+30/−60], are prepared with a thickness of $t = 0.4\,mm$. The aspect ratio of the samples is defined such that $\mathrm{L} = 3a/\tan\alpha$ denoted the length of samples between the clamps, and a is the width of the samples. Using this sample geometry, at least one end of each fiber is free (i.e., was not clamped in the fixture); therefore, no clamping effects had to be considered. The importance of the sample geometry is highlighted in a combined experimental and numerical study [8]. Composites exhibiting a fiber orientation of [+0/−90] are prepared in dimensions of 30×90 (a (mm) × L (mm)). The matrix material is manufactured according to the ISO 37 standard with type 2 specimens.

Cyclic tensile tests are performed on the composites with preferred fiber orientations [+45/−45], [+30/−60], and [+0/−90] in the $\mathbf{e}_1$ direction. Stretches associated with the composites are recorded based on the machine crosshead displacement. Cyclic uniaxial tensile tests are also carried out on a pure matrix, and stretches are measured using the digital image correlation (DIC) method by monitoring two points with a $20\ \mathrm{mm}$ distance marked in the middle of the sample (For a detailed explanation of the characterization method of isotropic hyperelastic elastomers, please refer to [33]). All the tests are conducted at a crosshead velocity of 5 mm/min, where viscoelastic effects are negligible under standard atmospheric conditions. The tests are performed using a universal testing machine (Z250, ZwickRoell GmbH & Co. KG). The composites are clamped using a pneumatic grip at 6 bar. To capture the stretch deformation fields of the composite, 3D full-field high-resolution images are captured using the DIC method (with a DIC system consisting of a Mercury BLFY 050 camera and Mercury RT software, Czech Republic) for the composite prepared with fibers oriented at [+45/−45] during the cyclic tensile test in the

$\mathbf{e}_1$ direction and for a spray pattern on the specimen surface suitable for the high elasticity of the matrix material.

In-situ optical microscale tests are performed on composites prepared with fibers oriented at $[+45/-45]$, at approximately the length scale of the fibers, to understand the relationship between the macroscale observations and the microstructural damage evolutions. The samples are placed in a custom-designed *in-situ* tensile test device and are stretched to 1.3 times their initial length while they are observed under an optical microscope (Alicona InfiniteFocusG5 Plus, Austria) equipped with a 100× magnification objective lens. The transparency of the PDMS matrix enabled the interior material structure to be clearly observed during deformation. Vertical Focus Probing Technology (VFPT) enables samples to be vertically scanned to provide images at different depths and 10-nm vertical resolution. Matrix–fiber debonding is characterized using the micrographs obtained by capturing images at five vertical sample depths.

2.2. Cyclic stress–stretch responses

To assess the influence of the stress softening and accumulated residual strain on the stretch response, several series of loading–unloading–reloading tensile tests are conducted on fiber-reinforced elastomers at specific stretches. A displacement control protocol is employed for the cyclic tensile testing of the matrix, fibers, and composites prepared with fibers oriented at $[+45/-45]$ and $[+30/-60]$. For the composites, cyclic unloading are conducted at 0.05 uniaxial stretch increments. The relevant cyclic stress–stretch results corresponding to the loading–unloading up to a stretch of $\lambda_1 = 1.30$ and $\lambda_1 = 1.25$ are provided in Fig. 2(a) and (b) for the composites prepared with fibers oriented at $[+45/-45]$ and $[+30/-60]$, respectively. Note that Fig. 2 shows significant Mullins softening and irreversible residual stretch for the composites

exhibiting different material anisotropies, which both become more pronounced with increasing maximum stretch. The figure also indicates that the Mullins softening is not ideal because the unloading and reloading responses differ. This divergence of the unloading and reloading responses has been observed previously in other reinforced soft materials such as filled rubbers [34], fiber-reinforced elastomers [32,35,36], elastomeric nanocomposites [37], and fibrous tissues [20]. Ideally, the reloading and loading responses coincide [11].

The same protocol is applied to tests on pure matrix specimens for loading–unloading cycles up to a stretch of $\lambda_1 = 1.30$. The cyclic stress–stretch responses of the fibers are characterized using a composite prepared with fibers oriented at $[+0/-90]$ and stretched at three evenly spaced intervals up to $\lambda_1 = 1.015$. The stress–stretch results corresponding to the last cycle are plotted in Fig. 3 for the matrix, fibers, and composites prepared with fibers oriented at $[+45/-45]$ and $[+30/-60]$. Clearly, the pure matrix and the 0/90 "fiber" specimen both exhibited negligible Mullins softening and permanent strain. Therefore, the damage accumulation in the composite cannot be attributed to the damage evolution in the matrix or fibers.

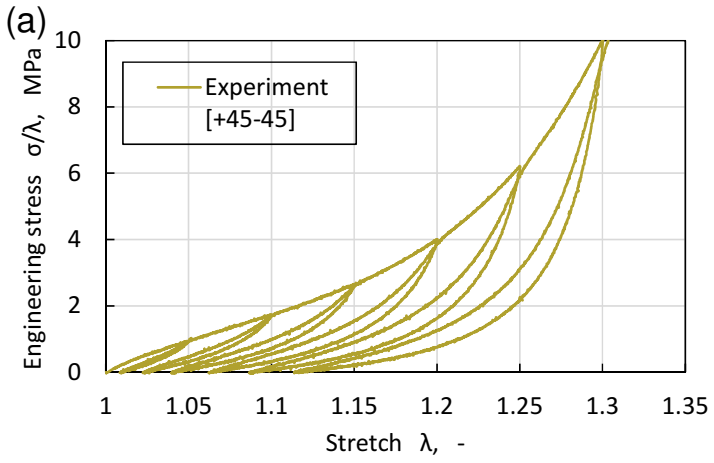

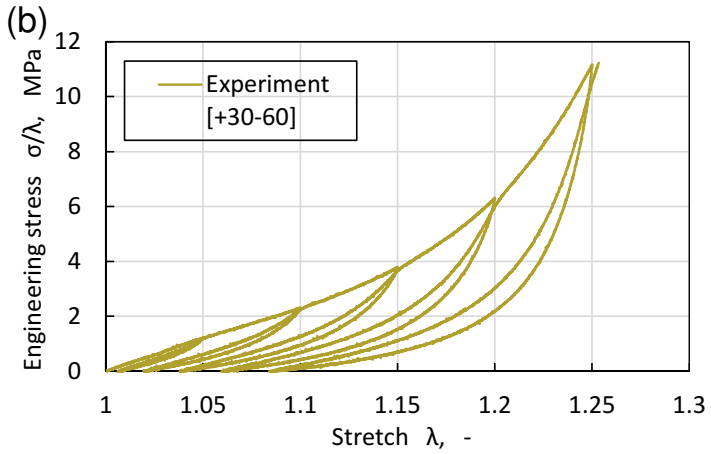

Fig. 2. Cyclic stress–stretch responses featuring Mullins softening and permanent strain of composites prepared with fibers oriented at (a) [+45/−45] and (b) [+30/−60] and subjected to tensile tests in $\boldsymbol{e}_1$ direction.

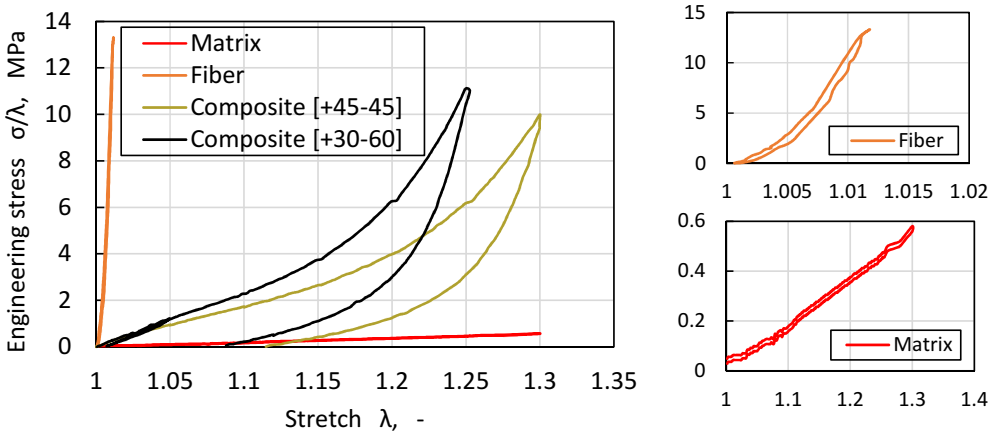

Fig. 3. Cyclic stress–stretch responses of matrix and fibers during cyclic tensile tests. Comparative experimental illustrations of highest damage accumulated during entire deformation history for matrix, fibers, and composites during cyclic tensile tests.

2.3. In-situ microstructural characterizations

Micromechanical damage to hyperelastic fiber-reinforced materials remains unclear. According to the literature, damage evolution is due to the degradation of the mechanical constituents of fiber-reinforced

materials, as reflected in models wherein damage evolution is only attributed to constituent materials (i.e., matrix and fibers). Nevertheless, because mechanical property degradation indicates microstructural changes, the cyclic stress–stretch responses shown in Fig. 3 suggest that such changes are irrelevant for the matrix and fibers. Therefore, it seems reasonable to determine the damage evolution mechanism for other material phases of fiber-reinforced composites, the most relevant of which might be due to matrix–fiber interfacial debonding. However, there is a lack of experimental observations to bridge the gap between the degradation of the composite mechanical properties (quantified based on cyclic stress–stretch responses) and matrix–fiber interfacial debonding, which might be microscopically visible.

To bridge this gap, the probability of matrix–fiber interfacial debonding is first evaluated using *in-situ* optical microscopy. Therefore, different selected composite areas (see Fig. 4a, Fig. 5, and Fig. 6) exhibiting fibers oriented at $[+45/-45]$ are chosen, and the specimens are then stretched to characterize the microstructure *in situ*. Simultaneously, local matrix–fiber debonding is captured by taking high-resolution images at five different vertical sample depths. As shown in Fig. 4b, the image includes the top outer surface of the sample (Z_0), top of the first observed fiber (Z_1), middle of the same fiber (Z_2), top of the fiber in the second layer (Z_3), and middle of the same fiber (Z_4). The composite transparency allows the microscope to scan through the entire thickness of the samples, thereby enabling a full-field analysis of matrix–fiber debonding. The micrographs captured from different vertical sample depths are depicted in Fig. 4, Fig. ***5***, and Fig. ***6*** for the nondeformed sample and the counterparts deformed up to a stretch of $\lambda_1 = 1.30$.

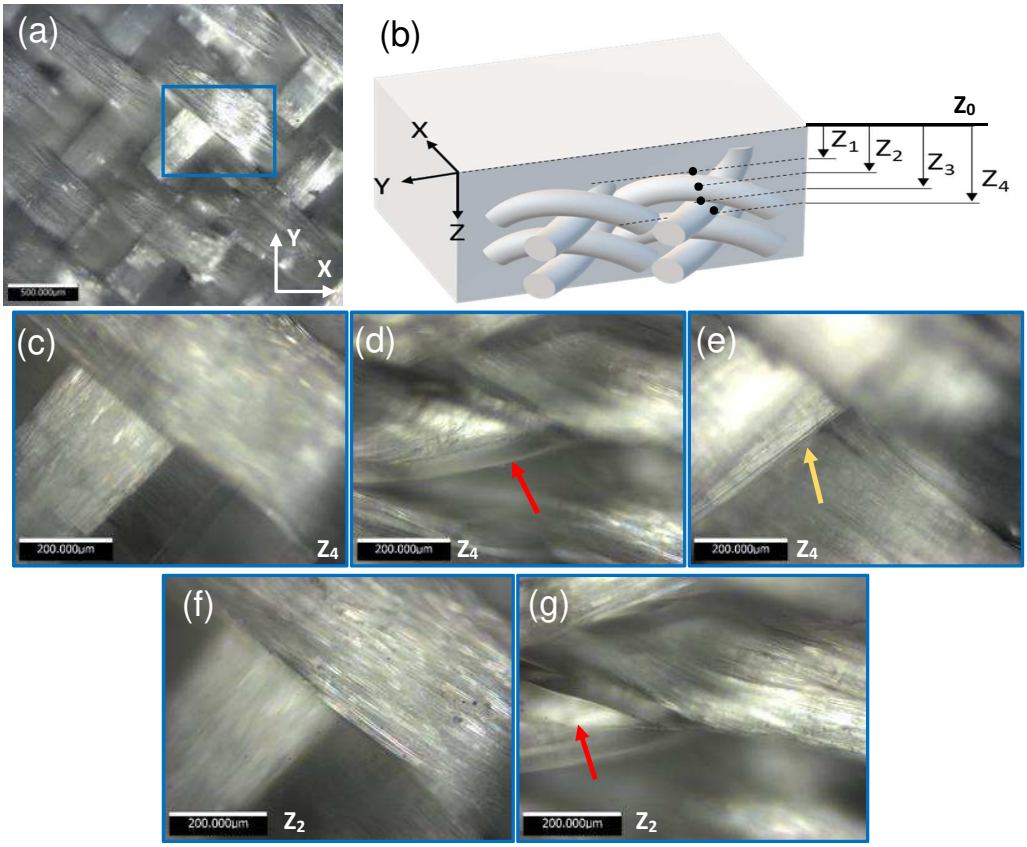

Fig. 4. Matrix–fiber interfacial debonding illustrated for two families of fibers: (a) representative region in nondeformed sample; (b) vertical positions of fibers at different depths (c); micrograph of blue region shown in (a) at vertical depth of Z_4; (d) micrograph corresponding to panel (c) in deformed specimen, featuring local matrix–fiber debonding; and (e) disappearance of matrix–fiber debonding when sample is unloaded. (f) Micrograph of blue region in figure (a) shown for depth Z_2, and (g) respective matrix–fiber debonding in deformed specimen.

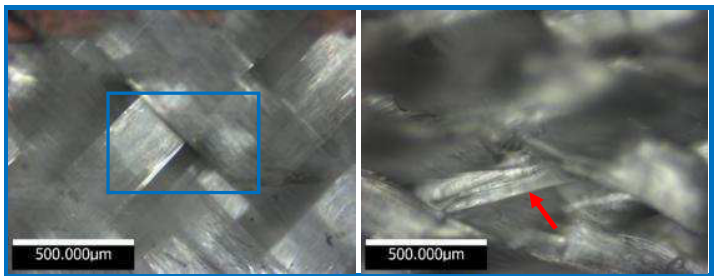

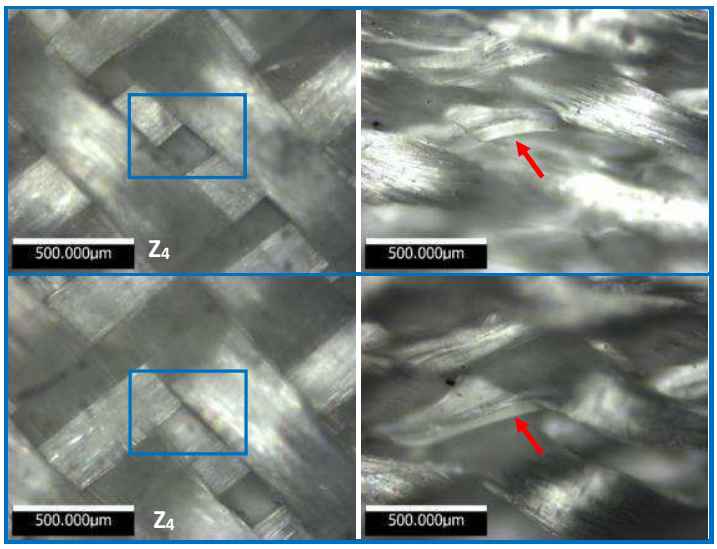

Fig. 5. Chosen micrographs captured from different regions of nondeformed sample, shown in blue boxes (left); and corresponding images captured when sample is stretched up to 1.3 times its initial length, featuring local matrix–fiber interfacial debonding indicated by red arrows (right).

The micrographs indicate different microstructural damage evolutions during deformation: (i) Continuous matrix–fiber debonding is observed in the vicinity of two families of fibers in Fig. 4(d) and (g), while corresponding nondeformed specimens are shown in Fig. 4(c) and (f), respectively. Notably, matrix–fiber debonding is barely visible when the sample is unloaded (see Fig. 4(e)). Because the material is flexible, it tends to return to its initial state, while permanent matrix–fiber debonding remains. Therefore, *in-situ* tests are necessary to characterize matrix–fiber debonding in fiber-reinforced soft composites. Further illustrations of matrix–fiber interfacial debonding are provided in Fig. 5 as taken from different areas of the samples. (ii) Discontinuous matrix–fiber debonding is observed between the outer surface of the sample and the middle of the first observed fiber (i.e., $Z_0<Z<Z_2$), as shown in Fig. 6. Although this type of damage is special, it is frequently observed during optical imaging. Local pointwise matrix–fiber debonding starts

in the top vicinity of the fibers and continues vertically up to the middle of the fiber while dispersing horizontally into the matrix. Because portions of the material appear to have been scraped away, we call this class of damage "carving," which has not been observed previously. We chose to monitor top views (Z_0) of three areas on the composite surface, as shown in Fig. 6(a). The corresponding local damage evolutions are apparent in Fig. 6(b) between the vertical depths $Z_0<Z<Z_2$. As shown in Fig. 6(c), the carving disappears and is barely visible in the middle of the fiber (Z_2). Both microstructural evolutions, appearing as matrix–fiber debonding, are reported herein as the underlying mechanism generating the Mullins softening and permanent strain observed in the typical stress–stretch responses of the fiber-reinforced composites (see Fig. 3).

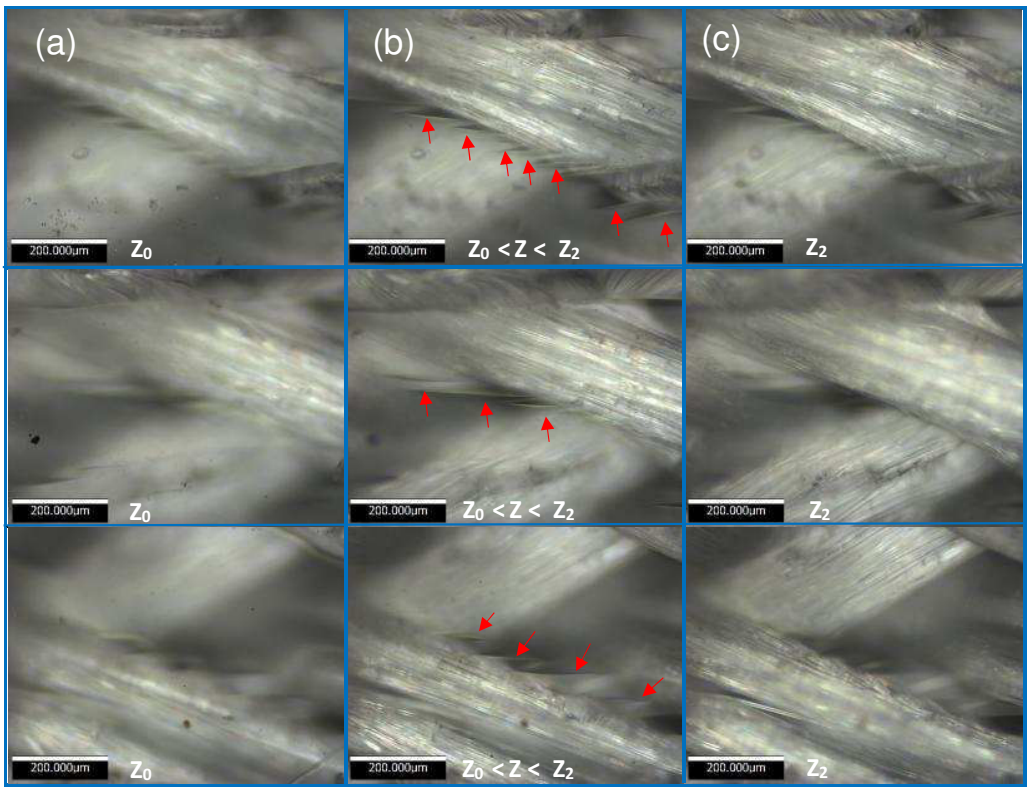

Fig. 6. Pointwise matrix–fiber debonding shown for chosen regions of stretched sample: (a) micrographs taken from top view of surfaces of three regions; (b) representative pointwise matrix–fiber debonding corresponding to regions shown in panel (a) taken at vertical depth between top surface of sample (Z_0) and middle of first observed fiber (Z_2), as indicated by red arrows; and (c) disappearing, barely visible pointwise debonding observed in panel (b) at depth of Z_2.

2.4. 3D full-field stretch analysis

The significant Mullins softening and permanent strain observed in the cyclic deformations shown in Fig. 2 are indicative of damage evolutions in the material microstructure, which is locally observable. Because damage should manifest in the stretch maps on the outer surface of the samples, 3D full-field high-resolution images are captured using the DIC method for the composite prepared with fibers oriented at $[+45/-45]$ during the cyclic tensile test in the $\mathbf{e}_1$ direction, as explained in Section 2.2. Because the deformation was symmetric, we monitored the blue region depicted in Fig. 7(a). Representative cyclic stress–stretch responses are shown in Fig. 7(b), indicating that for each cycle, the maximum stretch (λ_1, $\lambda_3, \lambda_5, \lambda_7, \lambda_9, \lambda_{11}, \lambda_{13}$) and respective residual stretch ($\lambda_2, \lambda_4, \lambda_6, \lambda_8, \lambda_{10}, \lambda_{12}, \lambda_{14}$) were achieved. The local stretch maps corresponding to the stretch values are indicated in Fig. 7(c) and (d), showing inhomogeneous deformations at the maximum stretches and permanent strains after the specimens were unloaded, respectively. Movies of the stretch maps generated during the cyclic tensile tests are provided in the supplementary materials [38].

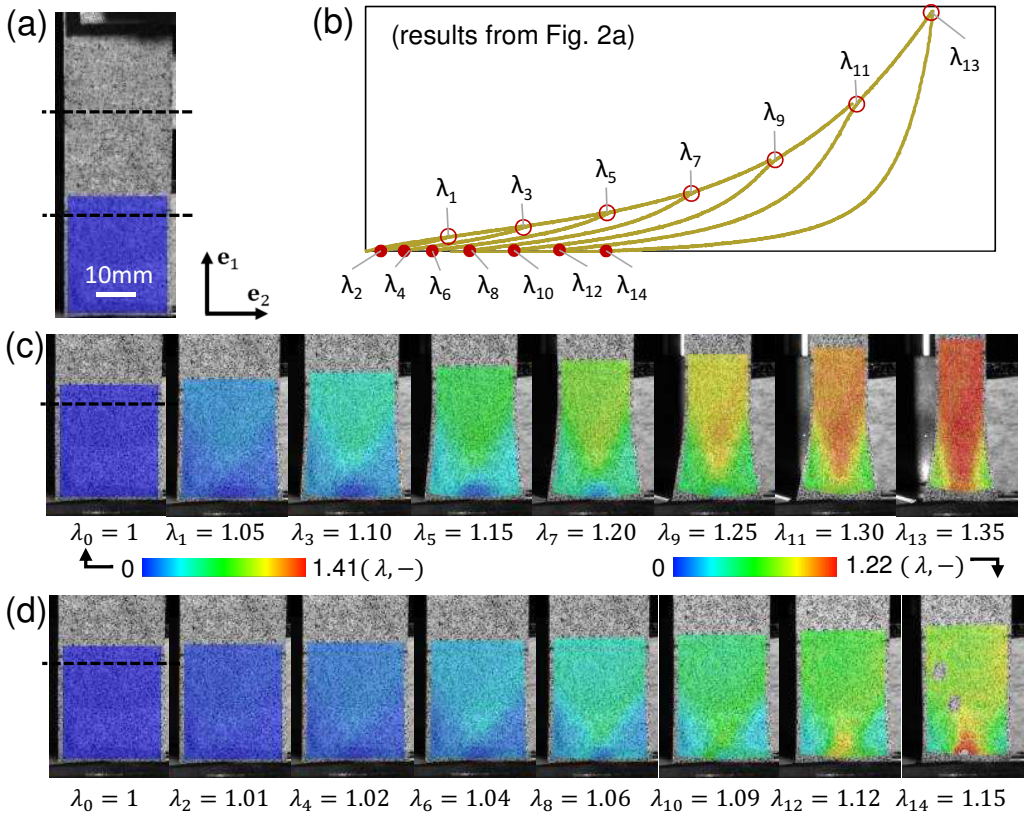

Fig. 7. 3D full-field stretch maps captured by DIC for composite prepared with fibers oriented at [+45/−45] and subjected to cyclic tensile tests in $\boldsymbol{e}_1$ direction: (a) nondeformed composite showing blue region used to monitor stretch maps; (b) representative stress–stretch plot generated for sample; (c) inhomogeneous stretch maps corresponding to highest stretches (shown in panel (b)) obtained during each cycle; (d) inhomogeneous evolution of damage reflected in residual stretches in unloaded composite.

3. Modeling

3.1. A matrix-fiber-interaction model based on general invariants

To model the elastic part of the deformation, a unified invariant-based constitutive model proposed by [39] and its continuum mechanical framework are described owing to some necessary changes in notation.

Consider continuum body $\mathfrak{B}_r$ in the reference configuration of a material body. It is assumed that any material point is labeled by its position vector $\mathbf{X}$ in $\mathfrak{B}_r$. Let the body be deformed into a new configuration ($\mathfrak{B}$) such that material point $\mathbf{X}$ takes up position $\mathbf{x}$. This motion was introduced by mapping $\mathbf{x} = \boldsymbol{\chi}(\mathbf{X})$. The gradient of $\boldsymbol{\chi}$ is defined by $\mathbf{F}(\mathbf{X}) = \mathrm{Grad}\,\mathbf{x}$ and is referred to as the deformation gradient tensor, and its determinant $J = \det \mathbf{F}(\mathbf{X}) > 0$ is called the local volume ratio. The right Cauchy–Green strain tensor is given by $\mathbf{C} = \mathbf{F}^{\mathrm{T}}\mathbf{F}$ with the corresponding first and second invariants as

$$I_1 = \mathrm{tr}\,\mathbf{C} \quad \text{and} \quad I_2 = \frac{1}{2}[(\mathrm{tr}\mathbf{C})^2 - \mathrm{tr}(\mathbf{C}^2)]. \tag{1}$$

Let $\mathbf{M} = \cos\theta\ \mathbf{E}_1 + \sin\theta\ \mathbf{E}_2$ and $\mathbf{N} = \cos\theta\ \mathbf{E}_1 - \sin\theta\ \mathbf{E}_2$ be unit vectors oriented in the directions of the fibers in the reference configurations, where $\mathbf{E}_1$ and $\mathbf{E}_2$ denote the Cartesian coordinate system. Parameter θ is one-half the angle subtended by $\mathbf{M}$ and $\mathbf{N}$, which are mapped to spatial line elements $\mathbf{m}$ and $\mathbf{n}$ in the deformed configuration by deformation gradient $\mathbf{F}$ through motion $\mathbf{x} = \chi(\mathbf{X})$. During this deformation, the material line elements might experience a change in both the element length and angle. The following invariants for fiber-reinforced materials were introduced [40]:

$$I_4(\mathbf{M}) = \mathbf{C} : \mathbf{M} \otimes \mathbf{M}, \qquad I_6(\mathbf{N}) = \mathbf{C} : \mathbf{N} \otimes \mathbf{N}, \qquad I_8(\mathbf{M}, \mathbf{N}) = \mathbf{C} : \mathbf{M} \otimes \mathbf{N}. \tag{2}$$

Pseudoinvariants I_4 and I_6 capture information about the square of the stretch in fiber directions $\mathbf{M}$ and $\mathbf{N}$, respectively. In their original work, Ref. [41] introduced a scalar ($\mathcal{B}$) representing the change in the angle between equally deformed fibers and found the following relation between $\mathcal{B}$, the angle between the deformed fibers (denoted here by φ), and the right-hand side of the relations defined in (2):

$$\cos\varphi = \frac{\mathbf{C} : \mathbf{M} \otimes \mathbf{N}}{\sqrt{\mathbf{C} : \mathbf{M} \otimes \mathbf{M}}\sqrt{\mathbf{C} : \mathbf{N} \otimes \mathbf{N}}} = \frac{\mathcal{B}^2\cos^2\theta - \mathcal{B}^{-2}\sin^2\theta}{\mathcal{B}^2\cos^2\theta + \mathcal{B}^{-2}\sin^2\theta} \tag{3}$$

By substituting the relations given in (2) into equation (3), [39] obtained an angular-based invariant expressed in terms of strain invariants $I_8^* = I_8/\sqrt{I_4\, I_6} = \cos\varphi$ to consider the current angle between deformed fibers.

For computational implementation, the proposed model is treated as a nearly incompressible material. Hence, deformation gradient $\mathbf{F}$ and corresponding strain measure $\mathbf{C}$ are multiplicatively decomposed into volume-changing (volumetric) and volume-preserving (isochoric) parts as $\mathbf{F} = J^{1/3}\overline{\mathbf{F}}$ and $\mathbf{C} = J^{2/3}\overline{\mathbf{C}}$, respectively. Because $\mathbf{F}$ is decoupled, it is assumed that the total potential function (Ψ) can be described in terms of an energy contribution ($\mathrm{U_{vol}}(J)$) dependent only on J; that is, a purely volumetric contribution, and contribution $\overline{\Psi}^0(\overline{\mathbf{C}}, \{\mathbf{M}, \mathbf{N}\})$ obtained from the isochoric deformation through $\overline{\mathbf{C}}$. Thus,

$$\Psi(\mathbf{C}, \{\mathbf{M}, \mathbf{N}\}) = \overline{\Psi}^0(\overline{\mathbf{C}}, \{\mathbf{M}, \mathbf{N}\}) + \mathrm{U_{vol}}(J). \tag{4}$$

Extensional-based invariants I_4 and I_6 and angular-based invariant I_8^* are employed by the fibers' and the matrix–fiber mechanical interactions' potentials, respectively, to form a unified invariant-based Matrix–Fiber–Interaction (MFI) model [42] wherein an isochoric potential function ($\overline{\Psi}^0$) is defined as follows:

$$\overline{\Psi}^0(\overline{\mathbf{C}}, \{\mathbf{M}, \mathbf{N}\}) = \overline{\Psi}_{\mathrm{M}}^0(\bar{I}_1) + \overline{\Psi}_{\mathrm{F}}^0(\bar{I}_4, \bar{I}_6) + \overline{\Psi}_{\tau}^0(\bar{I}_8^*), \tag{5}$$

where $\overline{\Psi}_{\mathrm{M}}^0$, $\overline{\Psi}_{\mathrm{F}}^0$, and $\overline{\Psi}_{\tau}^0$ introduce the isochoric potentials associated with the matrix, fibers, and matrix–fiber mechanical interactions, respectively, and isochoric invariants $\bar{I}_1 = J^{-2/3}I_1$, $\bar{I}_i = J^{-2/3}I_i$, $i = \{4, 6, 8\}$, and $\bar{I}_8^* = I_8^*$.

Remark 3.1. A so-called invariant (I_8) $= \mathbf{C} : \mathbf{M} \otimes \mathbf{N}$ was introduced in [40] to model composites exhibiting two fiber families. This invariant appears to have attracted negligible attention until [43] introduced I_8 as a "coupling" term to model fiber-reinforced nonlinear elastic solids. Since then, this

invariant has been an alternative used to constitutively model the contribution of matrix–fiber mechanical interactions (see, for example, [44–51].

3.2. Inelastic damage model

The pseudoelasticity approach enables us to distinguish between Mullins softening and permanent strain. Moreover, it allows distinct contributions from any constituent materials to both Mullins softening and permanent strain to be considered. In this work, two damage variables—and, therefore, two dissipation functions—corresponding to Mullins softening and permanent strain are assigned to each material phase including the matrix, two fiber families, and matrix–fiber interface. The pseudoelastic energy introduced by [18] for isotropic materials is accordingly modified for anisotropic ones to represent loading and unloading as follows:

$$\begin{aligned}\mathcal{W}(\bar{\mathbf{C}},\{\mathbf{M},\mathbf{N}\},\eta,\xi) &= \sum_{i=\mathrm{M,F},\tau}\Big(\Big[\eta_i\overline{\Psi}_i^0(\bar{\mathbf{C}},\{\mathbf{M},\mathbf{N}\})+\phi_i(\eta_i)\Big] \\ &\quad -\left[(1-\xi_i)\,N_i(\bar{\mathbf{C}}^N,\{\mathbf{M},\mathbf{N}\})+\rho_i(\xi_i)\right]\Big),\end{aligned} \tag{6}$$

where η_i and ξ_i, $i=\{\mathrm{M},\mathrm{F},\tau\}$ are variables used to capture the stress softening and permanent strain, respectively. Both variables depend on the previously achieved maximum strain [18]. In Eq. (6), $\phi_i(\eta_i)$ and $\rho_i(\xi_i)$ are dissipation functions that capture the energy dissipated in the material during loading–unloading cycles and are associated with softening and permanent strain, respectively. Inelastic energy dissipations N_i introduce permanent strain to the model, including the dependence on the maximum deformation to which the material had been subjected during the primary loading. It is defined as a function of the modified right Cauchy–Green tensor ($\bar{\mathbf{C}}^N$) obtained at the peak deformation of the loading history.

Remark 3.2. Unlike in equation (6), all the previously developed pseudoelastic models reported in the literature use a single damage variable for all the material constituents to capture the permanent strain (see, for example, [31]), which limits the determination of particular contributions from any of the constituents to the overall material damage.

Like the elastic contribution, an anisotropic dissipation function (N) is assumed for the inelastic energy contribution and takes the same form as the decoupled elastic potential function introduced in equation (5). However, because N has different material parameters, it reflects anisotropy as follows:

$$N(\bar{\mathbf{C}}^N, \{\mathbf{M}, \mathbf{N}\}) = N_{\mathrm{M}}\left(\bar{I}_1^{\,N}\right) + N_{\mathrm{F}}\left(\bar{I}_4^{\,N}, \bar{I}_6^{\,N}\right) + N_{\tau}\left(\bar{I}_8^{*N}\right). \tag{7}$$

Note that we considered the inelastic energy dissipation (N) as a function of $\bar{\mathbf{C}}$ at the peak deformation of the loading history; that is, $\bar{\mathbf{C}}^N = \bar{\mathbf{C}}$ and structural parameters $\mathbf{M}$ and $\mathbf{N}$. Indeed, this function is only updated during unloading from the maximum deformation so that once the function is updated, its value remains constant during unloading and reloading. Therefore, from equations (1) and (2), the invariants given in equation (7) are defined as follows:

$$\bar{I}_1^{\,N} = \mathrm{tr}\bar{\mathbf{C}}^N,\ \bar{I}_4^{\,N} = \bar{\mathbf{C}}^N{:}\,\mathbf{M}\otimes\mathbf{M},\ \bar{I}_6^{\,N} = \bar{\mathbf{C}}^N{:}\,\mathbf{N}\otimes\mathbf{N},\ \bar{I}_8^{\,N} = \bar{\mathbf{C}}^N{:}\,\mathbf{M}\otimes\mathbf{N},\ \bar{I}_8^{*N} = \frac{\bar{I}_8^{\,N}}{\sqrt{\bar{I}_4^{\,N}\bar{I}_6^{\,N}}}. \tag{8}$$

During loading, it is assumed that $\eta = \xi = 1$ and, therefore, $\phi_i(\eta_i) = \rho_i(\xi_i) = 0$, which reduces equation (6) to equation (5), and the general finite elasticity is recovered.

From [52], it follows that at equilibrium in the absence of body forces

$$\frac{\partial \omega(\mathbf{F}, \delta)}{\partial \delta} = 0 \quad \text{in} \quad \mathfrak{B}_r, \tag{9}$$

where $\omega(\mathbf{F}, \delta)$ is the pseudoenergy function of the material, and δ is a damage variable. It is now convenient to specialize in Eq. (6) to account for more than one additional variable as follows:

$$\frac{\partial \mathcal{W}(\bar{\mathbf{C}}, \{\mathbf{M}, \mathbf{N}\}, \eta, \xi)}{\partial \eta} = 0, \quad \frac{\partial \mathcal{W}(\bar{\mathbf{C}}, \{\mathbf{M}, \mathbf{N}\}, \eta, \xi)}{\partial \xi} = 0, \tag{10}$$

according to [18]. From equation (10), the pseudoelastic energy in equation (6) gives

$$\overline{\Psi}_i^0 + \frac{\partial \phi_i}{\partial \eta_i} = 0, \quad N_i - \frac{\partial \rho_i}{\partial \xi_i} = 0. \tag{11}$$

3.3. Cauchy stress

We now present the total Cauchy stress tensor ($\boldsymbol{\sigma}$) decomposed into volumetric and isochoric pseudoelastic (which is no longer elastic) responses as follows:

$$\boldsymbol{\sigma} = \boldsymbol{\sigma}_{\text{iso}} + \boldsymbol{\sigma}_{\text{vol}}. \tag{12}$$

The isochoric Cauchy stress associated with the pseudoelastic energy defined in Eq. (6) can be written as

$$\boldsymbol{\sigma}_{\text{iso}} = 2J^{-1}\mathbf{F}\, \frac{\partial \mathcal{W}(\bar{\mathbf{C}}, \{\mathbf{M}, \mathbf{N}\}, \eta, \xi)}{\partial \mathbf{C}}\, \mathbf{F}^{\text{T}}. \tag{13}$$

Replacing equation (6) in equation (13) with chain rules and the relations defined in equation (11) one can obtain

$$\boldsymbol{\sigma}_{\text{iso}} = \sum_{i\,=\,\text{M,F,}\tau} \left(\eta_i \boldsymbol{\sigma}_i^0 - (1-\xi_i)\boldsymbol{\sigma}_i^{\text{in}}\right), \tag{14}$$

so that

$$\boldsymbol{\sigma}_{\text{iso},i} = \eta_i \boldsymbol{\sigma}_i^0 - (1-\xi_i)\boldsymbol{\sigma}_i^{\text{in}}, \quad i \,=\, \text{M, F, } \tau \tag{15}$$

The volumetric part of the Cauchy stress is then determined as follows:

$$\boldsymbol{\sigma}_{\text{vol}} = p\mathbf{I}. \tag{16}$$

The constitutive equation for the hydrostatic pressure is given by $p = \partial \text{U}_{\text{vol}}/\partial J$.

3.4. Mullins softening and residual strain variables

Following [19], damage variables η_i and $\xi_i, i = \{\mathrm{M}, \mathrm{F}, \tau\}$ are respectively represented as follows:

$$\eta_i = 1 - \frac{1}{r_i}\operatorname{erf}\left[\frac{1}{m_i}(\bar{\Psi}_i^{\max} - \bar{\Psi}_i^0)\right], \tag{17}$$

and

$$\xi_i = \frac{1}{\tanh(1)}\tanh\left[\left(\frac{\bar{\Psi}_i^0}{\bar{\Psi}_i^{\max}}\right)^{n_i}\right]. \tag{18}$$

To characterize the damage induced by the matrix, fibers, and matrix–fiber mechanical interaction, the minimum value of the damage function is determined as follows:

$$\eta_i^{\min} = 1 - \frac{1}{r_i}\operatorname{erf}\left[\frac{1}{m_i}\bar{\Psi}_i^{\max}\right]. \tag{19}$$

The derivatives of the damage variables given in equations (17) and (18) with respect to $\bar{\Psi}_i^0$ are required to algorithmically implement the (pseudo)elasticity tensor, which read

$$\frac{\partial \eta_i}{\partial \bar{\Psi}_i^0} = \frac{2}{\sqrt{\pi} r_i m_i}\exp\left(-\left[\frac{1}{m_i}(\bar{\Psi}_i^{\max} - \bar{\Psi}_i^0)\right]^2\right), \tag{20}$$

and

$$\frac{\partial \xi_i}{\partial \bar{\Psi}_i^0} = \frac{n_i}{\bar{\Psi}_i^{\max}}\left(\frac{\bar{\Psi}_i^0}{\bar{\Psi}_i^{\max}}\right)^{n_i-1}\frac{1}{\tanh(1)}\left(1 - \tanh^2\left[\left(\frac{\bar{\Psi}_i^0}{\bar{\Psi}_i^{\max}}\right)^{n_i}\right]\right). \tag{21}$$

3.5. Elasticity tensors

Here, we provide the (pseudo)elasticity tensor ($\mathbb{c}$) in the Eulerian description required to update the consistent Jacobian matrix ($\mathbb{D}$), i.e., the DDSDDE variable in ABAQUS. (Note that although the term "elasticity tensor" is used here in accordance with its literature definition, the elasticity tensor also contains inelastic contributions within the pseudoelasticity framework.) For the purpose of computational

implementation, it is more customary to decouple $\mathbb{c}$ into volumetric and isochoric elastic responses as follows:

$$\mathbb{c} = \mathbb{c}_{\mathrm{iso}} + \mathbb{c}_{\mathrm{vol}}. \tag{22}$$

Before $\mathbb{c}_{\mathrm{iso}}$ can be obtained, its counterpart must be found in the Lagrangian description as

$$\mathbb{C}_{\mathrm{iso}} = \frac{\partial^2 \mathcal{W}(\bar{\mathbf{C}}, \{\mathbf{M}, \mathbf{N}\}, \eta, \xi)}{\partial \mathbf{C}\, \partial \mathbf{C}}. \tag{23}$$

Performing a $\mathbb{C}_{\mathrm{iso}}$ push-forward operation with $\mathbf{F}$ gives $\mathbb{c}_{\mathrm{iso}}$ in the Eulerian description. Then, taking the derivative of equation (14) with respect to $\mathbf{C}$ and applying the chain rule to equation (13), one can obtain a relation for the isochoric part of the (pseudo)elasticity tensor in the Eulerian description as follows:

$$\mathbb{c}_{\mathrm{iso}} = \sum_{i\,=\,\mathrm{M,F},\tau} \left(\left[\eta_i \mathbb{c}_i^0 + \frac{\partial \eta_i}{\partial \bar{\Psi}_i^0} \left(J\boldsymbol{\sigma}_i^0 \otimes J\boldsymbol{\sigma}_i^0 \right) \right] + \left[\frac{\partial \xi_i}{\partial \bar{\Psi}_i^0} \left(J\boldsymbol{\sigma}_i^0 \otimes J\boldsymbol{\sigma}_i^{\mathrm{in}} \right) \right] \right). \tag{24}$$

Note that when equation (14) is differentiated with respect to $\mathbf{C}$, the term $(1 - \xi_i)\, \partial \boldsymbol{\sigma}_i^{\mathrm{in}} / \partial \mathbf{C}$ appears and is always zero during loading and unloading (i.e., scalar $(1 - \xi_i) = 0$ during loading and tensor $\partial \boldsymbol{\sigma}_i^{\mathrm{in}} / \partial \mathbf{C} = \mathbb{O}$ during unloading and reloading). Note that although the inelastic part of the pseudoelasticity tensor is always zero during loading, it is determined using equation (24) during unloading and reloading below the maximum deformation.

The description of tensor (22) is completed using the definition of the volumetric elasticity tensor as follows:

$$\mathbb{c}_{vol} = \left(p + \frac{\partial p}{\partial J} \right) (\boldsymbol{I} \otimes \boldsymbol{I}) - 2p\mathbb{I}. \tag{25}$$

3.6. Energy functions

The functional forms of the decoupled potentials shown in equation (5) are defined as follows:

$$\Psi_{\tau} = \frac{c_1}{2c_2}[\exp(c_2(I_8^* - \cos(2\theta))^2) - 1] + c_3(I_8^* - \cos(2\theta))^2, \tag{26}$$

as proposed by [39] to account for the contributions of the matrix–fiber mechanical interaction, and

$$\Psi_{\mathrm{M}} = \mu(I_1 - 3) - p(J - 1), \quad \Psi_{\mathrm{F}} = \frac{k_1}{2}\sum_{i=4,6}(I_i - 1)^2, \tag{27}$$

where a linear function with respect to invariant I_1 and a quadratic function with respect to invariants I_4 and I_6 are considered for the matrix and fibers, respectively. Constants μ, k_1, c_1, and c_3 are positive material parameters for the stress dimension, and c_2 is a positive dimensionless parameter. Scalar p serves as an indeterminate Lagrange multiplier that can be identified as the hydrostatic pressure.

The functional form of the volumetric strain energy ($\mathrm{U_{vol}}$) is computed to check for convergence problems as follows:

$$\mathrm{U_{vol}}(J) = \frac{1}{4}\kappa(J^2 - 1 - 2\ln J), \tag{28}$$

where κ is the compressibility parameter with the dimension of the stress (see [53] for details).

Moreover, the decoupled forms of the functions in the inelastic energy dissipation (N) (recall Eq. (7)) are assumed to be the same as the previously described decoupled elastic potentials but with different material parameters. Thus,

$$N_{\tau} = \frac{c_1^N}{2c_2^N}\left[\exp\left(c_2^N\left(\bar{I}_8^{*N} - \cos(2\theta)\right)^2\right) - 1\right] + c_3^N\left(\bar{I}_8^{*N} - \cos(2\theta)\right)^2, \tag{29}$$

and

$$N_{\mathrm{M}} = \mu^N\left(\bar{I}_1^{\,N} - 3\right), \quad N_{\mathrm{F}} = \frac{k_1^N}{2}\sum_{i=4,6}\left(\bar{I}_i^{\,N} - 1\right)^2, \tag{30}$$

where μ^N, k_1^N, c_1^N, and c_2^N are positive material parameters with the dimension of stress and c_3^N is a positive dimensionless parameter.

4. **Finite element implementation**

4.1. Algorithmic implementation

Here, the algorithmic stress and (pseudo)elasticity tensors required to implement the pseudoelastic model are explained within the user-defined UMAT subroutine in the commercial ABAQUS software. Consider discrete time step $\mathrm{t} \in [\mathrm{t}_{n+1}, \mathrm{t}_n]$, where t_{n+1} and t_n denote the current and previous time steps, respectively, and corresponding energies $\left[\overline{\Psi}^0_{i\ n+1},\ \overline{\Psi}^0_{i\ n}\right], i = \{\mathrm{M}, \mathrm{F}, \tau\}$. If the current energy ($\overline{\Psi}^0_{i\ n+1}$) is greater than the corresponding energy at the previous time step (t_n) then no damage occurs within the interval. Otherwise, it is assumed that damage evolution occurs; hence, the Mullins softening invariants (η_i) and the residual strain invariants (ξ_i) are updated. The corresponding algorithm is presented in Appendix A.

For 3D solid elements, the Jaumann rate of the Kirchhoff stress tensor is required in the ABAQUS user-defined UMAT subroutine. Corresponding to this tensor is a fourth-order tensor represented by $\mathbb{D}$, which is a consistent Jacobian matrix referred to as the DDSDDE variable in the UMAT user material subroutine and is given by

$$\mathbb{D} = \mathbb{c} + \mathbb{H}, \qquad (\mathbb{H})_{ijkl} = \frac{1}{2}\left(\sigma_{ik}\delta_{jl} + \sigma_{jl}\delta_{ik} + \sigma_{il}\delta_{jk} + \sigma_{jk}\delta_{il}\right). \tag{31}$$

Spatial tensor $\mathbb{c}$ always exhibits both minor symmetry $(\mathbb{c})_{ijkl} = (\mathbb{c})_{jikl} = (\mathbb{c})_{ijlk}$ and major symmetry $\mathbb{c} = \mathbb{c}^T$ or $(\mathbb{c})_{ijkl} = (\mathbb{c})_{klij}$. The same symmetries can be assumed for tensor $\mathbb{H}$. The algorithm for constructing the stress and (pseudo)elasticity tensors is presented in Appendix A.

5. Results

5.1. Material and damage parameters

As discussed in Sections 2.2 and 2.3, the underlying mechanism producing the Mullins softening and permanent strain are attributed to matrix–fiber interfacial debonding and are modeled using the matrix–fiber interaction potential described in Section 3.2. Therefore, the pseudoelastic energy introduced in equation (6) is reduced to

$$\mathcal{W}(\bar{\mathbf{C}}, \{\mathbf{M}, \mathbf{N}\}, \eta, \xi) = \overline{\Psi}^0_{\mathrm{M}}(\bar{\mathbf{C}}) + \overline{\Psi}^0_{\mathrm{F}}(\bar{\mathbf{C}}, \{\mathbf{M}, \mathbf{N}\}) + \left[\eta_\tau \overline{\Psi}^0_\tau(\bar{\mathbf{C}}, \{\mathbf{M}, \mathbf{N}\}) + \phi_\tau(\eta_\tau)\right] - [(1 - \xi_\tau)\, N_\tau(\bar{\mathbf{C}}^N, \{\mathbf{M}, \mathbf{N}\}) + \rho_\tau(\xi_\tau)], \tag{32}$$

where the elastic energy functions defined in equations (26) and (27), the inelastic energy function (29), and the Mullins softening and residual stretch variables are given in equations (17) and (18), respectively. In equation (32), the inelastic Cauchy stress corresponding to Eq. (14) is therefore defined as follows:

$$\boldsymbol{\sigma}_{\mathrm{iso}} = \boldsymbol{\sigma}^0_{\mathrm{M}} + \boldsymbol{\sigma}^0_{\mathrm{F}} + \left(\eta_\tau \boldsymbol{\sigma}^0_\tau - (1 - \xi_\tau)\boldsymbol{\sigma}^{\mathrm{in}}_\tau\right). \tag{33}$$

The stress function ($\boldsymbol{\sigma}^0_{\mathrm{M}}$) in equation (33) corresponds to the elastic response of the matrix and is fitted to the experimental data given in Fig. 3. Thus, the fiber properties are obtained by fitting the stress function ($\boldsymbol{\sigma}^0_{\mathrm{M}} + \boldsymbol{\sigma}^0_{\mathrm{F}}$) to the orange curve shown in Fig. 3 corresponding to the extension of composites in the fiber direction. Then, by retaining the matrix and fiber parameters (c_{10} and k_1, respectively), the elastic stress function corresponding to the matrix–fiber mechanical interactions ($\boldsymbol{\sigma}^0_\tau$) is fitted to the primary loading path presented in Fig. 2(a). Mechanical interaction parameters c_1, c_2, and c_3 and the matrix and fiber parameters listed in Table 1 were thereby obtained independent of the damage parameters, which is an important advantage of the pseudoelasticity models described in [20,21].

Table 1. Material parameters obtained using inelastic model.

Contribution	μ, MPa	k_1, MPa	c_1, MPa	c_2, –	c_3, MPa
Matrix	0.40				
Fiber		227.0			
Matrix–fiber interaction			0.02496	2.0364	0.8948

By retaining the elastic material parameters listed in Table 1, Eq. (33) is fitted to the entire loading history of the cyclic loading–reloading stress–stretch results given in Fig. 2(a). For this purpose, the damage parameters are calibrated through inverse finite element modeling based on an FEM-model of the test samples using the optimization code LS-OPT employing the least-squares algorithm to minimize the discrepancy between the model results and the experimental data by the function as follows:

$$\Delta = \sum_{j=1}^{n} \left\| \phi_j^{\text{model}} - \phi_j^{\text{data}} \right\|^2, \tag{34}$$

where ϕ_j are the components of a force–displacement vector corresponding to the data points numbered by n. The boundary conditions and specimen geometry used in the FEM simulations are shown in Fig. 8. One end of the sample was fixed and the other was extended while it was constrained to move transverse to the loading. The corresponding damage parameters are listed in Table 2. The fitting results are compared with the experimentally determined cyclic stress–stretch behavior of the material, as shown in Fig. 9. The proposed constitutive model appears to be able to reproduce the rich material complexities such as nonlinearity, anisotropy, Mullins softening, and permanent strain. Parameters c_1^N, c_2^N, c_3^N, and n_τ effectively controlled the anisotropic damage-inducing permanent strain. The Mullins-softening-induced damage evolution is controlled by r_τ and m_τ, where larger values indicate slower damage evolution.

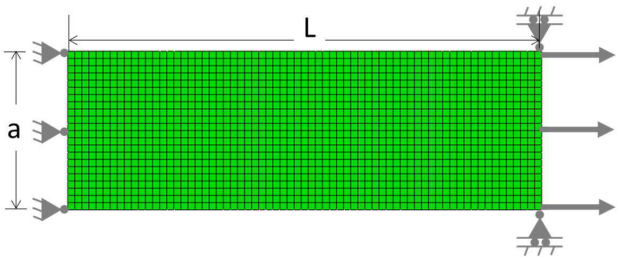

Fig. 8. Boundary conditions and specimen geometry used for FEM simulations.

Table 2. Damage parameters obtained using inelastic model.

Contribution	$r_\tau, -$	m_τ, MPa	c_1^N, MPa	$c_2^N, -$	c_3^N, MPa	$n_\tau, -$
Matrix–fiber debonding	1.02	0.18	0.455	0.50	0.05	8

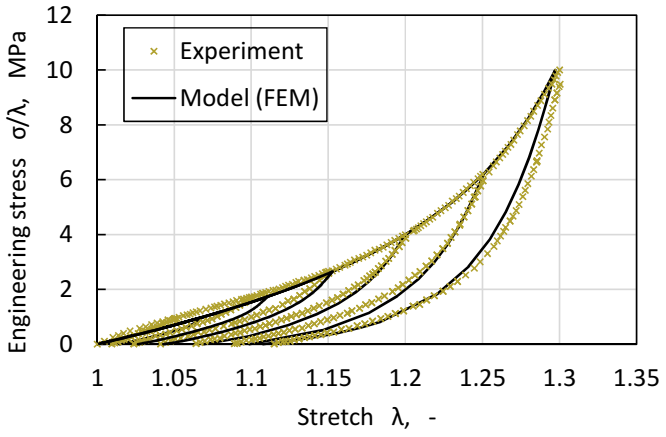

Fig. 9. Model fitting obtained for cyclic tensile tests of composite prepared with fibers oriented at [+45/−45].

5.2. Validation

To validate the predictions of the proposed inelastic damage model, cyclic stress–stretch experimental responses obtained for asymmetric deformations (shown in Fig. 2(b)) are compared with the simulation (FEM) results obtained for the composite prepared with fibers oriented at [+30/−60] and subjected to tensile deformation in the $\mathbf{e}_1$ direction to increase the stretch levels. The material and damage parameters listed in Table 1 and Table *2* are used. The loading–reloading results presented in Fig. 10 show reasonable agreement. Using exact elasticity tensors rather than approximate ones provided a robust computational framework that allowed simulations to quadratically converge very quickly near the solution point.

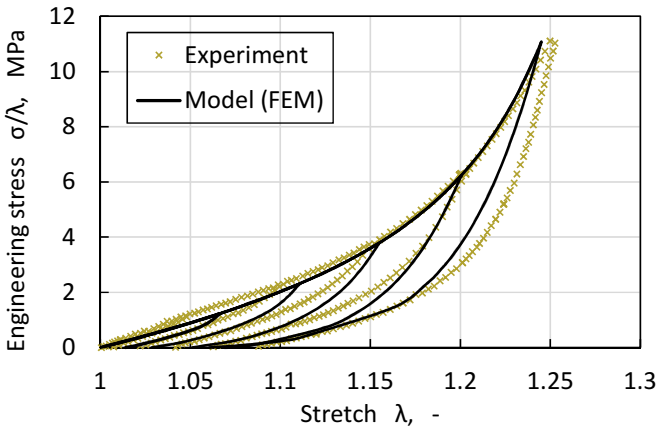

Fig. 10. Verification of model performance by comparing FEM and experimental results obtained for composite prepared with fibers oriented at [+30/−60] and then subjected to cyclic uniaxial extensions in $\boldsymbol{e}_1$ direction.

The local stretch maps captured using the DIC method (see Fig. 7) are compared with the FEM simulation results obtained for the composite prepared with fibers oriented at [+45/−45] during the cyclic tensile test in the $\mathbf{e}_1$ direction, as explained in Section 2.4. Fig. 11(a) and (b) show the results corresponding to the maximum local stretches obtained at loading and the permanent stretches obtained after unloading, respectively. Overall, the FEM and experimental results agreed well, both qualitatively and quantitatively.

However, there is a slight discrepancy between the FEM and experimental results obtained near the clamping area, which can be explained by local clamping effects during testing. Although a clamping system had been designed by applying clamping forces to five areas of the samples to avoid specimen slippage in the loading direction, some minor transverse slippage clearly still occurred at the clamps. These effects were, of course, not included in the model because a detailed study of the clamping effects would have been beyond the scope of the present study.

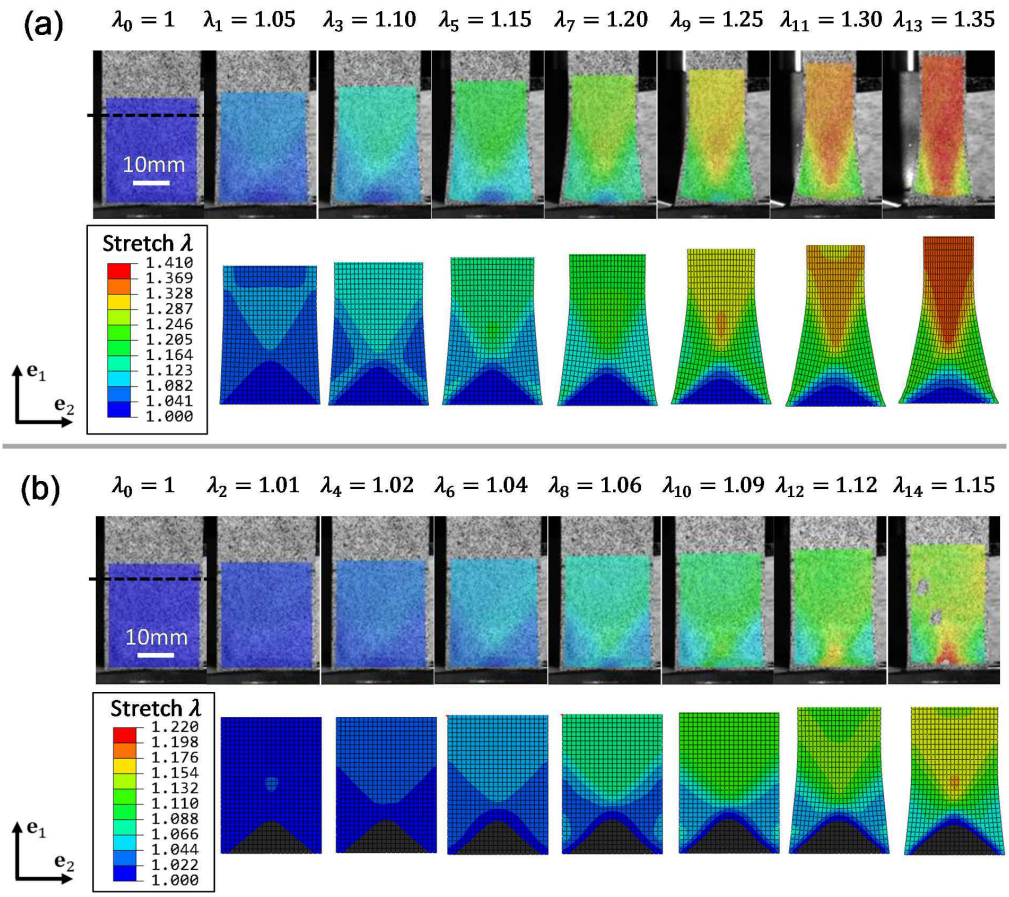

Fig. 11. Comparison of FEM simulation results to full-field stretch maps captured by DIC for composite prepared with fibers oriented at $[+45/-45]$ and then subjected to cyclic tensile tests in $\boldsymbol{e}_1$ direction: (a) loading and (b) unloading exhibiting profound residual deformations.

6. Discussion and conclusion

6.1. Experimental

The experimental observations indicated that the fiber-reinforced soft composites exhibited complex properties such as nonlinearity, anisotropy, Mullins softening, and permanent strain. The contribution of the microstructural evolution to mechanical property degradation was discussed based on microscopically visible matrix–fiber interfacial debonding. The results of the cyclic tensile tests on the pure matrix, fibers, and composites implied that the underlying mechanism producing the Mullins softening and permanent deformations could be attributed to matrix–fiber interfacial debonding and not to the matrix or fibers. This finding was supported by matrix–fiber interfacial debonding observed in the micrographs captured during the *in-situ* tensile tests and was reflected in the residual deformations recorded in the stretch maps by digital image correlation after unloaded samples. *In-situ* optical micrographs indicated different microstructural evolutions: continuous matrix–fiber debonding along the fibers barely visible after unloading and discontinuous pointwise matrix–fiber debonding starting from the top vicinity of the fibers and continuing to the matrix. The information obtained from the experiments may serve as useful input parameters for modeling.

6.2. Modeling

We presented a model covering almost the entire phenomenology of hyperelastic fiber-reinforced materials; that is, nonlinearity, anisotropy, Mullins softening, and permanent deformations while being proposed for high efficiency and robustness in finite element application. Mullins softening and permanent deformations were described using a phenomenological matrix–fiber damage potential, which were physically more meaningful because mechanical properties degraded owing to microscopic matrix–fiber interfacial debonding. The distinct contributions of the individual composite constituents to the elastic and inelastic mechanical behaviors of cyclically loaded materials were elucidated based on the following key points. (i) Particular elastic and pseudoelastic energy functions were primarily used to distinguish between the respective contributions of the individual constituent materials. (ii) Pseudoelasticity was adopted as a damage framework to obtain damage contributions from any of the individual constituent materials independent of the elastic properties. (iii) Separate damage variables were used to distinguish between inelastic mechanical behaviors such as Mullins softening and permanent strain. The model implemented in a user-defined subroutine was capable of reproducing inelastic behaviors as a result of the matrix–fiber debonding resulted in considerably degraded mechanical properties.

Declaration of Competing Interests

The authors declare that they have no known competing financial interests or personal relationships that could have influenced the work reported in this paper.

CRediT authorship contribution statement

M.R. Mansouri: Conceptualization, software, investigation, formal analysis, writing - original draft. **P.F. Fuchs:** Funding acquisition, supervision, writing - review & editing. **M. Baghani:** Software, Supervision, Writing - Review and Editing. **C. Schuecker:** supervision, writing - review, and editing.

Acknowledgment

The research was conducted within the COMET-project "ELASTIC LOAD COUPLING WITH TAILORED ELASTOMER COMPOSITES II" (project no.: VII-3.S2) at the Polymer Competence Center Leoben GmbH (PCCL, Austria) within the framework of the COMET program of the Federal Ministry for Climate Action, Environment, Energy, Mobility, Innovation, and Technology and the Federal Ministry for Digital and Economic Affairs with contributions from the Chair of the Materials Science and Testing of Polymers Department, Montanuniversitaet Leoben, and the Institute of Lightweight Design and Structural Biomechanics, Vienna University of Technology.

Supplementary materials

Supplementary materials associated with this paper can be found in the online version at http://dx.doi.org/10.17632/9wpnhty7zk.1.

Appendix A. Algorithmic implementation of inelastic damage model.

Algorithm A.1. Computation of stress and elasticity tensors considering stress softening and permanent deformation in the context of pseudoelasticity, as implemented using UMAT user-defined interface in ABAQUS software.

Subroutine UMAT

(1) Input:
deformation gradient **F** at each integration point (DFGRD1), properties (PROPS),
number of direct and shear stress components: (NDI) and (NSHR), respectively.

Start

compute $\left[\bar{\Psi}^0_{i\,n+1},\ \bar{\Psi}^0_{i\,n}\right]$, $i = \mathrm{M, F, \tau}$, corresponding to a specific time interval $[\mathrm{t}_{n+1}, \mathrm{t}_n]$

(2) Update Mullins softening and residual strain variables

if $\bar{\Psi}^0_{i\,n+1} \geq \bar{\Psi}^0_{i\,n}$ then $\quad (i = \mathrm{M, F, \tau})$

$\bar{\Psi}^{\max}_{i\,n+1} = \bar{\Psi}^0_{i\,n+1} \rightarrow \ \wr r_i^{\max} = \bar{\Psi}^{\max}_{i\,n+1}$ and $\quad \bar{\mathbf{C}}^N = \bar{\mathbf{C}}_{n+1}$

$\eta_i = 1, \quad \xi_i = 1, \quad \partial\eta_i/\partial\bar{\Psi}^0_i = 0, \quad \partial\xi_i/\partial\bar{\Psi}^0_i = 0,$

else

$\eta_i = 1 - \frac{1}{r_i}\mathrm{erf}\left[\frac{1}{m_i}\left(\wr r_i^{\max} - \bar{\Psi}^0_{i\,n+1}\right)\right]$

$\xi_i = \frac{1}{\tanh(1)}\tanh\left[\left(\frac{\bar{\Psi}^0_{i\,n+1}}{\wr r_i^{\max}}\right)^{n_i}\right]$

$\bar{I}_1{}^N = \mathrm{tr}\bar{\mathbf{C}}^N,\ \bar{I}_4{}^N = \bar{\mathbf{C}}^N\!:\mathbf{M}\otimes\mathbf{M},\ \bar{I}_6{}^N = \bar{\mathbf{C}}^N\!:\mathbf{N}\otimes\mathbf{N},\ \bar{I}_8{}^N = \bar{\mathbf{C}}^N\!:\mathbf{M}\otimes\mathbf{N}$

$N_{n+1}(\bar{\mathbf{C}}^N, \{\mathbf{M}, \mathbf{N}\}) = \left(N_{\mathrm{M}}\left(\bar{I}_1{}^N\right) + N_{\mathrm{F}}\left(\bar{I}_4{}^N, \bar{I}_6{}^N\right) + N_{\tau}\left(\bar{I}_8^{*N}\right)\right)_{n+1}$

end if

(3) Update elastic and inelastic stresses

if $\bar{\Psi}^0_{i\,n+1} \geq \bar{\Psi}^0_{i\,n}$ then $\quad (i = \mathrm{M, F, \tau})$

$\boldsymbol{\sigma}_{\mathrm{iso}\,n+1} = \sum_{i\,=\,\mathrm{M,F,\tau}} \boldsymbol{\sigma}^0_{i\,n+1}$

$\boldsymbol{\sigma}_{n+1} = (\boldsymbol{\sigma}_{\mathrm{iso}} + \boldsymbol{\sigma}_{\mathrm{vol}})_{n+1} \quad \rightarrow \quad$ STRESS

else

$\bar{\boldsymbol{\sigma}}^{\mathrm{in}}_{i\,n+1} = 2\,J^{-1}\bar{\mathbf{F}}\,\frac{\partial N_{i\,n+1}}{\partial\bar{\mathbf{C}}^N}\,\bar{\mathbf{F}}^{\mathrm{T}}$

$\boldsymbol{\sigma}^{\mathrm{in}}_{i\,n+1} = \mathbb{P} : \bar{\boldsymbol{\sigma}}^{\mathrm{in}}_{i\,n+1}$

$\boldsymbol{\sigma}_{\mathrm{iso}\,n+1} = \sum_{i\,=\,\mathrm{M,F,\tau}}\left(\eta_i\boldsymbol{\sigma}^0_{i\,n+1} - (1-\xi_i)\,\boldsymbol{\sigma}^{\mathrm{in}}_{i\,n+1}\right)$

$\boldsymbol{\sigma}_{n+1} = (\boldsymbol{\sigma}_{\mathrm{iso}} + \boldsymbol{\sigma}_{\mathrm{vol}})_{n+1} \quad \rightarrow \quad$ STRESS

end if

(4) Update (pseudo)elasticity tensor

compute fourth–order matrix $\left(\mathbb{H}_{\mathrm{ijkl}}\right)_{n+1} = \frac{1}{2}\left(\sigma_{\mathrm{ik}}\delta_{\mathrm{jl}} + \sigma_{\mathrm{jl}}\delta_{\mathrm{ik}} + \sigma_{\mathrm{il}}\delta_{\mathrm{jk}} + \sigma_{\mathrm{jk}}\delta_{\mathrm{il}}\right)_{n+1}$

compute Eulerian description of fictitious tensor $\bar{\mathbb{C}}^0_{n+1} = 4\,\bar{\mathbf{F}}\,\bar{\mathbf{F}}\,\frac{\partial^2\bar{\Psi}^0_{i\,n+1}}{\partial\bar{\mathbf{C}}\,\partial\bar{\mathbf{C}}}\,\bar{\mathbf{F}}^{\mathrm{T}}\bar{\mathbf{F}}^{\mathrm{T}}$ $(i = \mathrm{M, F, \tau})$

$\mathbb{c}^0_{n+1} = \sum_{i=\mathrm{M,F,\tau}}\left(J^{-1}\mathbb{P} :\ \bar{\mathbb{C}}^0_{i\,n+1} : \mathbb{P} + \frac{2}{3}\mathrm{tr}\left(\bar{\boldsymbol{\sigma}}^0_i\right)_{n+1}\mathbb{P} - \frac{2}{3}\left(\mathbf{I}\otimes\boldsymbol{\sigma}^0_{i\,n+1} + \boldsymbol{\sigma}^0_{i\,n+1}\otimes\mathbf{I}\right)\right)$

compute $\mathbb{c}_{\mathrm{iso}\,n+1} = \sum_{i\,=\,\mathrm{M,F,\tau}}\left(\left[\eta_i\mathbb{c}^0_{i\,n+1} + \frac{\partial\eta_i}{\partial\bar{\Psi}^0_i}\left(J\boldsymbol{\sigma}^0_i\otimes J\boldsymbol{\sigma}^0_i\right)_{n+1}\right] + \left[\frac{\partial\xi_i}{\partial\bar{\Psi}^0_i}\left(J\boldsymbol{\sigma}^0_i\otimes J\boldsymbol{\sigma}^{\mathrm{in}}_i\right)_{n+1}\right]\right)$

compute Eulerian description of (pseudo)elasticity tensor $\mathbb{c}_{n+1} = (\mathbb{c}_{\mathrm{iso}} + \mathbb{c}_{\mathrm{vol}})_{n+1}$

calculate tangent stiffness matrix, i.e., $\mathbb{D}_{n+1} = \mathbb{c}_{n+1} + \mathbb{H}_{n+1} \quad \rightarrow \quad$ DDSDDE

End Subroutine UMAT

References

[1] Karger-Kocsis J, Mahmood H, Pegoretti A. Recent advances in fiber/matrix interphase engineering for polymer composites. Progress in Materials Science 2015;73:1–43.

[2] Kim J-K, Hodzic A. Nanoscale characterisation of thickness and properties of interphase in polymer matrix composites. The Journal of Adhesion 2003;79(4):383–414.

[3] Bellini A, Bovo M, Mazzotti C. Experimental and numerical evaluation of fiber-matrix interface behaviour of different FRCM systems. Composites Part B: Engineering 2019;161:411–26.

[4] Khandelwal S, Rhee KY. Recent advances in basalt-fiber-reinforced composites: Tailoring the fiber-matrix interface. Composites Part B: Engineering 2020;192:108011.

[5] Palola S, Vuorinen J, Noordermeer JWM, Sarlin E. Development in Additive Methods in Aramid Fiber Surface Modification to Increase Fiber-Matrix Adhesion: A Review. Coatings 2020;10(6):556.

[6] Drzal LT, Madhukar M. Fibre-matrix adhesion and its relationship to composite mechanical properties. J Mater Sci 1993;28(3):569–610.

[7] Zhong J, Luo Z, Hao Z, Guo Y, Zhou Z, Li P et al. Enhancing fatigue properties of styrene butadiene rubber composites by improving interface adhesion between coated aramid fibers and matrix. Composites Part B: Engineering 2019;172:485–95.

[8] Mansouri MR, Beter J, Fuchs PF, Schrittesser B, Pinter G. Quantifying matrix-fiber mechanical interactions in hyperelastic materials. International Journal of Mechanical Sciences 2021;195:106268. https://doi.org/10.1016/j.ijmecsci.2021.106268.

[9] Cao L, Sinha TK, Tao L, Li H, Zong C, Kim JK. Synergistic reinforcement of silanized silica-graphene oxide hybrid in natural rubber for tire-tread fabrication: A latex based facile approach. Composites Part B: Engineering 2019;161:667–76.

[10] Khiêm VN, Itskov M. An averaging based tube model for deformation induced anisotropic stress softening of filled elastomers. International Journal of Plasticity 2017;90:96–115.

[11] Diani J, Fayolle B, Gilormini P. A review on the Mullins effect. European Polymer Journal 2009;45(3):601–12.

[12] Diani J, Brieu M, Vacherand JM. A damage directional constitutive model for Mullins effect with permanent set and induced anisotropy. European Journal of Mechanics-A/Solids 2006;25(3):483–96.

[13] Lv C, Wang J, Li Z, Zhao K, Zheng J. Degradable, reprocessable, self-healing PDMS/CNTs nanocomposite elastomers with high stretchability and toughness based on novel dual-dynamic covalent sacrificial system. Composites Part B: Engineering 2019;177:107270.

[14] Clough JM, Creton C, Craig SL, Sijbesma RP. Covalent bond scission in the Mullins effect of a filled elastomer: real-time visualization with mechanoluminescence. Advanced Functional Materials 2016;26(48):9063–74.

[15] Marckmann G, Verron E, Gornet L, Chagnon G, Charrier P, Fort P. A theory of network alteration for the Mullins effect. Journal of the Mechanics and Physics of Solids 2002;50(9):2011–28.

[16] Hanson DE, Hawley M, Houlton R, Chitanvis K, Rae P, Orler EB et al. Stress softening experiments in silica-filled polydimethylsiloxane provide insight into a mechanism for the Mullins effect. Polymer 2005;46(24):10989–95.

[17] Mansouri, Fuchs PF. Elastic load coupling with tailored elastomer composites. Composites Part C: Open Access 2020:100088.

[18] Dorfmann A, Ogden RW. A constitutive model for the Mullins effect with permanent set in particle-reinforced rubber. International Journal of Solids and Structures 2004;41(7):1855–78.
[19] Ogden RW, Roxburgh DG. A pseudo–elastic model for the Mullins effect in filled rubber. Proceedings of the Royal Society A: Mathematical, Physical and Engineering Sciences 1999;455(1988):2861–77.
[20] Weisbecker H, Pierce DM, Regitnig P, Holzapfel GA. Layer-specific damage experiments and modeling of human thoracic and abdominal aortas with non-atherosclerotic intimal thickening. J Mech Behav Biomed Mater 2012;12:93–106.
[21] Rausch MK, Humphrey JD. A microstructurally inspired damage model for early venous thrombus. J Mech Behav Biomed Mater 2016;55:12–20.
[22] Ghasemi M, Nolan DR, Lally C. An investigation into the role of different constituents in damage accumulation in arterial tissue and constitutive model development. Biomechanics and modeling in mechanobiology 2018;17(6):1757–69.
[23] Peña E. Prediction of the softening and damage effects with permanent set in fibrous biological materials. Journal of the Mechanics and Physics of Solids 2011;59(9):1808–22.
[24] Bai L, Yan X, Feng B, Zheng J. Mechanically strong, healable, and reprocessable conductive carbon black/silicone elastomer nanocomposites based on dynamic imine bonds and sacrificial coordination bonds. Composites Part B: Engineering 2021;223:109123.
[25] Arash B, Exner W, Rolfes R. Viscoelastic damage behavior of fiber reinforced nanoparticle-filled epoxy nanocomposites: Multiscale modeling and experimental validation. Composites Part B: Engineering 2019;174:107005. https://doi.org/10.1016/j.compositesb.2019.107005.
[26] Doblaré M. An anisotropic pseudo-elastic approach for modelling Mullins effect in fibrous biological materials. Mechanics Research Communications 2009;36(7):784–90.
[27] Chagnon G, Rebouah M, Favier D. Hyperelastic Energy Densities for Soft Biological Tissues: A Review. J Elast 2015;120(2):129–60.
[28] Gracia LA, Peña E, Royo JM, Pelegay JL, Calvo B. A comparison between pseudo-elastic and damage models for modelling the Mullins effect in industrial rubber components. Mechanics Research Communications 2009;36(7):769–76.
[29] Guo Z, Sluys LJ. Computational modelling of the stress-softening phenomenon of rubber-like materials under cyclic loading. European Journal of Mechanics-A/Solids 2006;25(6):877–96.
[30] Fung YC, Fronek K, Patitucci P. Pseudoelasticity of arteries and the choice of its mathematical expression. American Journal of Physiology-Heart and Circulatory Physiology 1979;237(5):H620-H631.
[31] Fereidoonnezhad B, Naghdabadi R, Holzapfel GA. Stress softening and permanent deformation in human aortas: continuum and computational modeling with application to arterial clamping. J Mech Behav Biomed Mater 2016;61:600–16.
[32] Mo C, Jiang Y, Raney JR. Microstructural evolution and failure in short fiber soft composites: experiments and modeling. Journal of the Mechanics and Physics of Solids 2020:103973.
[33] Mansouri, Darijani H, Baghani M. On the correlation of FEM and experiments for hyperelastic elastomers. Exp Mech 2017;57(2):195–206.
[34] Plagge J, Ricker A, Kröger NH, Wriggers P, Klüppel M. Efficient modeling of filled rubber assuming stress-induced microscopic restructurization. International Journal of Engineering Science 2020;151:103291.
[35] Jia Y, Yue X, Wang Y, Yan C, Zheng G, Dai K et al. Multifunctional stretchable strain sensor based on polydopamine/reduced graphene oxide/electrospun thermoplastic polyurethane fibrous mats for human motion detection and environment monitoring. Composites Part B: Engineering 2020;183:107696.

[36] Al-Anany YM, Tait MJ. Experimental assessment of utilizing fiber reinforced elastomeric isolators as bearings for bridge applications. Composites Part B: Engineering 2017;114:373–85.
[37] Georgousis G, Roumpos K, Kontou E, Kyritsis A, Pissis P, Koutsoumpis S et al. Strain and damage monitoring in SBR nanocomposites under cyclic loading. Composites Part B: Engineering 2017;131:50–61.
[38] Mansouri MR. Matrix-fiber interface debonding in soft materials: Modeling and microstructural evolution. Mendeley Data, V1 2021. https://doi.org/10.17632/9wpnhty7zk.1.
[39] Mansouri, Fuchs PF, Criscione JC, Schrittesser B, Beter J. The contribution of mechanical interactions to the constitutive modeling of fiber-reinforced elastomers. European Journal of Mechanics-A/Solids 2020:104081.
[40] Spencer AJM. Constitutive theory for strongly anisotropic solids. In: Continuum theory of the mechanics of fibre-reinforced composites. Springer; 1984, p. 1–32.
[41] Criscione JC, Hunter WC. Kinematics and elasticity framework for materials with two fiber families. Continuum Mechanics and Thermodynamics 2003;15(6):613–28.
[42] Mansouri MR, Fuchs PF, Criscione J, Schrittesser B, Beter J. The contribution of mechanical interactions to the constitutive modeling of fiber-reinforced elastomers. European Journal of Mechanics - A/Solids: in press, 2020.
[43] Merodio J, Ogden RW. The influence of the invariant on the stress–deformation and ellipticity characteristics of doubly fiber-reinforced non-linearly elastic solids. International Journal of Non-Linear Mechanics 2006;41(4):556–63. https://doi.org/10.1016/j.ijnonlinmec.2006.02.001.
[44] Peng X, Guo Z, Du T, Yu W-R. A simple anisotropic hyperelastic constitutive model for textile fabrics with application to forming simulation. Composites Part B: Engineering 2013;52:275–81.
[45] Wang J, Peng X, Huang Z, Zhou H. A temperature-dependent 3D anisotropic visco-hyperelastic constitutive model for jute woven fabric reinforced poly (butylene succinate) biocomposite in thermoforming. Composites Part B: Engineering 2021;208:108584.
[46] Holzapfel GA, Ogden RW. An arterial constitutive model accounting for collagen content and cross-linking. Journal of the Mechanics and Physics of Solids 2020;136:103682.
[47] Gilchrist MD, MacManus D, Murphy JG, Pierrat B. A new formulation of slight compressibility for arterial tissue and its Finite Element implementation. Computer methods in biomechanics and biomedical engineering 2017;20(4):403–14.
[48] Gong Y, Peng X, Yao Y, Guo Z. An anisotropic hyperelastic constitutive model for thermoplastic woven composite prepregs. Composites Science and Technology 2016;128:17–24.
[49] Melnik AV, Luo X, Ogden RW. A generalised structure tensor model for the mixed invariant I8. International Journal of Non-Linear Mechanics 2018. https://doi.org/10.1016/j.ijnonlinmec.2018.08.018.
[50] Sacks MS, Zhang W, Wognum S. A novel fibre-ensemble level constitutive model for exogenous cross-linked collagenous tissues. Interface focus 2016;6(1):20150090.
[51] Holzapfel GA, Ogden RW. Constitutive modelling of passive myocardium: a structurally based framework for material characterization. Philosophical Transactions of the Royal Society A: Mathematical, Physical and Engineering Sciences 2009;367(1902):3445–75.
[52] Lazopoulos KA, Ogden RW. Nonlinear elasticity theory with discontinuous internal variables. Mathematics and Mechanics of Solids 1998;3(1):29–51.
[53] Holzapfel GA. Nonlinear solid mechanics: A continuum approach for engineering science. Meccanica 2002;37(4):489–90.

Conflict of Interest

Declaration of interests

☒ The authors declare that they have no known competing financial interests or personal relationships that could have appeared to influence the work reported in this paper.

☐The authors declare the following financial interests/personal relationships which may be considered as potential competing interests:

CRediT authorship contribution statement

M.R. Mansouri: Conceptualization, software, investigation, formal analysis, writing - original draft.

P.F. Fuchs: Funding acquisition, supervision, writing - review & editing.

M. Baghani: Software, Supervision, Writing - Review and Editing.

C. Schuecker: supervision, writing - review, and editing.

Composites Part C: Open Access 4 (2021) 100088

Contents lists available at ScienceDirect

Composites Part C: Open Access

journal homepage: www.elsevier.com/locate/jcomc

Elastic load coupling with tailored elastomer composites

M.R. Mansouri*, P.F. Fuchs

Polymer Competence Center Leoben GmbH, Leoben, Austria

ARTICLE INFO

Keywords:
Flexible composite
Load-coupling behavior
Anisotropy
Finite element analysis

ABSTRACT

This study identifies a unique performance benefit in flexible composite laminates through evaluation of the load-coupling potentials once an external stimulus triggers extensional loadings. A combination of soft elastomers with stiff fibers can be used to develop a composite with distinct direction-dependent properties. Unique exponential flexibility changes in some directions and extreme linear stiffness in others are observed. These tunable multidirectional flexibilities can be achieved at different flexibility ratios tailored to a wide range of applications, such as extension-twist coupling in composite laminates. To this end, the conflicting design requirements such as decoupling ratio between deformation modes, i.e. extension and twist, and torsional flexibility are studied for laminates with different ply thicknesses, stacking directions, constituent materials, and numbers of plies. A design space is then introduced and used to evaluate the capability of laminates for effective load-coupling behaviors. It is also demonstrated that significant differences in the (linear) stiffness of the constituent materials result in highly nonlinear mechanics in hyperelastic fiber-reinforced composites, mainly owing to the contributions of the matrix-fiber mechanical interaction.

1. Introduction

Hyperelastic fiber-reinforced materials are generally classified as either organic (including myocardium and arterial walls) or inorganic (including fiber-reinforced elastomers). From early history to the present, the highest functionalities have been assigned to healthy fibrous organs, while distinct functionalities—for example, load coupling behaviors—have been supported through the build-up of inorganic, fiber-reinforced composites. Most works in the field of biomaterial mechanics have focused on the modeling and characterization of these materials, while functionality is an additional consideration for designing inorganic fiber-reinforced composites. Past efforts in the study of classic composites were mostly devoted to harnessing fiber-reinforced composites' extreme properties, such as their high tensile strength and low elongation. As reinforcements, glass, polyester, and carbon fibers have a high tensile strength, and, within their operating limits, they show very little deformation. When they are embedded in a soft elastomer, it harnesses their key characteristics in an exceptionally flexible form, enabling the development of fiber-reinforced materials in soft applications. These applications include pressure-controlled robotic actuators [1–4], soft wearable systems [5,6], morphing aircraft wings [7–10], artificial muscles [5,11,12], elastofluidics [13–15], aerospace applications [16–18], and energy-absorbing composite systems [7,19]. Some of these applications are shown in Fig. 1.

The properties of fiber-reinforced composite laminates can be tailored with stacking sequence of layers and selection of appropriate materials to produce a desired load-coupling behavior such as extension-twist coupling, which is a frequently encountered phenomenon in structures [20]. This study identifies a unique performance benefit in flexible composite laminates through evaluation of the load-coupling potentials once an external stimulus triggers extensional loadings. To this end, the conflicting design requirements as decoupling ratio between deformation modes, referred to herein as extension and twist in laminates, and torsional flexibility are studied. They could be used in products such as morphing systems, which are characterized by conflicting requirements like "exhibit low in-plane stiffness while maintaining large strain capability and exceptional flexibility." In particular, material anisotropy is exploited in order to maximize the load-coupling potential of composite laminates. Therefore, as a basis, the direction-dependent nonlinear material behavior of selected possible composites is characterized and modeled. These developed tools and methods pave the way for establishing a completely different view of these composites, offering immense potential for possible applications and the introduction of a new class of intelligent materials.

* Corresponding author.
E-mail address: mohammad.mansouri@pccl.at (M.R. Mansouri).

https://doi.org/10.1016/j.jcomc.2020.100088
Received 22 October 2020; Received in revised form 9 December 2020; Accepted 11 December 2020

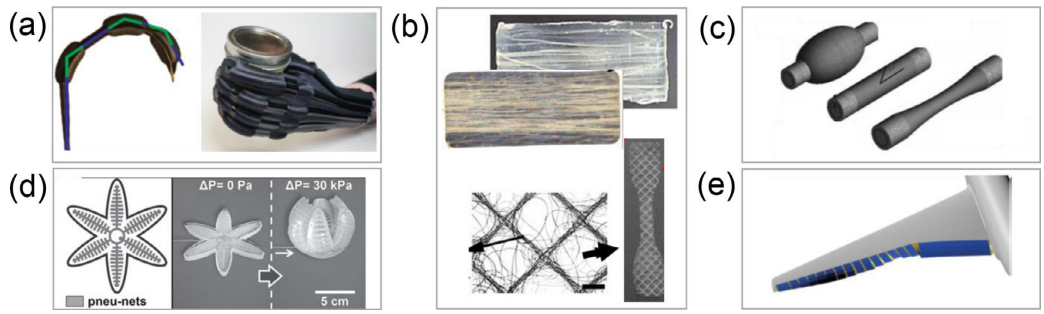

Fig. 1. Some applications of soft reinforced materials: a) wearable robots [5]; b) biocompatible materials [21,22]; c) artificial muscles [23]; d) soft actuators [24]; and e) morphing wings [25].

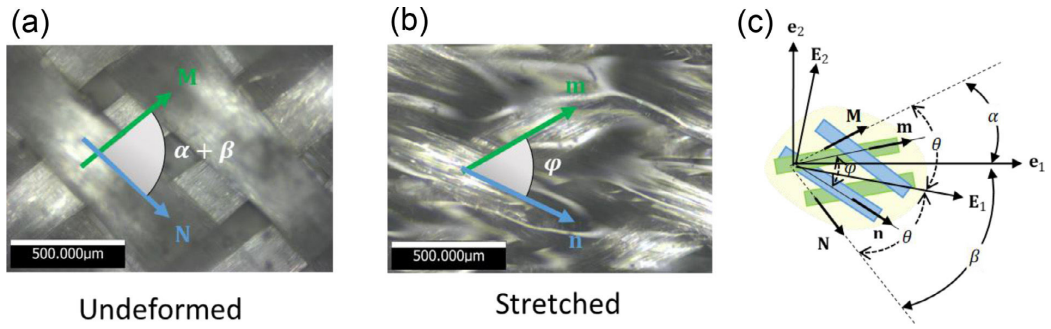

Fig. 2. (a) Micrographs of an undeformed region with two fiber families shown by the directions $\boldsymbol{M}$ and $\boldsymbol{N}$; (b) fiber directions after deformation shown by $\boldsymbol{m}$ and $\boldsymbol{n}$; (c) schematic illustrations of the relation between fiber angle at undeformed and stretched configurations, where $\boldsymbol{E}_1$ in the orthogonal coordinate system $\{\boldsymbol{E}_1,\boldsymbol{E}_2\}$ is the bisector of fibers at undeformed state. A fixed coordinate system such as $\{\boldsymbol{e}_1,\boldsymbol{e}_2\}$ is applied for specifying the loading in the $\boldsymbol{e}_1$ direction.

2. Experimental

2.1. Materials and methods

Hyperelastic single-lamella fiber-reinforced composites with constituents including polydimethylsiloxane (PDMS) as a matrix and endless, twill woven glass fibers (GF) as reinforcement are manufactured. The glass fiber is provided from CS Interglas AG (Erbach, Germany) as E-type fibers with a standard industrial finish (FK144) and the classification EC9–69 × 5t0 with a twine thickness of about 68tex. The mean fiber diameter of a single filament is about 10 μm and an area weight of 200g/m^2. The PDMS used here is an addition-curing two-component system with a hardness of 35 Shore A, a density of 1.02 g/cm^3 and a viscosity in an uncured state of 3500 mPas and pot life of about 90 min at room temperature. The specimens are manufactured using vacuum assisted resin infusion (VARI) with a vacuum pressure of 20 mbar. The woven fabric is placed in a mold and then exposed to a matrix flow. After impregnation, the composite part is cured at 70 ○C for 1 h in a temperature chamber.

Samples contain two fiber families initially aligned in the preferred directions $\mathbf{M} = \cos\theta\mathbf{E}_1 + \sin\theta\mathbf{E}_2$ and $\mathbf{N} = \cos\theta\mathbf{E}_1 - \sin\theta\mathbf{E}_2$, where the orthogonal coordinate system $(\mathbf{E}_1,\mathbf{E}_2)$ is defined so that $\mathbf{E}_1$ is the bisector of fibers at undeformed state and the angle θ represents half of the angle subtended by $\mathbf{M}$ and $\mathbf{N}$ in this system. For simplicity, a fixed coordinate system such as $\{\mathbf{e}_1,\mathbf{e}_2,\mathbf{e}_3\}$ is adopted for specifying the loading in the $\mathbf{e}_1$ direction so that the two fiber families in this system are defined as $\mathbf{M} = \cos\alpha\,\mathbf{e}_1 + \sin\alpha\mathbf{e}_2$ and $\mathbf{N} = \cos\beta\mathbf{e}_1 + \sin\beta\mathbf{e}_2$, $\alpha > 0$ and $\beta < 0$. In this coordinate system, the α and β are angles associated respectively with the preferred fiber orientations $\mathbf{M}$ and $\mathbf{N}$ constructed with respect to the loading direction $\mathbf{e}_1$. The angle between deformed fibers is indicated by ϕ in Fig. 2(b). The relations between $(\alpha, \beta, \theta, \phi)$ are illustrated in Fig. 2.

Samples with an aspect ratio of $\xi = 3/\tan\alpha$ are prepared to have a thickness of approximately 0.4 mm, where $l_0 = 3a/\tan\alpha$ is the length and $a = 30$mm denotes the width of the samples, respectively. The sample geometry is defined such that, at least, one end of each featured fiber inside the evaluation area is free-ended, and therefore no clamping effects have to be considered. Composites with a preferred fiber orientation defined by $[+\alpha-\beta]$, such as [+30 − 60] and [+45 − 45] are subjected to tensile tests in the $\mathbf{e}_1$ direction. Composites with the fiber orientation [+0 − 90] are stretched in one of the fiber directions (both fibers have the same contributions to the deformation). For this fiber orientation, the sample aspect ratio is not critical and is adopted here as $\xi = 3$ with $l_0 = 90$mm and $a = 30$mm. The pure matrix is also characterized using tensile tests on PDMS material (for a detailed discussion on the constitutive modeling and experimental characterization of isotropic elastomers, the reader is referred to, for example, [26] and [27] and references therein).

The average stress-stretch response of three samples cut through from the same sheet is reported for each setting. Tests are carried out by the universal testing machine Z250 (Zwick Roell GmbH & Co. KG) at a quasi-static rate of 10 mm/min. To map the local stretches of the samples, 3D full-field, high-resolution images are captured via a digital image correlation (DIC) system (Mercury BLFY 050 camera with Mercury RT software, Czech Republic) including a spray pattern on the specimen surface suitable for the high elasticity of the matrix material. Within the deformation range applied on the composites, up to a strain of 30%, no delamination is observed on the sprayed patterns. *In situ* microscale tests are performed to show the evolution of the fiber angle

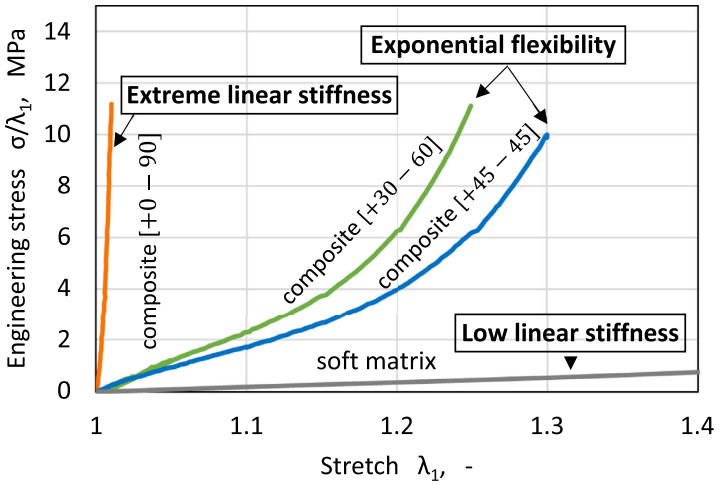

Fig. 3. Experimental stress-stretch results showing that the combination of a soft matrix with stiff fibers provides exceptional, tunable flexibilities in soft composites.

during loading experiments as well as the fiber distortions at their intersections, both contributing to the mechanical interaction. To this end, the transparent PDMS-GF samples with fiber orientation [+45– 45] are placed in a custom-designed *in situ* tensile test device, while they are under an optical microscope (Alicona InfiniteFocusG5 Plus, Austria) with an objective magnification of 100x.

2.2. Tunable flexibility and 3D full-field stretch analysis

The average stress-stretch results of the PDMS-GF composites with the preferred fiber orientations as [+45 − 45] and [+30 − 60] are presented in Fig. 3. Included in this figure are the average stress-stretch responses of the matrix and the composite [+0 − 90]. The stretch λ_1 is calculated based on changes in the length of the samples in the loading direction $\mathbf{e}_1$. Accordingly, $\lambda_1 = l/l_0$, where l is the length of the sample in the deformed configuration, while l_0 denotes its undeformed length. 3D full-field, high-resolution images are captured via the DIC method. It is carried out for the samples with fiber orientations such as [+45 − 45] and [+30 − 60] during tensile tests on PDMS-GF composites. The corresponding local stretch maps are depicted respectively in Fig. 4(a) and (b) for specific stretches, showing inhomogeneous deformation fields in the composites.

Fig. 3 indicates that the combination of a soft matrix with stiff fibers, having *linear* elastic behaviors within the operating limits of the composite, enables us to build up composites with tunable *exponential* flexibilities. This unique flexibility, which changes exponentially in some directions and shows extreme linear stiffness in other directions, is valuable in many potential applications, such as soft wearable robots, morphing aircraft, isolation mounts, and marine structures [1,2,5,28]. It should be mentioned that, in addition to orienting the fibers, one can tailor the properties of the constituent materials to achieve a much wider range of flexibility ratios.

2.3. Physical meaning of mechanical interaction

The fiber-reinforced materials are commonly modeled and characterized in terms of their constituent materials, while their matrix-fiber mechanical interaction has not yet been evaluated satisfactorily in the literature. It is noted that the term 'matrix-fiber mechanical interaction' is concisely referred to herein as both the fiber-fiber and the matrix-fiber mechanical interactions. The latter is a result of the angle change between deformed fibers, which trigger the shear interaction of the matrix/fiber interface, while the former manifests itself in the form of the distortion of the fibers at their intersections. The evolution of the fiber angle in a specific region of the sample [+45 − 45], wherein the fibers are free-ended and therefore they can rotate easily, are indicated in Fig. 5(a) using the micrographs captured during the *in situ* tensile tests. Moreover, the fiber distortions at their intersections are illustrated in Fig. 5(b) for three different regions. The micrographs are indicative of the angle change between deformed fibers and the significant amount of the fiber distortions at their intersections, which both contribute to the matrix-fiber mechanical interaction.

3. Modeling and material parameters

3.1. Constitutive model

A unified invariant-base constitutive model, named Matrix-Fiber-Interaction (MFI) model, is employed to take into account particularly the matrix-fiber mechanical interaction in fiber-reinforced elastomers with two fiber families. The model is decomposed into three contributions: matrix, fiber, and matrix-fiber mechanical interaction [29]. The general form of the MFI strain-energy density function is defined as

$$\Psi(\mathbf{C},\ \{\mathbf{M},\mathbf{N}\}) = \Psi_{\mathrm{M}}(I_1) + \Psi_{\mathrm{F}}(I_4,\ I_6) + \Psi_{\tau}(I_8^*), \tag{1}$$

where the subscripts M, F, and τ denote the contributions of the matrix, the fiber, and the matrix-fiber mechanical interaction, respectively. In the equation above, $I_1 = \mathrm{tr}\,\mathbf{C}$, where $\mathbf{C} = \mathbf{F}^{\mathrm{T}}\mathbf{F}$ is the right Cauchy-Green strain tensor, and $\mathbf{F}$ is the deformation gradient. The extensional-based invariants with definitions $I_4(\mathbf{M}) = \mathbf{C}\colon \mathbf{M}\otimes\mathbf{M}$ and $I_6(\mathbf{N}) = \mathbf{C}\colon \mathbf{N}\otimes\mathbf{N}$ are employed by the fiber potential Ψ_{F}.

In [30] a relation for the current angle between deformed fibers is presented as the left-hand side of the following equation

$$\cos\varphi = \frac{\mathbf{C}:\mathbf{M}\otimes\mathbf{N}}{\sqrt{\mathbf{C}:\mathbf{M}\otimes\mathbf{M}}\,\sqrt{\mathbf{C}:\mathbf{N}\otimes\mathbf{N}}} = \frac{I_8}{\sqrt{I_4\ I_6}} = I_8^* \tag{2}$$

An angular-base invariant is considered in [29] such as the right-hand equation by replacing the invariants I_4, I_6 (defined above), and $I_8(\mathbf{M},\mathbf{N}) = \mathbf{C}\colon \mathbf{M}\otimes\mathbf{N}$ in Eq. (2). Because the matrix-fiber mechanical interaction is a result of the fiber rotation, the angular-base invariant I_8^* is employed by the mechanical interaction potential Ψ_{τ}. The functional forms of the potentials in Eq. (1) are given by the neoHookean potential [31] for the matrix and a quadratic function for the fibers as

$$\Psi_{\mathrm{M}} = \mu(I_1 - 3) - p(J-1),\ \Psi_{\mathrm{F}} = \frac{k_1}{2}\sum_{i=4,6}(I_i - 1)^2 \tag{3}$$

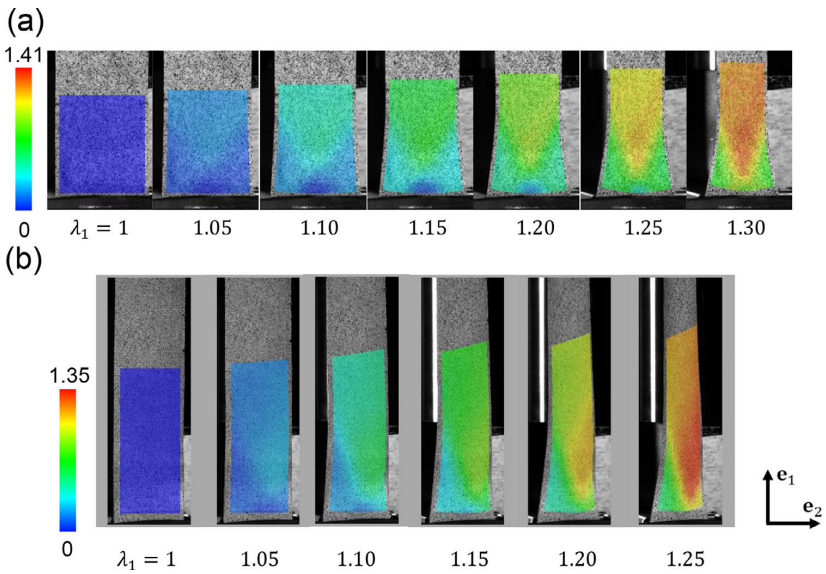

Fig. 4. 3D full-field stretch maps captured by DIC for composites subjected to the tensile tests in e_1 direction: (a) composite with fiber orientation [+45– 45]; (b) composite with fiber orientation [+30– 60].

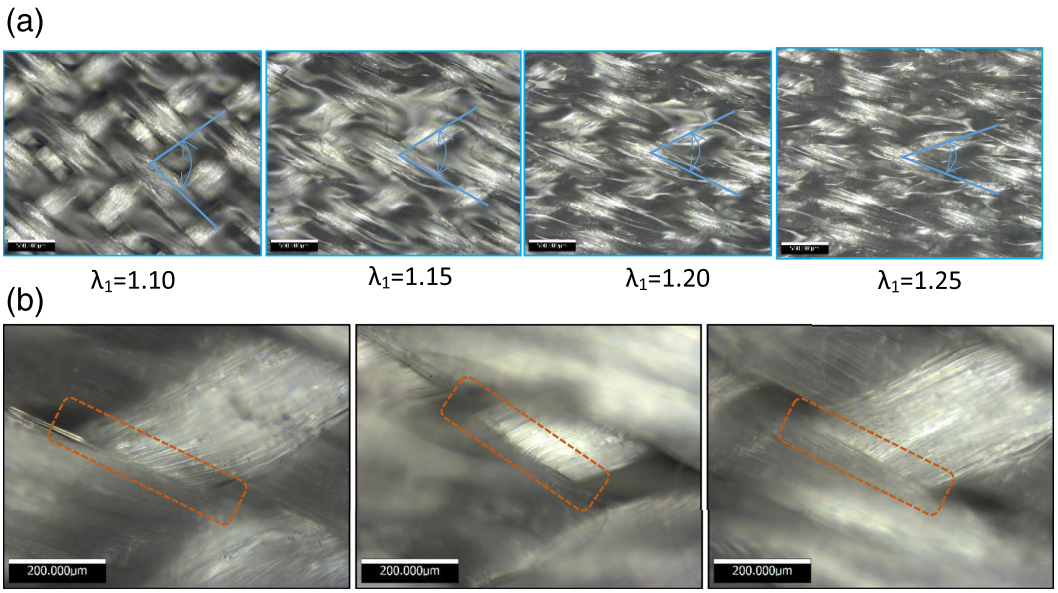

Fig. 5. (a) Representative micrographs showing the evolution of the fiber angle during the deformation of the composite [+45 – 45]. (b) Distortions of the fibers at their intersections.

and

$$\Psi_\tau = \frac{c_1}{2c_2}\left[\exp\left(c_2\left(I_8^* - \cos(2\theta)\right)^2\right) - 1\right] + c_3\left(I_8^* - \cos(2\theta)\right)^2. \quad (4)$$

The constants c_{10}, k_1, c_1, and c_3 are positive material parameters with the dimension of stress, while c_2 is a positive, dimensionless parameter. The scalar p serves as an indeterminate Lagrange multiplier that can be identified as hydrostatic pressure. The constant $\cos(2\theta)$ is the cosine of the current angle between fibers in the undeformed configuration.

3.2. Finite element modeling

The unified invariant-based MFI constitutive model is implemented in the FEM commercial program Abaqus using a user-defined interface, UMAT. The material is treated as nearly incompressible; therefore, for the finite element simulations, the model is decomposed into volumetric and isochoric parts. Accordingly, the Cauchy stress and elasticity tensors should be decoupled into volumetric and isochoric parts in an Eulerian description. The dimensions of the finite element models are 100 mm (length) × 20 mm (width) × 0.5 mm (thickness) for each ply. All the geometries are discretized with 3D reduced integration, eight-node lin-

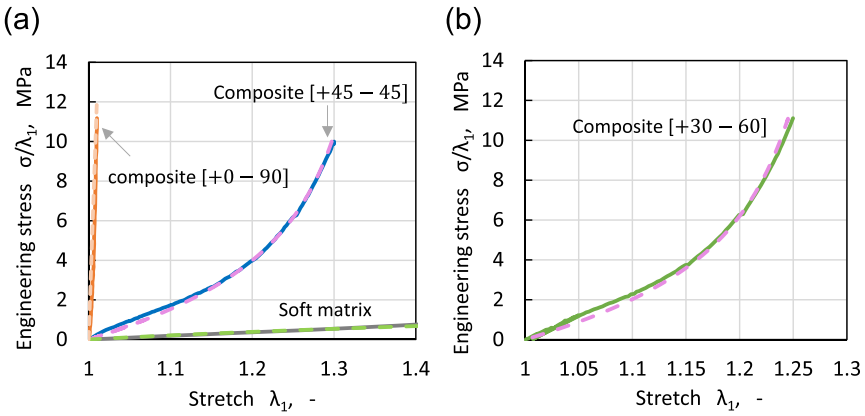

Fig. 6. (a) Comparisons of the results obtained from the inverse finite element modeling (dash lines) and the tensile tests (solid lines) on composites with preferred fiber orientation [+45– 45] in $\boldsymbol{e}_1$ direction and [+0 – 90] in the fiber direction as well as the pure soft matrix. (b) Verification of the model performance via the comparison of the finite element results with experiments for composite with fiber orientation [+30– 60] subjected to the uniaxial extensions in $\boldsymbol{e}_1$ direction.

ear solid elements with hybrid formulation (C3D8RH). Each layer of the composite laminates is discretized with a mesh size of 1 mm, and depending on the number of the plies the total number of elements varies. To see the effect of mesh refinement, three convergence tests are conducted adopting finer mesh sizes such as 1 mm, 0.9 mm, and 0.8 mm. It is figured out that additional mesh refinement does not affect the stress-stretch, moment, and twist angle results. To enforce the incompressibility condition, we adopt a large value of the bulk modulus as $\kappa = 10^5$ MPa. The model geometry and the boundary conditions used for the simulations are the same as those used initially in the experiments.

3.3. Material parameters

The material parameters are calibrated through inverse finite element modeling implemented in the optimization code LS-OPT employing the least-squares algorithm to minimize the discrepancy between the model results and entered experimental data via the function

$$\Delta = \sum_{j=1}^{n} \left\| \phi_j^{\text{model}} - \phi_j^{\text{data}} \right\|^2 \tag{5}$$

where φ_j are the components of a force-displacement vector corresponding to the data points numbered by n.

The material parameter of the matrix (μ) is obtained using the uniaxial tensile tests on the pure soft matrix (gray curve in Fig. 3). Then, keeping the matrix parameter, the material parameter of the fibers (k_1) is determined using the results of the tensile tests on the composite with the preferred fiber orientation [+0 – 90] stretched in the fiber direction (orange curve in Fig. 3). Upon finding the material parameters of the matrix and fibers independently using the optimization code, the material properties of the interaction potential (i.e. c_1, c_2, c_3) are determined using the stress-stretch responses of the composite with the fiber orientation [+45 – 45] (blue curve in Fig. 3). It is carried out by the inverse finite element modeling and the results of all verifications are presented in Fig. 6(a). In this figure, the solid lines represent the experimental data while the dash lines indicate the finite element results obtained by the optimization code. The material parameters of the matrix, the fibers, and the matrix-fiber mechanical interaction are listed in Table 1. The behavior of the model for predicting the stress-stretch experimental responses of the non-symmetric deformations associated with the composite [+30 – 60] is illustrated in Fig. 6(b). The boundary conditions for all simulations are those used initially by the experiments. Both plots indicate good qualitative agreements between the models and the test data. The model appears to be able to reproduce the rich complexities of the material, such as the nonlinearity and the anisotropy.

Table 1
Material properties of the PDMS-GF composite.

Contribution	μ, MPa	k_1, MPa	c_1, MPa	c_2,–	c_3, MPa
Matrix	0.40				
Fiber		227.0			
Interaction			0.02496	2.0364	0.8948

4. Linear stiffness versus exponential flexibility

As mentioned in the previous section, a combination of soft and stiff materials with linear elastic properties results in composites showing a wide range of flexibility ratios, from extremely linear to exponential flexibilities. One explanation for the extremely linear properties of the composite is obviously related to the stiff fibers. However, to the best of the authors' knowledge, little information exists on why a combination of stiff fibers and a soft matrix with linear properties results in exponential flexibilities in fiber-reinforced composites. In order to explain these differences, the features involved in the highly nonlinear mechanics of such composites are evaluated. To this end, the contributions of the matrix, the fibers, and the newly introduced matrix-fiber mechanical interaction are evaluated during the uniaxial deformation of specific composites. The composites with the preferred fiber orientations as [+45 – 45] and [+30 – 60], with mechanical behaviors given already in Fig. 3 and the material properties tabulated in Table 1, are chosen here. The strain energy stored in the matrix (Ψ_M), in the fibers (Ψ_F), and in the matrix-fiber mechanical interaction (Ψ_τ), as well as the total strain-energy density stored in the respective composites (Ψ), are evaluated. The finite element results are provided in Fig. 7(a) and (b) for composites with fiber orientations [+45 – 45] and [+30 – 60], respectively. In addition, the spatial distributions of the respective stored energies are depicted in the same figure for a stretch of $\lambda_1 = 1.25$. Although the constituent materials have linear mechanical behaviors (see Fig. 3), it is seen in both plots in Fig. 7 that the matrix and especially the fibers show nonlinear contributions in composites undergoing the specific deformations explained above. Nevertheless, as it is illustrated in these two figures, the mechanical interaction potential Ψ_τ contributes exponentially to the deformation, even more than the constituent materials. It can now be stated that the highly nonlinear mechanics of the composites is mainly due to the contribution of the matrix-fiber mechanical interaction, namely, the feature involved in the unique exponential flexibility of the composites.

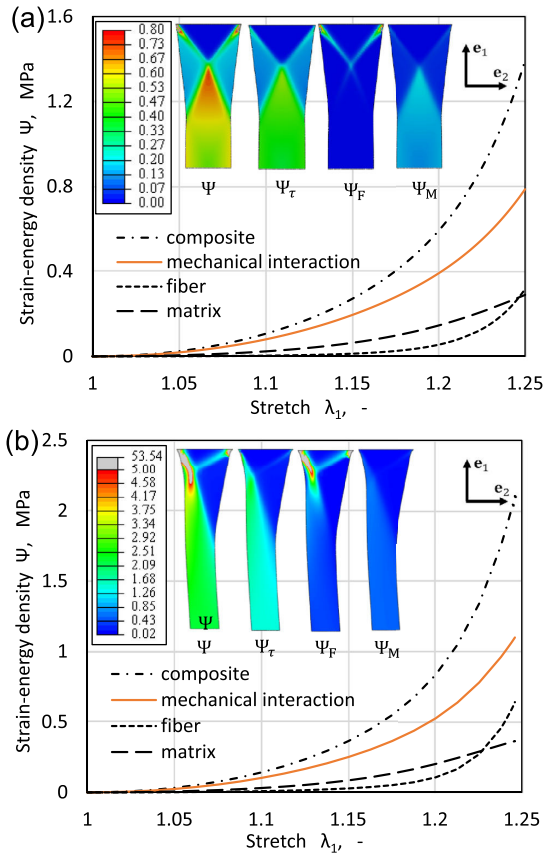

Fig. 7. Contributions of the constituent materials and matrix-fiber mechanical interaction to the exponential flexibility of the composites: (a) with preferred fiber orientation as [+45 −45]; (b) with fiber orientation as [+30 −60], subjected to uniaxial extensions in the $\boldsymbol{e}_1$ direction.

Note that, as it is apparent from Fig. 6(a), the neoHookean and the fiber potentials presented in Eq. (3) stand close to the respective experimental results. Accordingly, it is expected that the contributions of the matrix, fibers, and mechanical interactions in the deformation of the composites presented in Fig. 7 have not been perturbed by each other.

5. Load-coupling potentials

The tunable flexibility of single-lamella composites discussed in previous sections now can be exploited to exhibit beneficial load-coupling behaviors in fiber-reinforced laminates. Extension-twist coupling is one such characteristic. In this section, a set of conflicting requirements are addressed, based on which a design space is introduced to evaluate the effective load-coupling behaviors. The effect of structural variables on these parameters is then evaluated by performing a set of parametric studies. The possible extension-twist coupling potentials are then discussed within the introduced design space.

5.1. Conflicting requirements

Based on the Classical Lamination Theory (CLT), the fundamental mechanism producing extension-twist coupling in laminated composites is a result of the in-plane extension-shear coupling associated with the off-axis plies [20]. In CLT, the relation between deformation modes (i.e., stresses and moments) with deformations (i.e., ε_1, ε_2) are defined with $[A]$, $[B]$ and $[D]$ matrices, which represent the in-plane, the coupling, and the flexural stiffness matrix of the laminate, respectively, that reads

$$\begin{bmatrix} \sigma_e \\ M \end{bmatrix} = \begin{bmatrix} A & B \\ B & D \end{bmatrix} \begin{bmatrix} \varepsilon_1 \\ \varepsilon_2 \end{bmatrix} \tag{6}$$

Fig. 8(a) schematically shows the coupling of deformation modes such as end moment (M) and longitudinal (engineering) stress (σ_e) as well as end twist (Ω) in a composite laminate. These parameters, which may be addressed herein as conflicting requirements for designing laminates exhibiting effective extension-twist coupling behaviors, are individually evaluated. Effective load-coupling behaviors necessitate the laminate to possess unique properties, the most important of which are: high output values of the end moment, high end-twist capability, and low longitudinal stress, so as to minimize the actuation force required for stretching the laminates. An application scenario that necessitates possessing these unique properties is morphing systems, wherein conflicting requirements such as low in-plane stiffness while maintaining large strain capability and exceptional flexibility to achieve complex morphed shapes are highly desired. During a load-coupling process, the values of the parameters $\{M, \Omega\}$ are increasing; therefore, based on the definition above, they are not assumed to be conflicting requirements. On the other hand, an effective coupling behavior requires high torsional capability for low longitudinal stresses, which implies that the parameter set $\{\sigma_e,\Omega\}$ is a conflicting requirement. Admittedly, the same can be stated for the set $\{M, \sigma_e\}$ in that these two parameters are highly coupled to each other, while it is not suitable for load-coupling applications. Accordingly, a new term M/σ_e is introduced here, which is called the decoupling ratio. A higher degree of decoupling between end moment and longitudinal stress corresponds to the laminates showing more potential for load-coupling applications. The only parameter that remains is the torsional flexibility Ω, which is a desirable quantity for load coupling. Consequently, a design space represented by a diagram is considered in which its vertical axis denotes the decoupling ratio M/σ_e, while its horizontal axis shows the degree of torsional flexibility through Ω. In this work, effective load-coupling behaviors are studied within this design space.

5.2. Parametric investigations

Parametric studies are performed using the finite element analysis on 2-, 3-, and 4-ply laminates with different ply thicknesses, stacking directions, and constituent material properties to enhance the understanding of the relationship between end moment and longitudinal stress, as well as the relationship between the decoupling ratio M/σ_e and end twist Ω during extension-twist deformations. The composite laminates are obtained by stacking a set of identical orthotropic plies where the ply fiber orientations are assumed to be [+15 − 5], [+30 − 60], [+45 − 45], [+60 − 30], and [+75 − 15] with respect to the loading direction $\mathbf{e}_1$, shown in Fig. 8(b). As shown, the plies differ in terms of the preferred fiber orientations. The plies are numbered from 1 to 5; consequently, the stacking sequence of the composite lay-up shown in this figure reads [12,345]. As the fiber-dominated direction cannot accommodate any significant strain, the ply with the fiber orientation [+0 − 90] is not taken into account here. Lamella dimensions in the reference configuration are 100 mm, 20 mm, and 0.5 mm for the length, width, and thickness, respectively, with an aspect ratio of 5. It should be noted that the aspect ratio should be chosen so that the two fiber families of each ply are not located in the two clamping areas at the ends of the strips. If they are, the free-ended fibers will not be able to rotate easily, and this will cause a fiber-stretching-dominated deformation to occur with no significant contribution toward the coupling of the deformation modes.

Two series of simulations are performed on the laminates described above. In the first series, boundary conditions are set such that one end

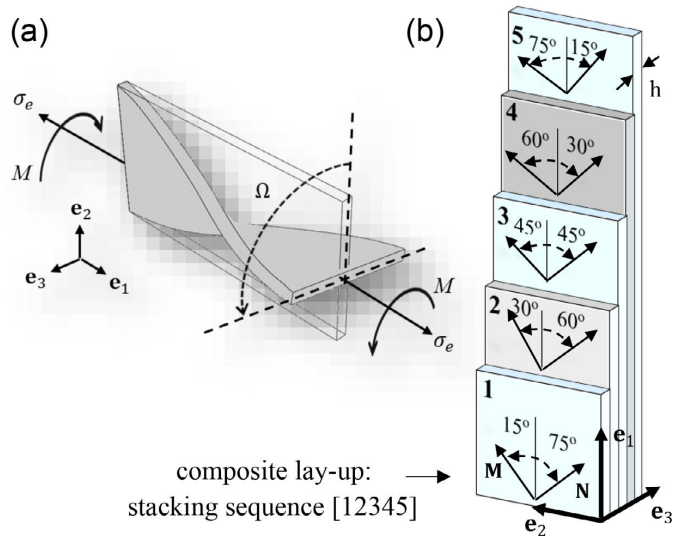

Fig. 8. (a) Extension-twist coupling of a composite laminate. (b) Composite lay-up with plies numbered from 1 to 5. An exemplary stacking sequence of plies [12,345] is shown.

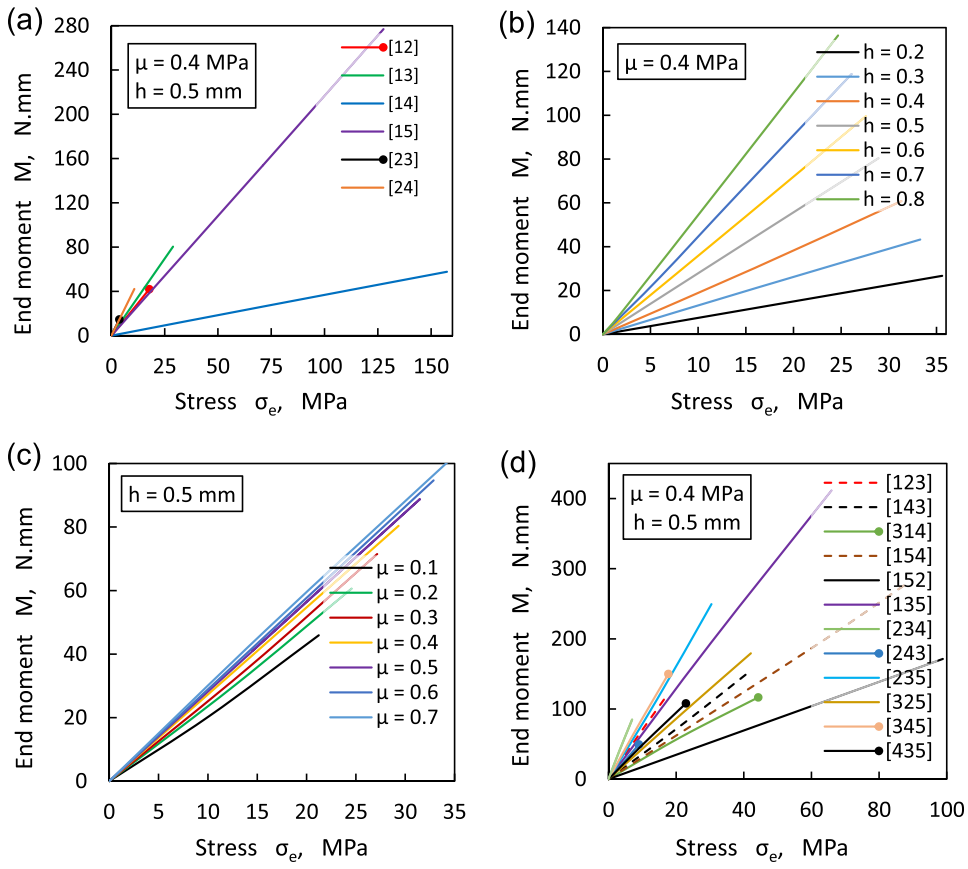

Fig. 9. Parametric investigations of the structural variables with respect to the results of displacement-control simulations for a specific displacement of 8 mm.

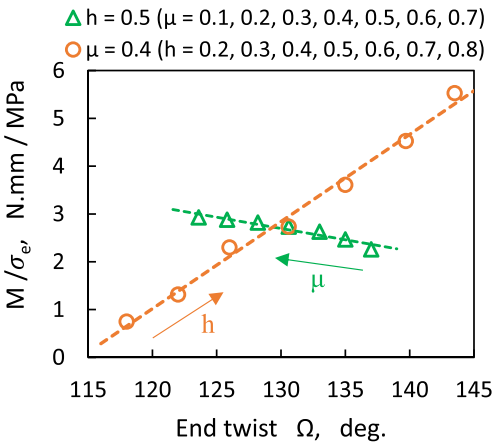

Fig. 10. An almost linear relationship between the decoupling ratio M/σ_e and the torsional flexibility represented by Ω with respect to the changes in the thickness of the plies and shear modulus of the matrix.

of the laminate is fixed, while the opposite end is allowed to freely elongate and rotate along and about the $\mathbf{e}_1$ direction, respectively. The values of the longitudinal engineering stress ($\sigma_e = \sigma/\lambda_1$) and end-twist (Ω) are obtained from this particular boundary condition. In the second series of simulations, the same boundary condition is applied, with the exception that the nodes on the face of the moving end are not allowed to rotate about the $\mathbf{e}_1$ direction. Therefore, the values of the end moment (M) are measured during the extension-twist coupling. All laminates are subjected to a uniaxial displacement of $d = 8$mm in the loading direction, applied at the end face of the laminates.

In Fig. 9(a), with fixed values for both the ply thickness and the shear modulus of the matrix, the end moment M is plotted versus engineering longitudinal stress σ_e for a 2-ply laminate with different stacking sequences. The effects of varying the ply thickness are shown in Fig. 9(b) for a specific value of the shear modulus for the same laminate. Moreover, considering now fixed values for ply thickness, the influence of shear modulus changes is depicted in Fig. 9(c). Surprisingly, these three figures imply that the two parameters M and σ_e have linear relationships with respect to the changes in stacking sequence, ply thickness, and shear modulus of the matrix. The same findings are obtained for 3- and 4-ply laminates. In Fig. 9(d), the results associated with a 3-ply laminate are provided; they show there exists a linear relationship between end moment and stress for given stacking sequences. Knowing now the linear relationship between M and σ_e, another set of parametric studies is performed to understand the relationship between the decoupling ratio M/σ_e and end twist Ω with respect to the thickness and shear modulus changes. The results shown in Fig. 10 follow almost linear increases in the decoupling ratio with an end twist for a 2-ply laminate. The same trends are observed for 3- and 4-ply laminates with respect to all possible stacking sequences (not shown).

5.3. Extension-twist coupling potentials

Bearing in mind the discussion in the previous section concerning the existence of a linear relationship between M and σ_e as well as M/σ_e and Ω, the capability of a laminate for load-coupling applications can be now represented by only one point in the design space introduced in Section 5.1. That is, a point on the referred diagram shows the potential of a specific laminate for simultaneous consideration of both extension-twist coupling and flexibility, both of which are highly desirable.

The values of M/σ_e versus Ω are plotted in Fig. 11(a), (b), and (c), for 2-, 3-, and 4-ply laminates, respectively, subjected to the deformations described in the previous section. All possible stacking sequences are evaluated. The diagrams are plotted based on the maximum values of Ω for all laminates (note that the decoupling ratio M/σ_e is constant during the deformation, see the previous section). A reference line as a determinative indicator is shown in all diagrams; it can be used to evaluate the load-coupling capability of a particular laminate. The reference line is adopted based on 4-ply laminates. A point close to and inclined to the end of this line shows a large amount of load-coupling potential with

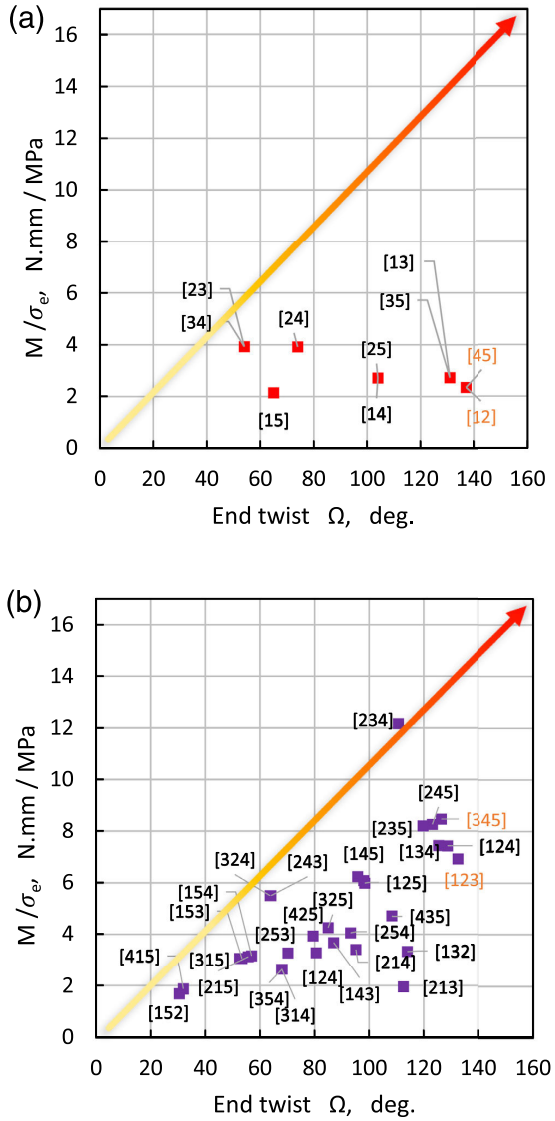

Fig. 11. Load-coupling potentials represented in a design space featuring a reference line that can be used to evaluate the capability of the fiber-reinforced composite laminates for the extension-twist coupling behaviors shown for (a) 2-ply, (b) 3-ply, and (c) 4-ply laminates with all possible stacking sequences. Its vertical axis denotes the decoupling ratio while the values of the torsional flexibility are aligned in the horizontal axis.

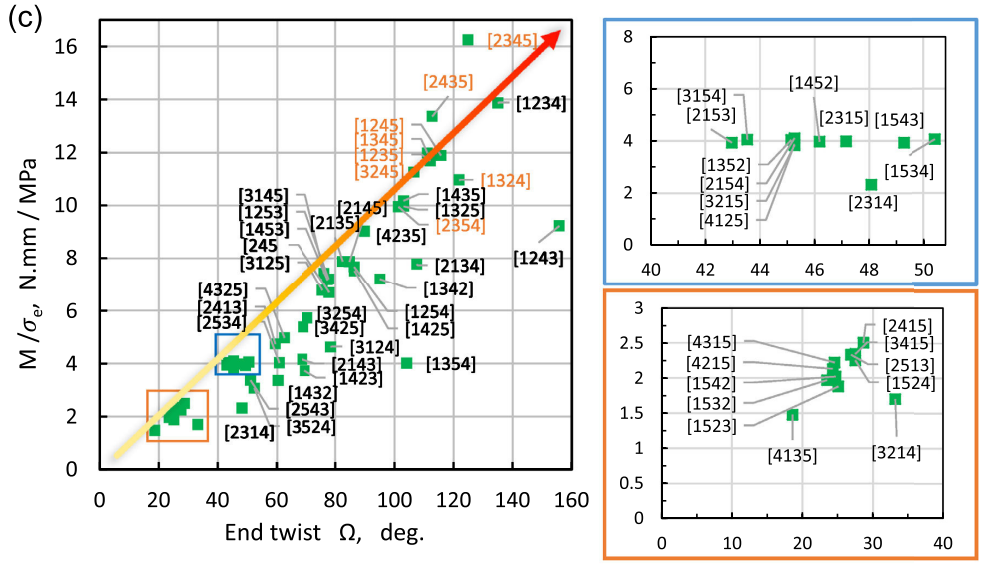

Fig. 11. Continued

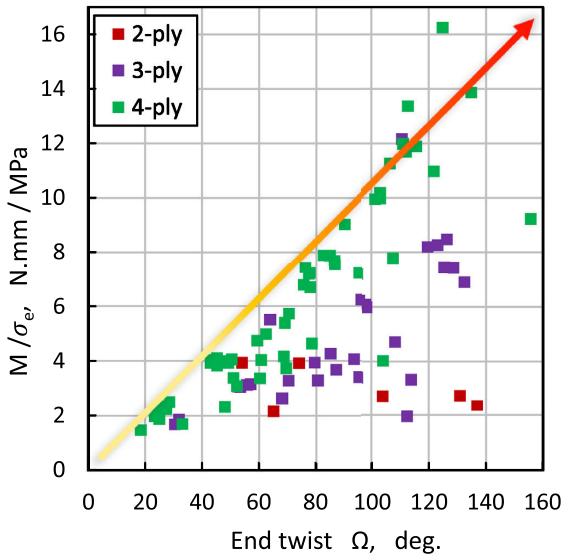

Fig 12. Comparison of the load-coupling potentials of 2-, 3-, and 4-ply laminates, considering all possible stacking sequences of the plies.

simultaneous consideration of both extension-twist coupling and flexibility. It is generally observed that providing a higher degree of decoupling between end moment and longitudinal stress gives rise to a much higher amount of flexibility. The points indicated by colored labels are associated with laminates showing a considerable amount of redirection of the forces, mainly due to the coupling between deformation modes. For instance, for a 3-ply laminate with the stacking sequence [345], see Fig. 11(b), it follows that $\sigma_{\text{laminate}} < \sigma_3 + \sigma_4 + \sigma_5$, which means the resultant stress in the laminate is less than the sum of the stresses in each of the respective plies obtained separately.

For further comparisons, all the results are provided in a single diagram in Fig 12. Generally, an increase in the number of plies results in more load-coupling potentials. This diagram uncovers unique load-coupling potentials found in flexible composite laminates. These benefits can be gainfully exploited by designing composite laminates capable of supporting distinct functionalities in a controlled manner in new applications. Applications such as morphing aircraft wings, artificial muscles, wearable systems, soft robotics, and marine structures, wherein the coupling between deformation modes and flexibility are highly desirable.

Conclusion

In this work, we have identified a unique performance benefit by evaluating the extension-twist coupling potentials in flexible reinforced composites. It is shown that a combination of soft elastomers with stiff fibers enables the build-up of composites with distinct direction-dependent properties, providing a wide range of tunable flexibility ratios, from extremely linear to highly exponential flexibilities. In order to explain these exponential flexibilities, the contributions of features that could possibly be involved in the highly nonlinear mechanics of such composites are evaluated. It is observed that, although the constituent materials have linear elastic mechanical behaviors (within the operating limits of the composite), they show nonlinear contributions in composites undergoing specific deformations. Nevertheless, it is demonstrated that the mechanical interaction potential contributes exponentially to the deformations even more than constituent materials. It is concluded that the highly exponential flexibility of the composites is mainly due to the contribution of the matrix-fiber mechanical interactions.

In order to exploit the tunable flexibility of fiber-reinforced composites for effective load-coupling behaviors such as extension-twist coupling, a set of conflicting requirements are evaluated. As a result, a design space is introduced through which the capability of a laminate can be evaluated for load-coupling applications. The design space is represented by a diagram in which the vertical axis denotes the decoupling ratio M/σ_e and the horizontal axis shows the degree of torsional flexi-

bility through Ω. In this space, the load-coupling potential of each laminate can be displayed by only one point on the referred diagram. For this reason, a series of parametric studies are performed whereby linear relations are obtained between end moment and longitudinal stress, as well as between the decoupling ratio and torsional flexibility. It is shown that these relations are independent of structural variables such as ply thickness, constituent material properties, stacking direction, and number of plies. The referred diagram shows that, in general, providing a higher degree of decoupling between end moment and longitudinal stress gives rise to a much higher amount of flexibility, which is highly desirable for load-coupling applications.

Declaration of Competing Interest

The authors declare that they have no known competing financial interests or personal relationships that could have appeared to influence the work reported in this paper.

Acknowledgment

The research work was performed at the Polymer Competence Center Leoben GmbH (PCCL, Austria) within the framework of the COMET-program of the Federal Ministry of Science, Research and Economy with contributions by Montanuniversitaet Leoben (Chair of Materials Science and Testing of Polymers, Austria). This research was funded by the Federal Ministry for Climate Action, Environment, Energy, Mobility, Innovation, and Technology and the Federal Ministry for Digital and Economic Affairs, Grant No. 854178.

References

[1] Y. Shan, M. Philen, A. Lotfi, S. Li, C.E. Bakis, C.D. Rahn, et al., Variable stiffness structures utilizing fluidic flexible matrix composites, J. Intell. Mater. Syst. Struct. 20 (4) (2009) 443–456.
[2] Y. Shan, M.P. Philen, C.E. Bakis, K.-.W. Wang, C.D. Rahn, Nonlinear-elastic finite axisymmetric deformation of flexible matrix composite membranes under internal pressure and axial force, Compos. Sci. Technol. 66 (15) (2006) 3053–3063.
[3] Variable stiffness adaptive structures utilizing hydraulically pressurized flexible matrix composites with valve control; 2006.
[4] A variable transverse stiffness sandwich structure using fluidic flexible matrix composites (F2MC): international society for optics and photonics; 2008.
[5] F. Connolly, D.A. Wagner, C.J. Walsh, K. Bertoldi, Sew-free anisotropic textile composites for rapid design and manufacturing of soft wearable robots, Extreme Mech. Lett. 27 (2019) 52–58.
[6] Al-Fahaam H.S.H. Wearable exoskeleton systems based-on pneumatic soft actuators and controlled by parallel processing; 2019.
[7] S. Barbarino, O. Bilgen, R.M. Ajaj, M.I. Friswell, D.J. Inman, A review of morphing aircraft, J. Intell. Mater. Syst. Struct. 22 (9) (2011) 823–877.
[8] S. Murugan, E.I.S. Flores, S. Adhikari, M.I. Friswell, Optimal design of variable fiber spacing composites for morphing aircraft skins, Compos. Struct. 94 (5) (2012) 1626–1633.
[9] J. Sun, Q. Guan, Y. Liu, J. Leng, Morphing aircraft based on smart materials and structures: a state-of-the-art review, J. Intell. Mater. Syst. Struct. 27 (17) (2016) 2289–2312.
[10] G. Murray, F. Gandhi, C. Bakis, Flexible matrix composite skins for one-dimensional wing morphing, J. Intell. Mater. Syst. Struct. 21 (17) (2010) 1771–1781.
[11] T. Lu, Z. Shi, Q. Shi, T.J. Wang, Bioinspired bicipital muscle with fiber-constrained dielectric elastomer actuator, Extreme Mech. Lett. 6 (2016) 75–81.
[12] M.K. Philen, Y. Shan, P. Prakash, K.W. Wang, C.D. Rahn, A.L. Zydney, et al., Fibrillar network adaptive structure with ion-transport actuation, J. Intell. Mater. Syst. Struct. 18 (4) (2007) 323–334.
[13] Bishop-Moser J.L. Design of generalized fiber-reinforced elasto-fluidic Systems 2014.
[14] W. Felt, C.D. Remy, A closed-form kinematic model for fiber-reinforced elastomeric enclosures, J. Mech. Robot. 10 (1) (2018) 14501.
[15] W. Felt, M.J. Telleria, T.F. Allen, G. Hein, J.B. Pompa, K. Albert, et al., An inductance-based sensing system for bellows-driven continuum joints in soft robots, Auton. Robots (2017) 1–14.
[16] Thermomechanical behavior and experimental testing of flexible matrix composite box-beams with extension-twist coupling; 2005.
[17] Design evaluation of model and full-scale flexible matrix composites tiltrotor blades with extension-twist coupling: American helicopter society; 2006.
[18] Extension-twist coupled tiltrotor blades using flexible matrix composites: American institute of aeronautics and astronautics Inc.(AIAA); 2005.
[19] Non-linear modeling of extension-twist coupled energy absorbing composite tubes; 2012.
[20] E.A. Armanios, A. Makeev, D. Hooke, Finite-displacement analysis of laminated composite strips with extension-twist coupling, J. Aerosp. Eng. 9 (3) (1996) 80–91.
[21] A. Sensini, L. Cristofolini, Biofabrication of electrospun scaffolds for the regeneration of tendons and ligaments, Materials (Basel) 11 (10) (2018) 1963.
[22] D. Benayahu, M. Sharabi, L. Pomeraniec, L. Awad, R. Haj-Ali, Y. Benayahu, Unique collagen fibers for biomedical applications, Mar. Drugs 16 (4) (2018) 102.
[23] Field trials and testing of the OctArm continuum manipulator: IEEE; 2006.
[24] X. Cao, M. Zhang, Z. Zhang, Y. Xu, Y. Xiao, T Li, Review of soft linear actuator and the design of a dielectric elastomer linear actuator, Acta Mech. Solida Sin. 32 (5) (2019) 566–579.
[25] D.L. Rodriguez, M.J. Aftosmis, M. Nemec, G.R. Anderson, Optimization of flexible wings with distributed flaps at off-design conditions, J. Aircr. 53 (6) (2016) 1731–1745.
[26] M.R. Mansouri, H. Darijani, Constitutive modeling of isotropic hyperelastic materials in an exponential framework using a self-contained approach, Int. J. Solids Struct. 51 (25–26) (2014) 4316–4326.
[27] M.R. Mansouri, H. Darijani, M. Baghani, On the correlation of FEM and experiments for hyperelastic elastomers, Exp. Mech. 57 (2) (2017) 195–206.
[28] I.K. Kuder, A.F. Arrieta, W.E. Raither, P. Ermanni, Variable stiffness material and structural concepts for morphing applications, Prog. Aerosp. Sci. 63 (2013) 33–55.
[29] M.R. Mansouri, P.F. Fuchs, J. Criscione, B. Schrittesser, J. Beter, The contribution of mechanical interactions to the constitutive modeling of fiber-reinforced elastomers, Eur. J. Mech. - A/Solids 85 (2020) 104081, doi:10.1016/j.euromechsol.2020.104081.
[30] J.C. Criscione, W.C. Hunter, Kinematics and elasticity framework for materials with two fiber families, Continuum Mech. Thermodyn. 15 (6) (2003) 613–628.
[31] L.R. Treloar, The elasticity of a network of long-chain molecules. I, Trans. Faraday Soc. 39 (1943) 36–41.